Spring 1-1-2017

Theoretical and Experimental Investigation of Matrix Inclusions on the Fracture Toughness of Composite Material

Shahlaa Al Wakeel
University of Colorado at Boulder, shahlaa.alwakeel3@gmail.com

Theoretical and experimental investigation of matrix inclusions on the fracture toughness of composite material

by

SHAHLAA A. Al WAKEEL

M.S., University of Technology, Iraq, 1996

B.S., University of Technology, Iraq,1986

A thesis submitted to the

Faculty of the Graduate School of the

University of Colorado in partial fulfillment

of the requirement for the degree of

Doctorate of Philosophy

Department of Civil, Environmental and Architectural Engineering

2017

This dissertation entitled:

Theoretical and experimental investigation of matrix inclusions on the fracture toughness of composite material

written by Shahlaa A. Al Wakeel

has been approved for the Department of Civil, Environmental and Architectural Engineering

_____

Professor Mija H. Hubler (Chair)

_____

Professor Yunping Xi

_____

Professor Victor E. Saouma

_____

Professor Wil V. Srubar III

_____

Dr. Edward Garboczi

Date _____

The final copy of this thesis has been examined by the signatories, and we find that both the content and the form meet acceptable presentation standards of scholarly work in the above mentioned discipline.

Shahlaa Al Wakeel (Ph.D. Civil Engineering)

Theoretical and experimental investigation of matrix inclusions on the fracture toughness of composite material

Dissertation directed by Professor Mija H. Hubler

ABSTRACT

This dissertation studies the impact of microstructure on macro-scale fracture parameters. Experimental and theoretical investigations of fracture toughness are carried out on a representative particulate composite material and reconciled by explicitly considering inclusions within the matrix. The reliability of any structure is a function of its resistance to fracture. Cracks resulting from stress concentrations are the major sources of fracture whether the material is classified as ductile, brittle, or quasi-brittle. The spatial distribution of inclusions in particulate composite materials, such as concrete and other heterogeneous materials, plays an important role in determining material fracture behavior due to the localized stress generated by the inclusion arrangement when cracks open. By controlling the spatial statistics of the inclusion microstructure in the matrix of a composite material, it is possible to control the amount or direction of crack development and may be possible to improve the material's reliability. As steps towards this goal this dissertation investigates the discrepancy between the micro-scratch and macro-scale three-point bending test methods due to the presence of matrix inclusions, applies the theoretical equations for fracture toughness which consider inclusions in the case of micro-particles in cement, and investigates how spatial statistic descriptions may be used to capture the impact of inclusions in a simple closed-form approach. The results of this work allow us to move towards a forward design method to design particulate composite micro-structures for improved resilience to local damage without fracturing.

DEDICATION

This dissertation is dedicated to:

The soul of my parents ***Essmat*** and ***Abdulkareem***, I will always remember you.

The three cornerstones of my life, to my dear children ***Jwan***, ***Shwan*** and ***Jehan***; your encouragement in every step of my Ph.D. degree, has always inspired me to put all best effort in to my research.

ACKNOWLEDGMENTS

My final semester of my doctorate has been funded by a Dissertation Completion Grant from the CU Boulder Civil, Environmental, and Architectural Engineering (CEAE) Department. This support is greatly appreciated.

I sincerely would like to acknowledge my advisor, Professor Mija Hubler for her guidance and especially her support through my research work. Also, I would like to thank all the people who helped and supported me during my Ph.D studies adventure . I will start with my committee members, Professors Yunping Xi, Wil V. Srubar III, Victor E. Saouma and Dr. Edward Garboczi for their comments on my dissertation work.

From deep of my heart I would like to thank the faculty members who taught me; in the structural engineering major / civil engineering department. I also thank CEAE staff, especially Araceli Warren, Ken LaFon, and Pamela Halstead Williamson (past staff) for their help and support.

In addition, special thanks to my fellow graduate students and post-docs I greatly appreciate them.

TABLE OF CONTENTS

LIST OF TABLES

LIST OF FIGURES

Chapter 1 INTRODUCTION

1.1 FRACTURE TOUGHNESS OF COMPOSITE MATERIALS

As civil engineers, our major concern is the building of functional environments (i.e., buildings and infrastructure) which survive during and after any disruptive events [1]. To engineer such environments efficiently we must take a closer look at the materials we use [2]. Concrete, ceramic, and other quasi-brittle materials contain pre-existing cracks and complex material structure on various internal length-scales [3]. This is because the material is not homogeneous; concrete consists of aggregate "particles", cement paste "mortar," and interfacial transition zone, the "weakest link" [4]. Cracks occur because of inconsistencies of the material types that range from a brittle solid to soft gel. Cracks coalesce and propagate throughout the material structure for variety of reasons (mechanical loading, temperature changes, etc.) and can cause deterioration of infrastructure [5]. Based on the Federal Highway Administration inspection [6], bridge decks are more exposed to cracking and deterioration than other structures due to direct exposure to the service environments, causing aging which has become a safety concern [7]. A methodology is introduced in this dissertation to relate the macrostructure deformation to micro-crack growth and coalescence at the microstructure scale during the failure process in heterogeneous materials. Design of concrete structures during 1900-1930, was based on elastic no-tension analysis. Later on, specifically during 1940-1970, plastic limit analysis was introduced to the concrete design structures. It is expected that the introduction of fracture mechanics could be incorporated into the design of concrete structures, but this has yet to be implemented [1]. A key challenge to incorporating fracture mechanics into design is the lack of a simple forward-design equation for the composite material microstructures found in construction. Existing numerical models cannot

be specified by code as a design approach, and closed-form solutions are required which link to standardized material tests. In the past two decades, many computational methods for fracture analysis have been elaborated [8-11]. The effect of increasing volume fraction of inclusions on the fracture resistant of composite materials was studied by many researchers [12-14]. Most engineering materials are heterogeneous with complex microstructure. Therefore, considering material microstructure is an important factor in understanding the failure process that may occur at different length scales [15-17].

1.2 MOTIVATION

The reliability of any structure is a function of its resistance to fracture. While structures may be designed to control the generation of damage within the material, this thesis will take a closer look at designing the structure of the material on the microscale to discourage damage evolution. As such, the focus is on incorporating the effect of interactions between the stress field caused by inclusions within the material matrix and the stress concentration of a characteristic crack. By applying Linear Elastic Fracture Mechanics (LEFM) concepts in a cracked body of arbitrary shape subjected to Mode I loading, a theoretical formulation will be presented where statistically grouped particle packing scenarios and fracture response are linked. This effect is currently missing from fracture formulations. Studying the effect of inclusion statistics on the fracture resistance of a heterogeneous material can assist us with gaining insight and understanding on how the stress concentration can be reduced within the material, thus reducing the initiation of cracks [18]. In macro-scale models of the global behavior of heterogeneous materials, homogenized properties may be assumed, ignoring heterogeneity by averaging material properties [19]. However, this homogenization doesn't give an accurate representation in scenarios when the stress concentrations initiated during failure are localized within the micro-structure. The properties and

the micro-scale spatial distribution of different phases in such material will determine the overall macroscopic behavior of the heterogeneous material. To explicitly address the correct fracture toughness of a composite, the individual components of the material should be considered. Fracture and failure is typically initiated at regions with weaker material properties, such as the interface between the matrix and inclusions [20]. To address this, a system of individual inclusions, cracks, and voids needs to be considered along with a methodology that relates the macrostructure deformation to micro-crack growth and changes in the stress field at the microstructure scale. Evaluating the fracture toughness of the system by using a micro- indent or scratch test probes these interactions while classical fracture tests determine the fracture response with stress distributed over a local region of the sample [1]. In this context, Figure 1.1 illustrates a summary of different materials tested using standard macro- and micro- tests. The data shows a discrepancy in the material's fracture toughness when using macro and micro-scale tests. Fracture toughness is classically defined as a material property [21], and as such should be independent of the length scale it is tested on.

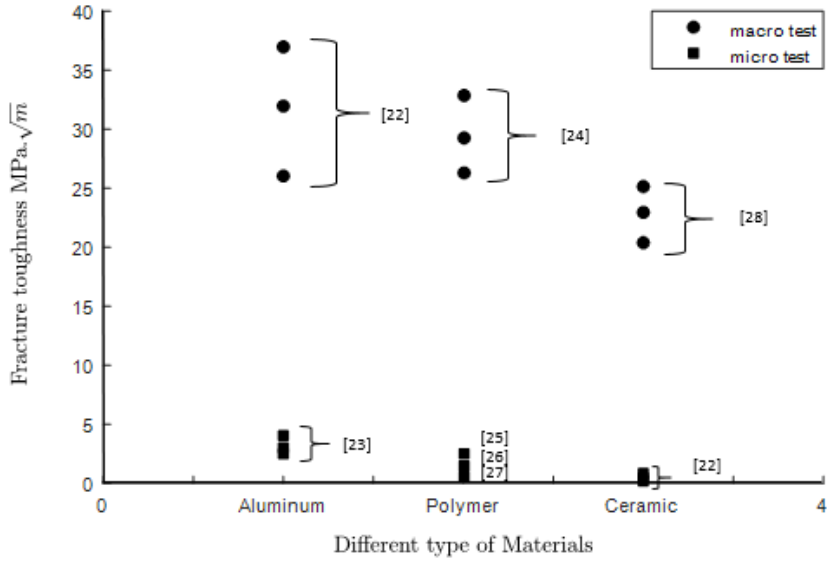

Figure 1.1. A summary of different materials tested using macro and micro tests

The data shows a discrepancy in the material's fracture toughness when using macro and micro-scale tests. This discrepancy of up to an order of magnitude reveals that either a reformulation of the fracture toughness equations derived from small scale tests is required or a redesign of standard tests to account for micro-scale behavior is needed.

1.3 RESEARCH VISION AND OBJECTIVES

The focus of this research is to address and provide a methodology to answer the following open questions:

1. What type of test gives us the most representative fracture parameters for a random composite material?

   Figure 1.2 illustrates the methodology used to answer this question. We first built a model system that represents a disordered composite. Standard 3-point bending and scratch tests were conducted for comparison. Numerical and analytical investigations of the different populations of inclusions were generated to investigate the microstructure effect.

2. Can we quantify the relation between the degree of randomness and the tendency to propagate the cracks using spatial statistics?

   The flowchart in Figure 1.3 shows the methodology used to answer this question using analytical and numerical methods.

3. How well can closed-form LEFM equations, explicitly considering inclusions, pores, and micro-cracks, match experimental cement fracture?

Figure 1.4 illustrates the methodology used to compare our results to an experimental study of the impact of injecting micro-particles into aged cement paste for sealing purposes and to improve the durability and sustainability of cement paste.

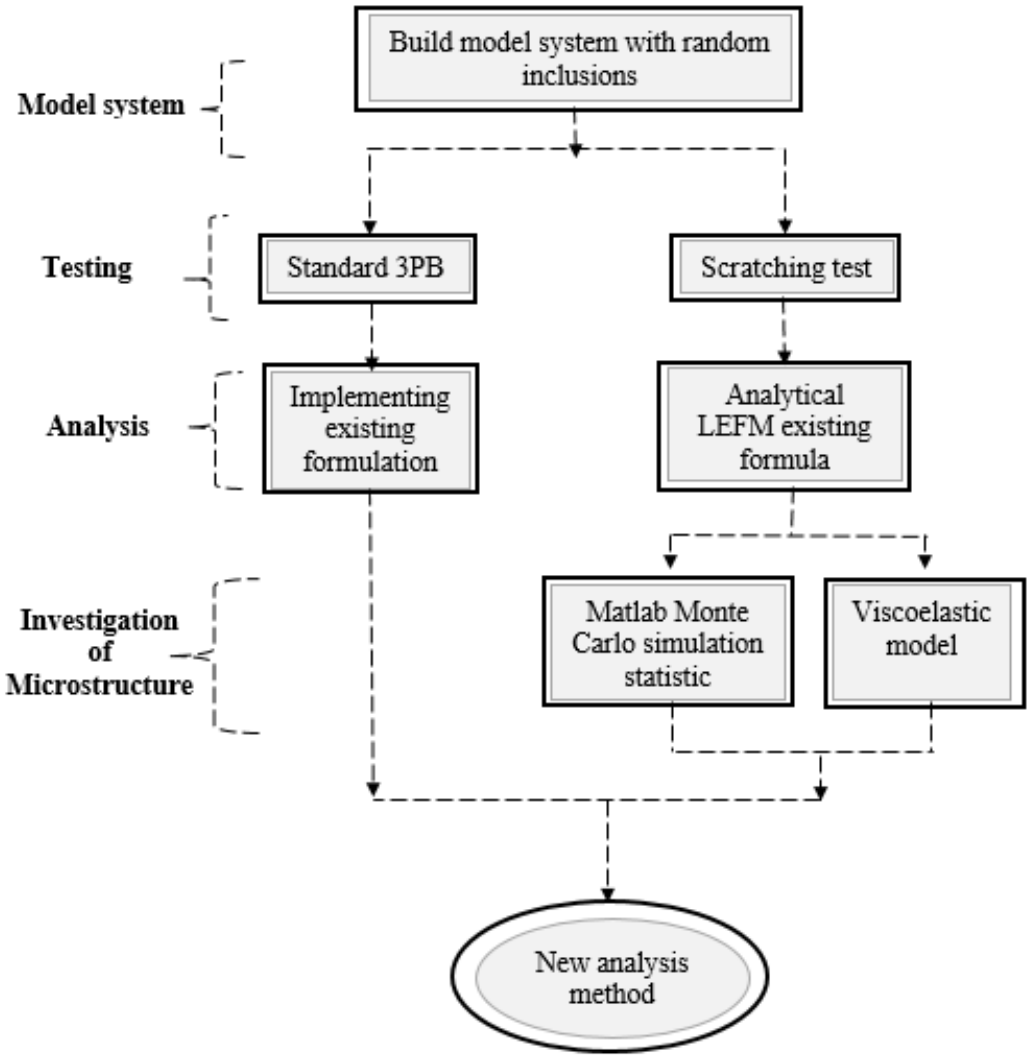

Figure 1.2. A roadmap for developing the answer for the first open question

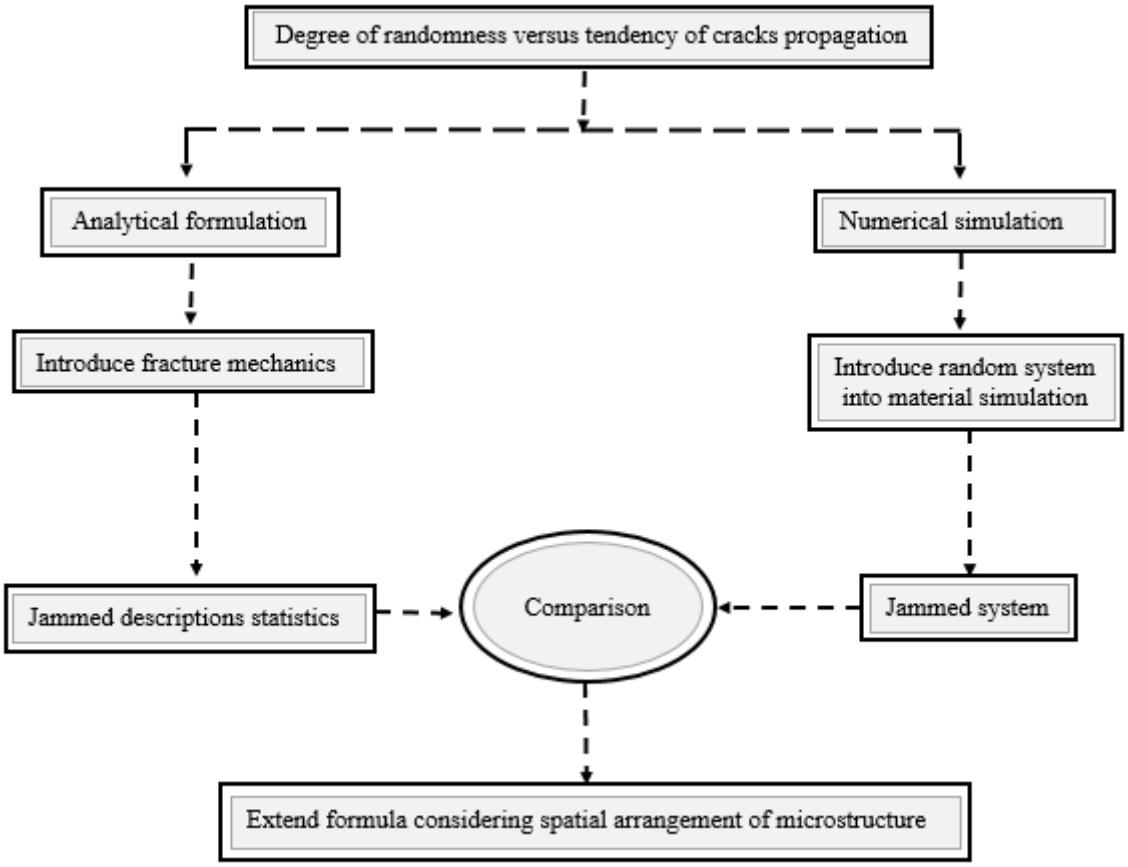

Figure 1.3. A roadmap for developing the answer for the second open question

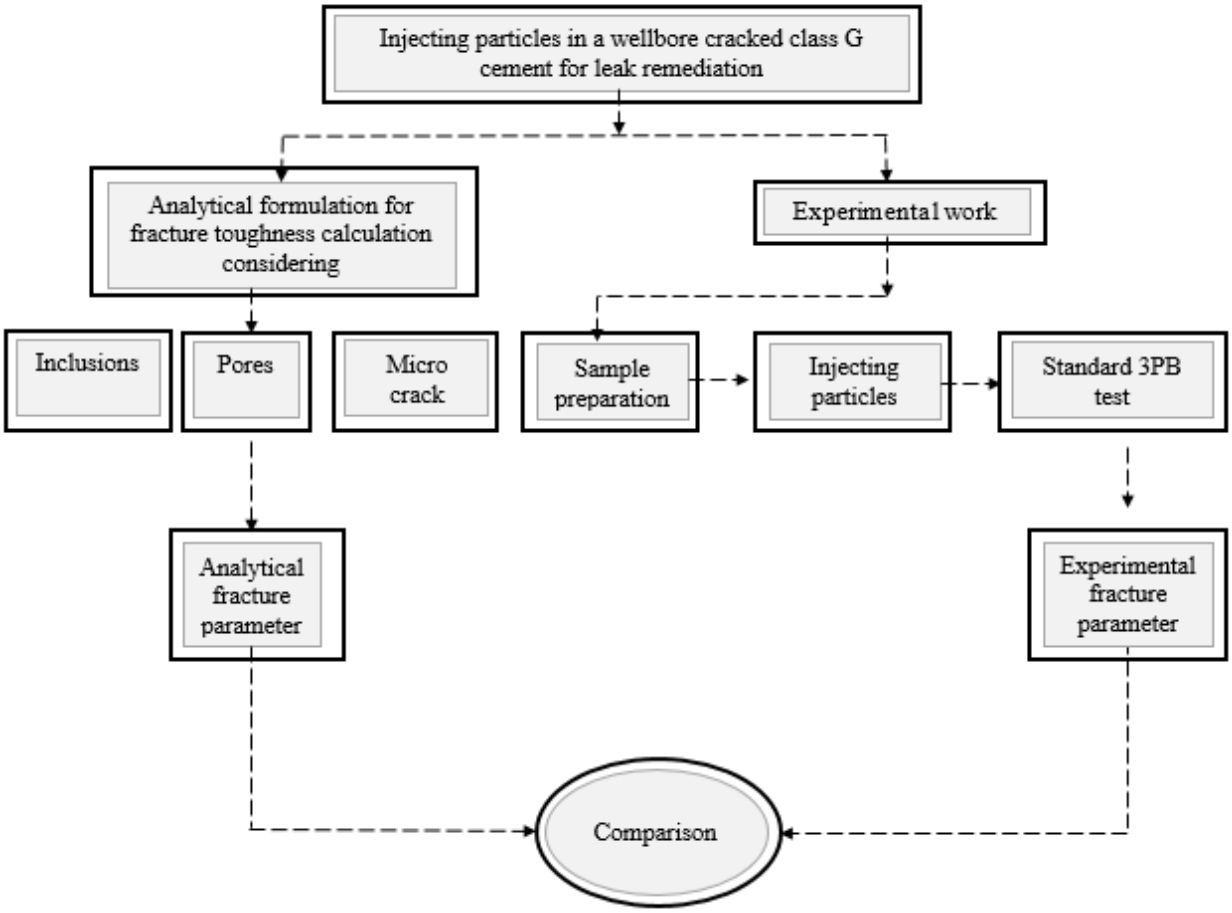

Figure 1.4.A roadmap for developing the answer for the third open question

1.4 DISSERTATION OUTLINE

This thesis introduces a methodology to consider material heterogeneity in a region in front of the crack tip experimentally, theretically, and numerically. This dissertation represents a compilation of four studies that combine to evaluate and quantify the influence of: a) the impact of inclusions on fracture toughness experiments b) the spatial statistics of matrix inclusions c) nanoparticle injection on fracture resistance of composite materials.

Chapter 2: Literature review and background of previous and relevant work to this research starting with the mathematical study of inhomogeneity problems which attracted Eshelby.

Chapter 3: Selectively studies the impact of microstructure on macro-scale fracture toughness. This chapter presents an experimental and theoretical investigation of the fracture toughness of a representative composite material consisting of glass beads embedded in epoxy using micro-scratching and conventional three-point bending tests. This chapter has been presented and published in the *9th International Conference on Fracture Mechanics of Concrete and Concrete Structures* (Al Wakeel and Hubler 2016).

Chapter 4: Investigates the discrepancy of fracture toughness values found in the previous chapter, which were derived from micro-scale and macro-scale tests. This discrepancy could be described by considering the effect of micro-structural defects in front of the crack tip in micro-scratch tests that have not been explicitly modeled. This chapter has been submitted as an article for review by the *Journal of the Mechanics and Physics of Solids.*

Chapter 5: Identify guidelines for selecting particles to seal cracks in aged class G cement, based on their impact on the mechanical behavior of the matrix. By incorporating particles, we can improve the durability and sustainability of cement, but the particle content must be selected to avoid further cracking. This chapter will be submitted for publication in the Journal of *Construction and Building Materials.*

Chapter 6: Argue that the degree of spatial ordering, disordering and packing of the particles will affect the fracture toughness of the heterogeneous material. By exploring a set of simple systems of different particle packing configurations, we can quantify the packing effect on the material's fracture toughness. This chapter will be submitted for publication in the Journal of *Construction and Building Materials.*

Chapter 7: Summary and conclusions of this thesis are presented in this chapter.

Chapter 2 LITERATURE REVIEW

2.1 LITERATURE REVIEW

2.1.1 FRACTURE MECHANICS FUNDAMENTALS

Fracture toughness is used to measure the resistance to extension of a crack. Inglis [29] (1913) introduced the first mathematical formulations of fracture mechanics by analyzing a plate containing an elliptical hole under uniform tensile stress; he noticed that the apex of the major axis had a maximum stress occurrence where the radius of curvature was minimum [30, 31]**.** In 1920 Griffith [32] applied the concept of energy conservation to a glass plate containing a central crack, stating that the glass was not perfect and the existence of flaws with a sharp tip in the microstructure would increase the stress concentration in the body. He proposed that it would be possible to generate a macroscopic load displacement curve as the crack length increased from a length a to $a+\Delta a$. Furthermore, Orowan (1952) and Irwin (1957) [33] extended Griffith's work to metals: Irwin developed the energy release rate concept, while Orowan formulated a similar modification to Griffith's theory independently [1]. Irwin's colleagues brought attention to Westergaard's paper [34] (published in 1939) long after it was published and that helped them further the findings of Orowan and Irwin. Westergaard was able to define a constant named stress intensity factor through his analysis of the stress field and displacement ahead of a crack tip using the semi inverse technique. The semi inverse technique is based on the energy release rate used later by Irwin to define the stresses and displacements in his work [30]. The stress intensity factor, as defined by Westergaard, has a subscript that defines the mode of the loading (K_I, K_{II}, K_{II}). There are three different types of failure mode: mode I (opening), mode II (sliding) and mode III

(tearing), as shown in Figure 2.1. The opening mode (mode I) and shearing mode (mode II) can be categorized as in-plane problems, while the tearing mode (mode III) is an out-of-plane problem [30]. A material's failure can also be due to mixed modes [30].

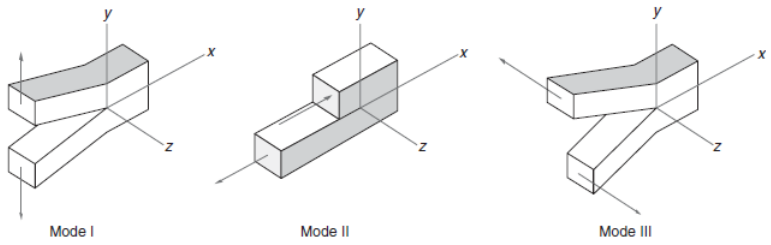

Figure 2.1. Types of fracture modes [30]

Failure can occur based on fracture theory when the applied stress exceeds the material resistance to fracture. Krafft, Sullivan and Boyle [31] (1962) introduced the R-curve. R-curve is one of the measures of fracture toughness; it is a material property and does not depend on the cracked body geometry. They argued that each material has a distinctive R-curve at a particular thickness under a given loading rate and temperature, and has nothing to do with the initial crack length and specimen size and shape.

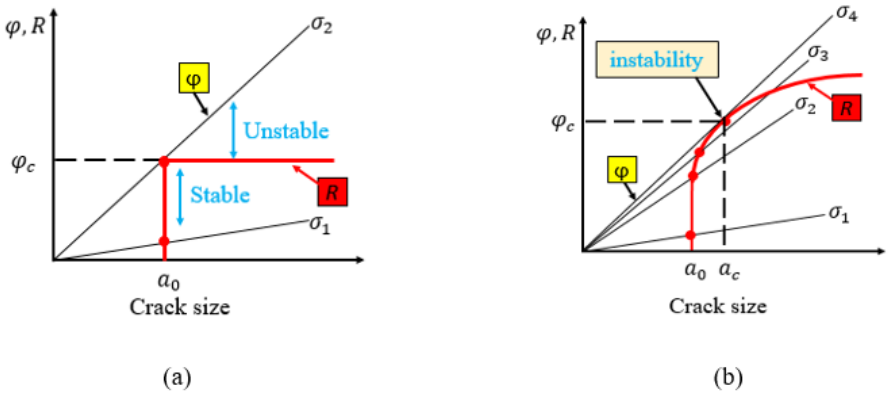

Figure 2.2. Schematic R-curve concept (a) brittle material behavior (b) ductile material behavior [31]

Figure 2.2 illustrates the R-curve concept; the material resistance versus the crack growth. For a brittle material, Figure 2.2 (a) shows when the applied stress is σ_1 the crack is stable. When the

applied stress is increased to σ_2,it will result in propagation of the crack in an unstable manner. However, the material resistant and will remain constant. The unstable crack growth will cause the material to fracture. This is not the case in the ductile material Figure 2.2 (b); when the stress reaches σ_2 the crack will grow a small amount. Upon further increasing the stress to σ_3, the crack length will continue to increase in a stable manner. When the stress reaches σ_4, the driving force is the tangent of the R curve. Finally, when the rate of the change in the driving force is equal to the slope of the R curve, unstable crack growth will be observed in the material. The circumstance of stable and unstable crack growth is illustrated below:

$\varphi = R$ crack growth (2.1)

$\frac{d\varphi}{da} \leq \frac{dR}{da}$ stable crack growth (2.2)

$\frac{d\varphi}{da} > \frac{dR}{da}$ unstable crack growth (2.3)

2.1.2 GOVERNING EQUATIONS FOR FRACTURE TOUGHNESS

A stationary crack is considered, where the Cartesian coordinates x and y are centered at the crack tip. It is referred to as a singular problem since the stress at the tip tends to infinity [31]. For any two-dimensional problem (plane strain or plane stress), the stress field near the crack tip is dominated by the inverse square root singularity as given by the following equation [34].

$$\sigma_{ij} = \frac{K_I}{\sqrt{2\pi r}} f_{ij}(\theta) \quad (2.4)$$

where K_I is the stress intensity factor, r and θ are the polar coordinates whose origins are defined located at the crack tip and f_{ij} is a dimensionless shape function expressing the geometric parameters, f_{ij} is different for different failure modes as defined in Figure 2.1. σ_{ij} is the component

of Cauchy stress tensor, in this study, the only component of the Cauchy stress that will be considered is σ_{xx} since the induced damage will propagate in the direction of $x = +\infty$, $dy = 0$. The stress field equation in the neighborhood of a crack tip for opening in mode I in an isotropic linear, elastic material is [30]:

$$\sigma_{xx} = \frac{K_I}{\sqrt{2\pi r}} \cos\left(\frac{\theta}{2}\right)\left(1 - \sin\left(\frac{\theta}{2}\right)\sin\left(\frac{3\theta}{2}\right)\right) \tag{2.5}$$

Williams [35] included a term called uniform stress in the x-direction ($\sigma_{0x} = 4C_{12}$) which is parallel to the crack plane. C_{12} is an elastic constant used in the compliance matrix [35]. The matrix of coefficients contains nine elastic coefficients are summarized by the matrix below [35]:

$$\begin{bmatrix} C_{11} & C_{12} & C_{13} & 0 & 0 & 0 \\ C_{12} & C_{22} & C_{23} & 0 & 0 & 0 \\ C_{13} & C_{23} & C_{33} & 0 & 0 & 0 \\ 0 & 0 & 0 & C_{44} & 0 & 0 \\ 0 & 0 & 0 & 0 & C_{55} & 0 \\ 0 & 0 & 0 & 0 & 0 & C_{66} \end{bmatrix} \tag{2.6}$$

By including the uniform stress term in a body containing a single crack for mode I failure, the stress field expression becomes:

$$\sigma_{xx} = \frac{K_I}{\sqrt{2\pi r}} \cos\left(\frac{\theta}{2}\right)\left(1 - \sin\left(\frac{\theta}{2}\right)\sin\left(\frac{3\theta}{2}\right)\right) + \sigma_{0x} \tag{2.7}$$

This term will not be included in the analysis as Irwin showed that this stress has no influence on the stress intensity factor and contributes nothing to the crack opening stress, although it may slightly affect the size of plastic zone [31]. Rice [36] indicated that the consideration of the σ_{0x} term can result in an accurate estimation for the crack tip plastic zone radius for a particular geometry. Additionally, Rice [37] proposed the J-Integral concept given by the following equation to estimate the stresses acting around a moving crack tip:

$$J = \int \left[\mathrm{W}\,\mathrm{dy} - \mathrm{T_i}\,\frac{\partial \mathrm{u_i}}{\partial \mathrm{x}}\,\mathrm{ds}\right] = 0 \tag{2.8}$$

where W = strain energy density, $T_{i\,\mathrm{i}}$ = Traction vector-outward normal acting to the contour Γ in Figure 2.3, u_i = displacement vector, x, y = Cartesian coordinates (y is the axis perpendicular to the crack), ds = arc element along the Γ, Γ = integration path surrounding the crack tip (anti-clockwise).

He began his analysis by considering a notched homogenous linear or non-linear elastic flat body restricted to two-dimensions (i.e. the stresses would be only the x and y directions). He defined the J-Integral by drawing a path counter-clockwise from the lower crack face to the upper crack face as shown in Figure 2.3. This path depends only on the crack tip singularity in the local field. Using Green's theorem, he proved that this definition of the J-Integral is path independent (equal to zero) for any closed path.

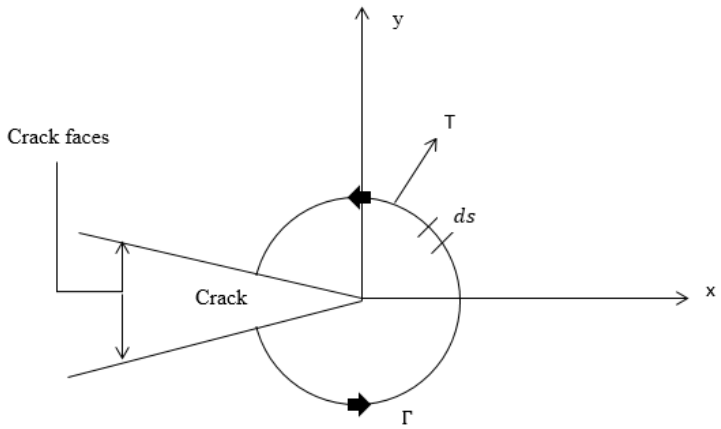

Figure 2.3. J-integral contour definition. Arbitrary path around a crack tip and coordinate definitions used in the integral formula.

His introduction of the J-Integral has since become one of the best methods to calculate the stress intensity factor over any path around the crack tip. In this study the concept of J-Integral and LEFM is used to estimate the stress intensity near the crack tip considering notched two-dimensional homogenous linear elastic body. However, the J-Integral is used to evaluate the energy release rate $\mathcal{G}$ using the contour integral surrounding the crack tip [1]:

$$J = \mathcal{G} \tag{2.9}$$

where $\mathcal{G}$ is the amount of the potential energy stored in the system which is released when the crack propagates. Using the Griffith-Irwin relationship:

$$K_c = \sqrt{E'\mathcal{G}} \tag{2.10}$$

We find that

$$\mathcal{G} = \frac{{K_c}^2}{E} \tag{2.11}$$

$$J = \frac{{K_c}^2}{E} \tag{2.12}$$

where E is the material modulus of elasticity.

2.1.3 LINEAR ELASTIC FRACTURE MECHANICS MODEL FOR SCRATCH TEST

Linear Elastic Fracture Mechanics (LEFM) was applied in this dissertation to relate the internal forces to material fracture toughness. LEFM can be applied to any material when certain requirements are met [1]. These requirements indicate that the material is elastic excluding a very small region (a point) at the crack tip. Therefore, in this section we will present the mathematical calculations behind using LEFM. Irwin [33] stated that the inelastic zone size can't be zero; therefore, it must have finite size R_c as shown Figure 2.4. To estimate the elastic distribution along the crack line, Irwin (1960) estimated the zone around the crack tip where the material shows yielding and hence no stress singularity exists. In this case at a distance R_c from the crack tip the stress σ_{yy} is greater than the yield stress σ_y as Figure 2.5 shows. The distance R_c represents the plastic zone size, for mode I failure it can be estimated as follows [33]:

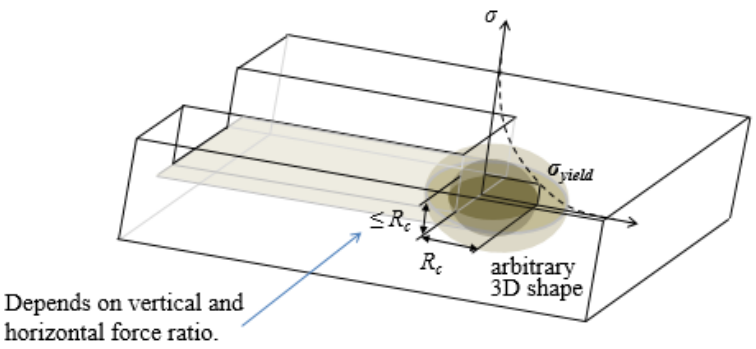

Figure 2.4. Size of plastic zone

$$R_c = \frac{1}{2\pi}\left(\frac{K_{IC}}{\sigma_y}\right)^2 \ll \text{specimen dimension, } \mathrm{D_s} \tag{2.13}$$

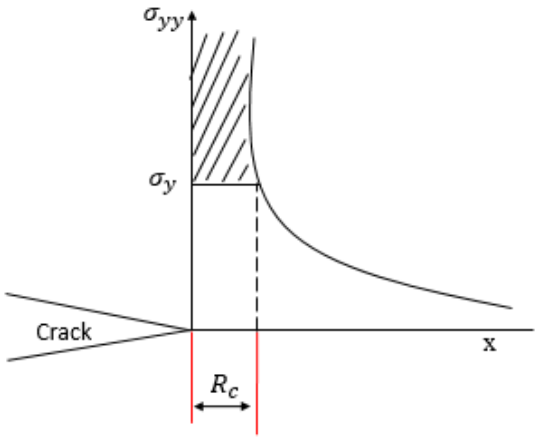

Figure 2.5. Irwin estimation of plastic zone

To calculate the plastic zone size, tension tests were performed to measure material yield stress. The specimens were cast in a dog-bone shape mold as illustrated in Figure 2.6 and tested at room temperature using an Instron testing machine. Type I standard specimen's dimension was used per ASTM D638 [38]. The testing speed was 0.0416 mm/sec under displacement control mode. The calculated yield stress was 40, 40.1, 40.5 and 41 MPa for the polymer with 0%, 5%, 25% and 50% glass beads respectively. Then, the size of the plastic zone R_c for each volume fraction was

calculated using equation 2.13 and was found to be: 0.4,0.37,0.27 and 0.21 mm. For LEFM to be applicable, R_c should be smaller than the specimen's dimension, D_s.

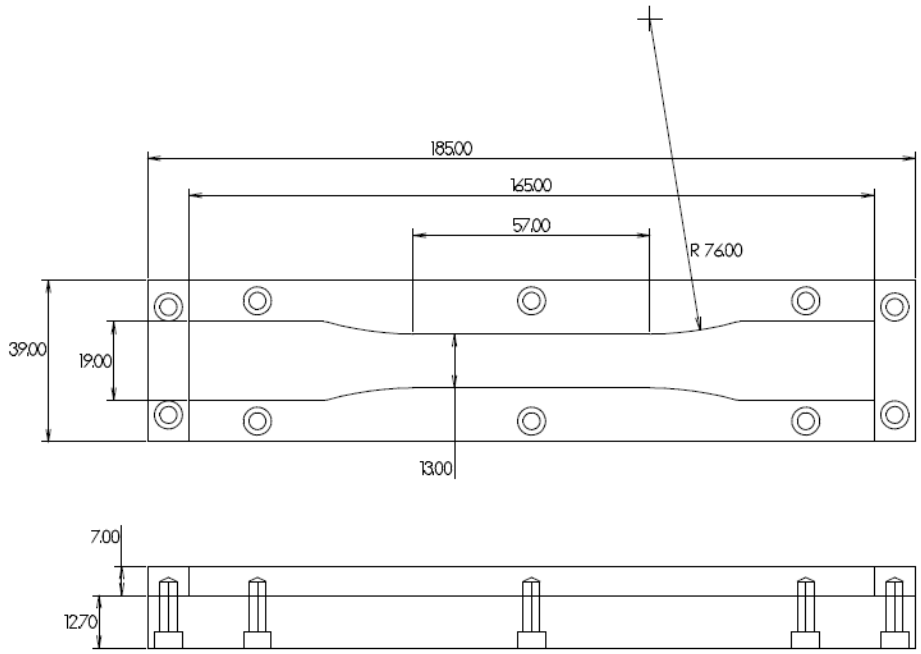

Figure 2.6. Tension test mold

The results show that LEFM can be applied to this test since the size of the plastic zone R_c is smaller than the smallest specimen dimension (D_s=10 mm). In this study we conducted the scratch test with increasing depth as the probe is pushing into the material shown in Figure 2.7.

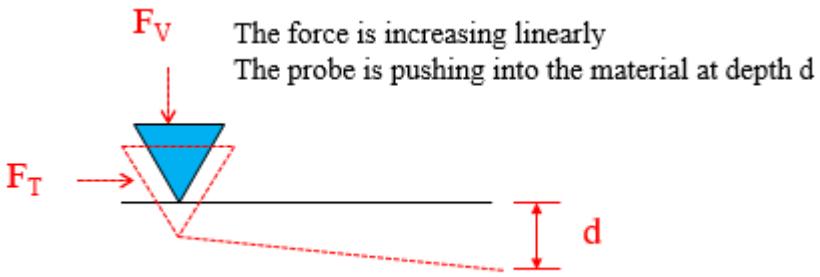

Figure 2.7. Schematic of scratch test

Using the equations derived in [39] this experimental setup allows us to fit the size effect curve for the material from each scratch. The characteristic size of the problem increases when as the

probe goes deeper into the material. Thus, each data point collected during the scratch test is one data point on the size effect curve, Figure 2.8. Figure 2.8 represents the energetic size effect law which scales the material behavior limits of plasticity along the horizontal line and the descending line of slope $(-1/2)$ for LEFM. To quantify the fracture properties of these materials from scratch testing, the force to probe-depth scaling is related to the size-effect analysis using the energetic size effect law [39] at the microscale.

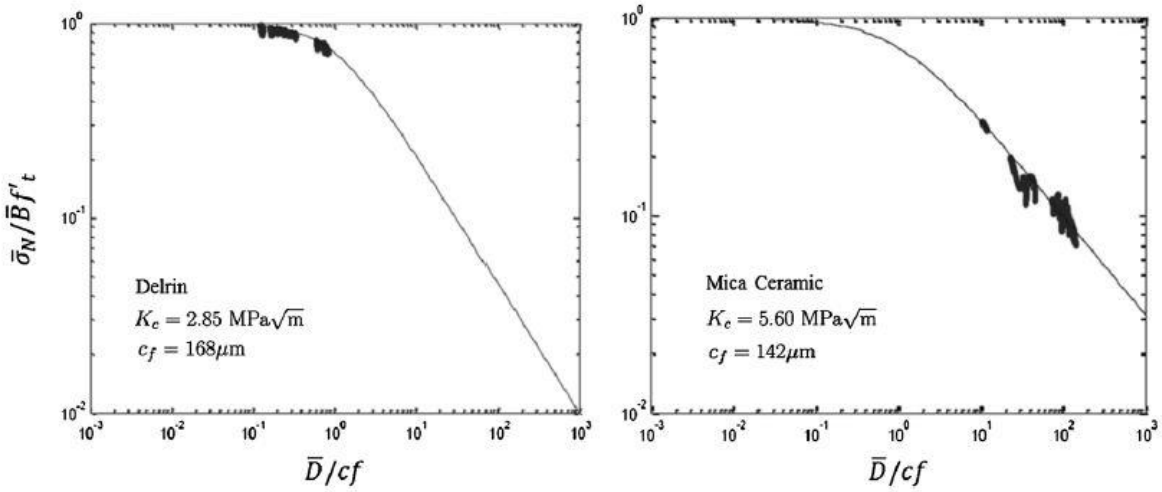

Figure 2.8. Microscratch data from Delrin and glass ceramic materials are shown on size effect curve [39]

Baz$\tilde{a}$nt's size effect law is given by equation 2.14.

$$\sigma_N = \frac{B\sigma_y}{\sqrt{1 + \frac{d}{d_0}}} \tag{2.14}$$

where σ_N is the nominal stress, B is a coefficient, σ_y is the material yield strength, d and d_0 is the size and the critical size of the structure respectively. The scratch test formulation of this equation dimensionlessly scales the strength and size axes of this relation to match the scratch probe geometry with depth. According to the results obtained by [39] for scratching of shale rock, nonlinear fracture mechanics show similar results to LEFM assumptions when obtaining fracture

toughness values from the scratch test data. In addition, nonlinear fracture mechanics does not explicitly address heterogeneity, only the average presence of microstructure, and thus results in the same discrepancy in fracture toughness when compared to the macroscale, which we are trying to address.

In the determination of the fracture toughness in the theoretical model we consider a single mode of fracture, mode I failure. We assume that the sole contribution to the energy change comes from the stress in the x-direction as the probe moves on the specimen's surface, letting the crack propagates horizontally. However, the derivations presented in this work can be generalized to consider all three modes of failure. This is important for cases in which the ratio of vertical and horizontal forces in the scratch tests are far from what was used in the case considered here. Most scratch testing devices currently have a limited range in force sensing capability, and thus cannot measure outside of a range that is mode I dominated. However, future devices optimized for this testing method may be optimized and could produce mode II and III failure, as is typically seen in larger surface grinding and scratching applications (such as those seen in mining).

We used Westergaard's [34] equation to estimate the stress field in front of the crack tip and the J-integral to evaluate the energy release rate under the conditions of plane strain, the Griffith- Irwin relation [32], which yields:

$$\mathcal{G} = \frac{(1 - v^2)K_I}{E} \tag{2.15}$$

where $\mathcal{G}$ is the energy release rate, E is the Young's modulus of elasticity, v is the Poisson's ratio and K_I is the mode I failure. Thus the J-integral provide the expression of the energy release rate:

$$J = \frac{(1 - v^2)K_I}{E} \tag{2.16}$$

With a more general solution, for the scratch test the energy release rate can be linked to mode I and mode II (Figure 2.9) as considered in [40-42] to evaluate the fracture resistance of the material using the following equation:

$$J_{total} = J_I + J_{II} = \frac{(1-v^2)}{E}\left({K_I}^2 + {K_{II}}^2\right) \tag{2.17}$$

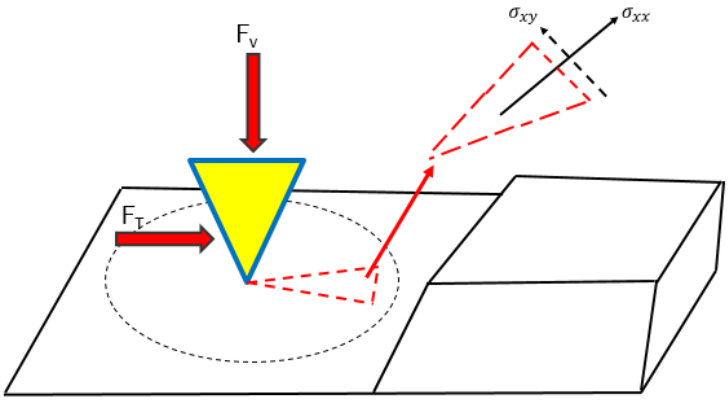

Figure 2.9. Possible consideration of mode I and II to evaluate material fracture toughness

The J-integral can be obtained as a mixed mode I, II and III, through superposition. Figure 2.10 illustrate the stresses that need to be considered to obtain the total J-integral using the following equation [43,44]:

$$J_{Total} = J_I + J_{II} + J_{III} = \frac{(1-v^2)}{E}\left({K_I}^2 + {K_{II}}^2\right) + \frac{1}{2G}{K_{III}}^2 \tag{2.18}$$

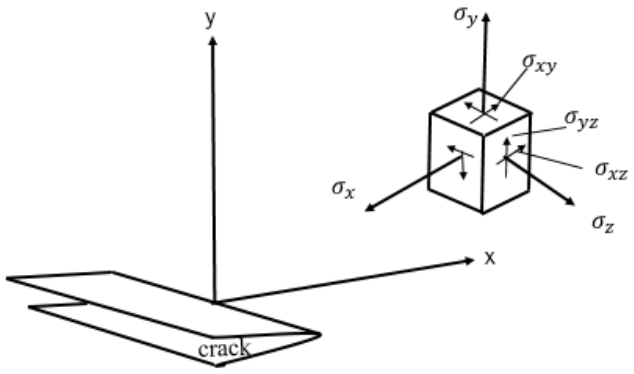

Figure 2.10. Crack tip stress field

The ratio of forces used in this dissertation cause J_I to dominate this expression [5]. Future work can directly extend the application of the equations derived herin to other force ratios by superposition of the J-integral values given in equation 2.18. In this dissertation, scratch tests were done by increasing the vertical applied force as the probe moves across the specimen's surface. Accordingly, the scratch depth increases as shown in Figure 2.7.

The influence of friction between the probe and specimen's surface has been investigated by Bard [45]. To illustrate the effect of friction, from the scratch data, experimental and analytical investigations were carried out on a 2D model of a cohesive material in mode I. The coefficient of friction is defined using equation 2.19, which is the ratio between the friction force to the normal force as illustrated in the Figure 2.11.

$$\mu = \frac{F_T}{F_v} \tag{2.19}$$

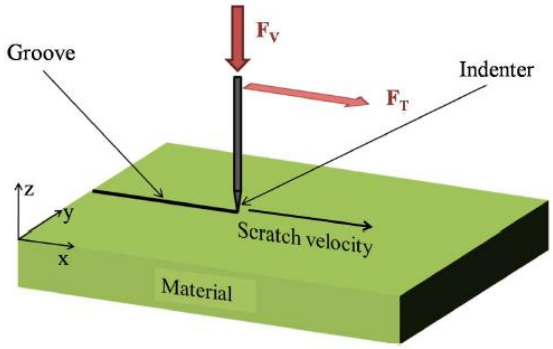

Figure 2.11. Graphical representation of the scratch test [45]

F_T and F_v are measured in the scratch test, based on the lower bound theory and a closed form solution from this study yields that there no influence of friction on the fracture toughness parameter. By comparing the lower bound yield design approach and FE methods, the influence of friction at the blade–material interface was investigated. A series of 20 scratch tests were performed on cement paste material and the effect of friction was molded by considering additional

degree of freedom θ'. The maximum value of the scratch hardness was found when θ' was equal to zero and a higher friction coefficient did not increase the scratch hardness.

Photo-elastic images [46] and Focused Ion Beam (FIB) imaging in Figure 2.12 shows that the propagation direction of surface contact-induced crack is lateral. Again, this suggested that mode I failure approximation is valid for the scratch test.

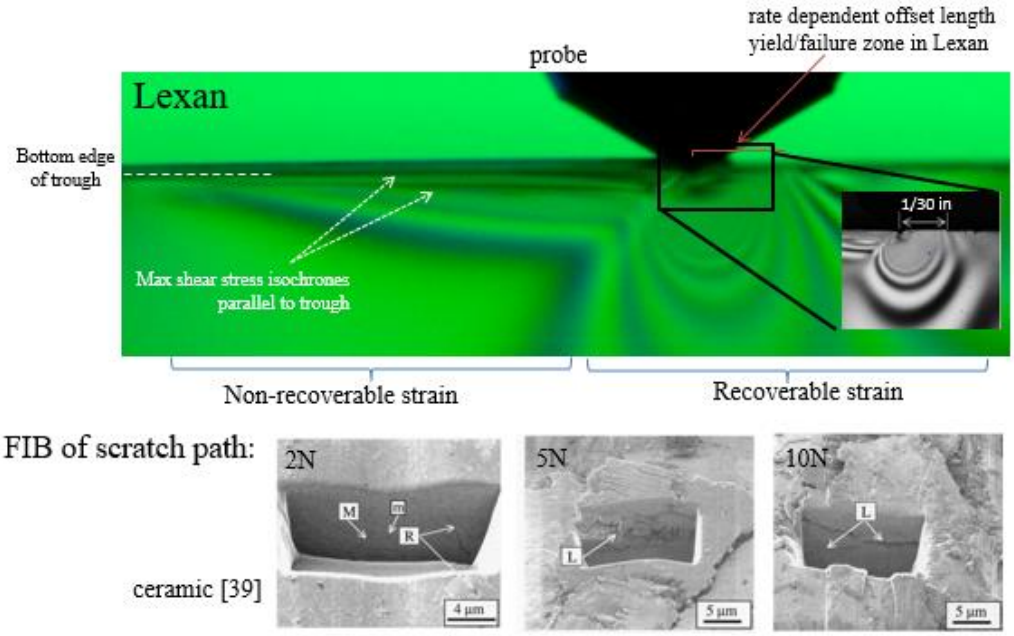

Figure 2.12. Photo-elasticity of Lexan scratch with circular polarizer [46]

2.1.4 IMPACT OF INTERACTION OF CRACK-INCLUSION ON FRACTURE TOUGHNESS

For a material made of inclusions embedded in a matrix, the existence of inclusions affects the deformations in the neighboring material during loading and generates stress concentrations [30]. The stress field of the crack and inclusion interact and impact fracture toughness measures of the material. Remote inclusions dispersed within the matrix can also have an impact on the fracture toughness of the material in a homogenized sense. Eshelby [47] transferred the inhomogeneous inclusion to a homogenous one by considering an inclusion which has the same properties as the

matrix. Others [48, 49] considered the explicit interactions between crack propagation and the inclusion-matrix. A study [50] was presented by several authors proposing that such an interaction yields stress shielding; reducing the stress intensity at the main crack tip. Their analysis considers the crack-inclusion problem using a global energy balance. It was found that for small inclusion sizes, crack growth required more energy because the energy release rate decreased as the inclusion size decreased for the same applied load. Also, higher crack speeds were found for weakly bounded inclusions compared to the strongly bonded case [51-54]. Most of these studies discuss the influence of the existence of one inclusion ahead of the crack tip but not the effect of the spatial distribution of more than one inclusion on the fracture toughness of the material.

This work addresses the need to simultaneously consider the near-field and far-field interactions of inclusions on crack growth in heterogeneous materials. The focus of this work is to develop a formula that considers the effect of the inclusions ahead of the crack tip and then compare the results with those that have been calculated from the standard three-point bend and the scratch tests on the macroscale to gain insight into the source of difference between fracture toughness values measured on different scales. First we look at the J-integral for a close contour near the crack tip. Then we introduce an inclusion in front of the crack tip to develop an analytical relation for a crack interacting with inclusions. A simple representation of the fracture process zone is proposed to study the effect of the volume of inclusions and their mutual interaction on the energy release of the crack.

2.1.5 SIMILAR WORK

Recently, Akono *et al.* [55-57] presented considerable work on using the scratch test to determination the fracture toughness. Akono [5] used the scratch test to measure forces and penetration depth by dragging an indenter probe along the surface material. In her work, she

proposed the following equation to calculate the fracture toughness [5] based on using the *J*-integral in front of the crack tip:

$$K_C = \frac{F_T}{[2p\ A_{LB}]^{1/2}} \tag{2.20}$$

where F_T is the horizontal force, p is a scratch probe parameter and A_{LB} is the horizontal projected load bearing contact area. This technique [5] was successfully applied on a wide range of materials including ceramics, polymers, metals, cementitious materials and rocks. Akono [5] proposed equation 2.20 based on a J-contour analysis using LEFM. They were able to link the scratching force and penetration depth with the fracture toughness by considering that in the scratch test the crack grows horizontally as the probe moves on the specimen surface as shown in Figure 2.13. The fracture toughness is derived as follows:

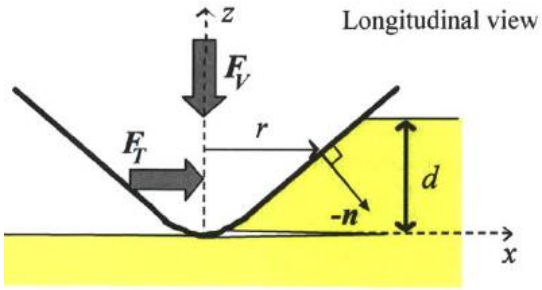

Figure 2.13. Axisymmetric scratch probe geometry [5]

$$\sigma_{xx} = \frac{F_T}{A} \tag{2.21}$$

$$F_T = \int \sigma_{xx} * n_x ds \tag{2.22}$$

Akono combined the stress equation (equation 2.21) with the energy density equation ($\mathcal{G} = \left(\frac{1}{2}\right) \kappa\sigma_{xx}^2/E$, to obtain the following equations [5]:

$$\mathcal{G} = \frac{\kappa}{2pA_{LB}E} F_T^2 \tag{2.23}$$

$$\mathcal{G} = \frac{K^2}{E} \tag{2.24}$$

$$K = \frac{F_T}{\sqrt{2pA_{LB}}} \tag{2.25}$$

where $\mathcal{G}$ is the energy release rate, x is the scratch direction, p is the perimeter of the probe, E is the Young's modulus, $\kappa = 1$ in plane stress and A_{LB} is the horizontal projected load bearing contact area shown in Figure 2.14. It can be calculated using the following equation [5]:

$$A_{LB} = \frac{2b\epsilon}{\epsilon + 1}\left(\frac{d}{b}\right)^{(1/\epsilon)+1} \tag{2.26}$$

where d is the scratch depth, b is the proportionality factor and ϵ is the homogeneous function described in Table 2.1.

Table 2.1 Typical values for the proportionality factor b and the homogeneous function ϵ

Probe type	**b**	**ϵ**
Spherical	2	1/(2R)
Cone	1	$\cot\theta$
Flat	$\rightarrow +\infty$	$(1/R^{\epsilon-1})$

The probe perimeter can be calculated using the following equation [5]:

$$p = \beta \left(\frac{d}{b}\right)^{1/\epsilon} \tag{2.27}$$

where p is the probe perimeter and β is dimensionless parameter defined in the following equation:

$$\beta = 2\int_0^1 \sqrt{1 + (\epsilon d)^2 \left(\frac{d}{B}\right)^{-2/\epsilon} x^{2\epsilon-2}}\, dx \tag{2.28}$$

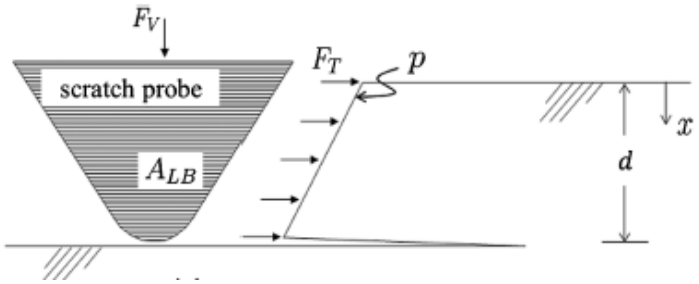

Figure 2.14. Microscratch configuration showing the projected horizontal area

In this work, scratch testing was performed by using a Rockwell diamond indenter shown in Figure 2.15. The scratch probe parameters used in this test are listed in Table 2.2.

Table 2.2. Scratch probe parameters

Indenter parameters	
Type	Rockwell
Material	Diamond
Radius (μm)	200

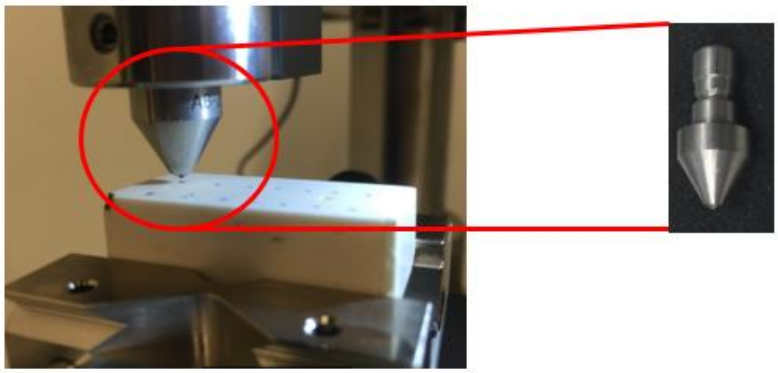

Figure 2.15. Rockwell diamond probe image

In her most recent work [55] Akono showed that, by combining the scratch and micro-indentation tests, we can accurately estimate the fracture toughness and the fracture energy. Those test results are essential for multi-scale modeling of the alkali-aggregate reaction. However, the formulation for energy release due to scratching applies the *J*-integral in front of the crack tip, and in doing so assumes a homogenous stress field in front of any crack tip that is generated. This ignores the local effect of the inclusions on this stress field. This work tests the validity of this assumption. Akono *et al.* [57] claimed that she accounted for the heterogeneity via the specimen preparation method and the test parameters. Her method is applied to gas shale system, and required to be combined with imaging technology. It wasn't very clear how she considered material heterogeneity in her work applicable to other materials.

Erwin *et al*. [22] studied the effect of increasing the filler content on the composite modulus. It has been found that the modulus and fracture parameters are improved with increasing volume fraction of the filler if the filler stiffer and stronger than the matrix. However, the quantification of the relevant microstructure in concrete introduces many experimental uncertainties. Many researchers have used a model composite system formed from epoxy resins filled with glass beads to evaluate the mechanical properties in terms of stress intensity fracture (K_I) and the energy release rate (G_I) [5, 14, 20, 22], but none have done so using scratch testing.

2.1.6 ESTIMATING NEAR AND FAR FIELD REGIONS

In this work, we introduced zones in which the local material microstructure is considered in determining near and far field contributions to the fracture toughness. These are different from the existing concept of a fracture processing zone. The zones considered here capture where the local arrangement of inclusions and stress shielding plays a role as shown in the Figure 2.16.

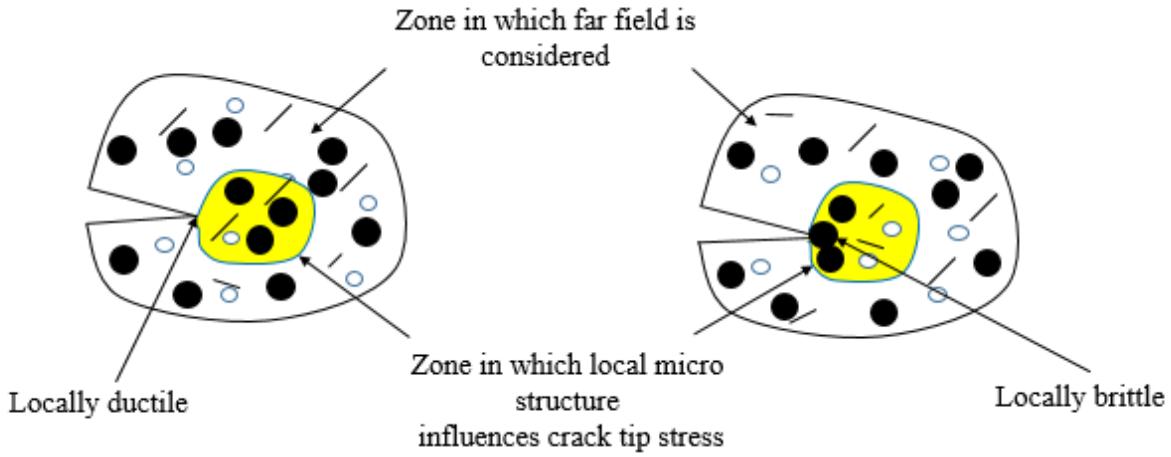

Figure 2.16. Zones in which the local arrangement of inclusions and stress shielding are considered

2.2 BACKGROUND

2.2.1 CONCRETE CRACKING

Because of the "stable growth of large cracking zones", concrete structures fail before maximum load is reached, which can produce large fractures [51]. By using mechanical analysis, we can model the crack zone ahead of the crack tip and study all the parameters that contribute to the initiation and growth of the cracks [1]. Concrete has existing micro cracks even before loading. This is due to the fact that the material is not homogeneous, temperature effect from hydration. To understand the fracture mechanisms in concrete materials, we need to scale down the concrete structure from the macroscale to microscopic interactions [18].

The fracture of concrete or cement based materials is strongly related to their micro-structure. Macro-cracks are the result of the growing cracks that were originally initiated in the microstructure. As previously mentioned, concrete is a multi-phase material since it consists of: hydrated cement paste as a binder, aggregate as filler, and the interface transition zone at which the binder and the filler are linked. When mixing water with cement powder the hydration process

starts. The main hydration product is the calcium Silicate Hydrate (C-S-H). It occupies between 50 - 60% of the solid volume in a completely hydrated cement paste. Therefore, C-S-H has a major role in determining the properties of cement paste and concrete material. In Portland cement paste, C-S-H is produced by the hydration of C_2S and C_3S as expressed in the equations below [5].

$$2C_3S + 6H \rightarrow C_3S_2H_3 + 3CH \quad (2.30)$$

$$2C_2S + 4H \rightarrow C_3S_2H_3 + CH \quad (2.31)$$

where: C_3S is tri-calcium silicate ($3CaO.SiO_2$), H is water molecule has the chemical formula (H_2O) di-hydrogen monoxide, $C_3S_2H_3$ is Calcium Silicate Hydrates ($3CaO.2SiO_2.3H_2O$), CH is calcium hydroxide Ca $(OH)_2$ and C_2S is di-calcium silicate ($2CaO.SiO_2$). The exact structure of C-S-H is not well known, and is strongly affected by the calcium-to-silicate ratio. In general, C-S-H forms in layers on the surface of cement particles. The layers have a huge surface area and interlayer spaces, which make C-S-H a highly porous material. At later ages, the C-S-H structure becomes more stable as the calcium to silica ratio is reduced. A well-documented fact is that the strength has an inverse relationship with the porosity, which is mainly determined by the structures of C-S-H. Usually, the strength of the transition zone is determined by the presence of voids, and under the impact of loads the voids will be prone to form cracks that will propagate and link the voids in the C-S-H structure and produce a visible crack [4].

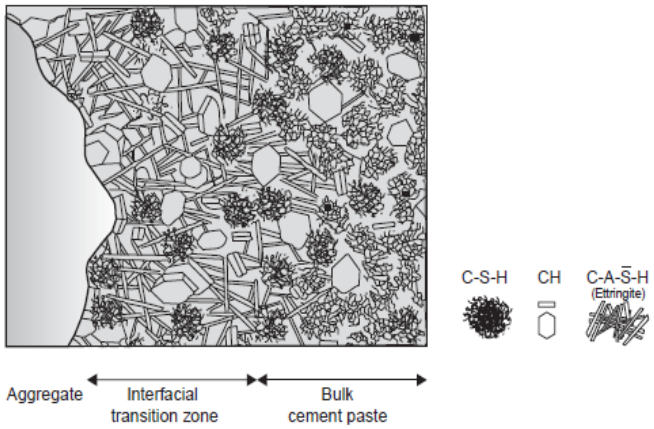

Figure 2.17 Diagrammatic illustrative of transition zone, aggregate and bulk cement paste in concrete [4]

2.2.2 FINITE ELEMENT SIMULATION USING ABAQUS

The Finite Element Method (FEM) is a commonly used and powerful technique for simulating mechanics of materials and structures. Numerical evaluations using the finite element method were carried out to determine the Stress Intensity Factor (SIF) by the well-known finite element software ABAQUS in this research. The ABAQUS software has the ability to solve both linear and non-linear problems, such as calculating the linear fracture parameter SIF using the domain integration method [58]. The ABAQUS software provides a procedure to calculate the J-integral parameter. For linear material response (as mentioned previously section 2.1.2), J-integral is related to the SIF as it measures the deformation intensity in front of the crack tip and the energy release associated with the crack extension. To perform J-contour analysis, several parameters need to be assigned such as crack tip, front and crack extension direction. Following ABAQUS guidelines, it is recommended that certain elements to be used around the crack tip / front, called singular elements. Singular elements are 2D biquadratic Lagrangian element (9 nodes) or 3D triquadratic Lagrangian (27-node). The benefit of these elements is that they contain the inverse square root of r everywhere within the element. For every FEM simulation, a convergence study needs to be conducted to ensure adequate mesh resolution for the stress field. For fracture problems, as the mesh size is reduced (number of elements increased), the change in the value of the SIF decreases [59-61].

2.2.3 FRACTURE TEST

2.2.3.1 FRACTURE TOUGHNESS USING ASTM STANDARD THREE-POINT TEST

Single Edge Notch Bend (SENB) geometry is typically used for fracture toughness assessment. A constant displacement load is applied above the centerline of the downward-facing notch while the

sample is supported equidistantly at both bottom edges. Specimen dimensions should be selected to satisfy ASTM 399 plane strain requirements [62]. The crack size to specimen width ratio is between 0.45 and 0.55 and a sharp crack is created by inserting a fresh razor blade into the notch. The fracture toughness can be determined using the ASTM 399 [62] standard formula for the three-point bend geometry from the following equation:

$$K_c = f\left(\frac{a}{w}\right)\frac{3PS\sqrt{a}}{2tW^2} \tag{2.32}$$

where: K_C is the critical stress intensity factor, P is the load at failure, S is the span length, a is the crack length, W is the specimen width, t is the specimen width and $f\left(\frac{a}{w}\right)$ is a numerical factor for this specimen that can be calculated using the equation below [14]:

$$f\left(\frac{a}{w}\right) = 1.93 - 3.07\left(\frac{a}{w}\right) + 14.53\left(\frac{a}{w}\right)^2 - 25.11 * \left(\frac{a}{w}\right)^3 + 25.80\left(\frac{a}{w}\right)^4 \tag{2.33}$$

2.2.3.2 FRACTURE TOUGHNESS USING MICRO SCRATCH TEST

The scratch test is a micro-scale test that can be used to evaluate the failure resistance of a material. It has been used extensively in geology and mining material characterization [63-65]. Scratching is performed by dragging a sharp Vickers indenter across the surface of the material under various loads [66]. Generally, the micro-scratch test has two advantages: there is no need to create a unique sample geometry and only a small sample is needed to run multiple tests. One of earliest uses of the scratch test was to measure material hardness [67]. Besides the hardness test, other studies have adopted this technique to determine the adhesion of coatings and the coefficient of friction [60]. Furthermore, the scratch test is used to account for the variation of crack depth below the scratch as a function of sliding velocity [61]. Recently Ulm & Akono used the scratch test to determine

the fracture toughness of different materials such as cement, shale and rock at a fine scale by assuming the probe drives a single crack in the material [5].

2.2.4 BAŽANT SIZE EFFECT

The change in specimen response with increasing size is defined as the size effect. This effect has been shown to stem from the quasi-brittle and heterogeneous nature of some construction materials during fracture. Studies of the size effect started in the 1970's, where the problem in modeling large structures like concrete dams and bridges for which there is a big difference in the scales between the real structure and lab tests. In larger size structures there is a higher probability of the existence of weak zones compared to the small size scale, which causes the energy dissipation to decrease as the sample size increases. There are two causes of this phenomenon. The first is due to the randomness in the material strength (statistics) and the second reason is due to energy release especially when the material has a damaged zone even before the maximum load is reached. In solid mechanics, when comparing the geometries of like structures of different sizes, the effect of characteristic structure length D and the nominal strength σ_N of the structure is known as:

$$\sigma_N = C_N \frac{F}{bD} \text{ or } \sigma_N = C_N \frac{F}{D^2} \tag{2.34}$$

where σ_N is the nominal strength, F is the applied force, b is the thickness of a two dimensional structure, D can be the diagonal dimension and C_N = arbitrary coefficient, which can be chosen to equal to 1. The coefficient C_N is depends on the structure geometry. For example, for a simply supported beam with three-point bending test the formula for the maximum normal stress is:

$$\sigma_N = \frac{3FS}{2bh^2} = C_N \frac{F}{bD}\,;\, C_N = 1.5\frac{S}{h} \tag{2.35}$$

where S is beam span, h is beam depth and D is the characteristic length. In this case, it is proper to say that C_N depends on the span to depth ratio; without geometric similarities the results of the equations would be totally different. Thus, it is important to consider the size effect for varying structures [1].

2.2.5 SPATIAL STATISTIC MEASURES

Quasi-brittle materials like concrete and other cementitious materials demonstrate a very high degree of statistical scatter in their microstructures. In this case, the nominal strength will be size dependent and the probability of failure of large scale structures is higher than that of small scale structures. Weibull incorporated the probability distribution into the fatigue failure of ceramics and introduced the power law for the statistical size effect [31]. His theory does not account for the material characteristic length. A number of approaches can be used to describe the microstructure component within the material. A Radial Distribution Function (RDF) is a suitable tool that can be used to define how particles are packed radially in a system (defining the insight material structure) [68]. This is not the case in flexible solids, since flexible solids have fixed particles position that do not overlap. The most suitable way to define this system is by defining how packed the system is or we say jammed or unjammed system. A jammed system is a mechanically stable system with minimum overlaps, but not in its lowest energy state. In a jammed system, there are two parameters can be used to determine how the system is jammed or unjammed, the translation and the bond orientation order. The translation parameter can be defined in the following equation [68]:

$$T = \left| \frac{\sum_{i=1}^{Ni} (n_i - n_i^{ideal})}{\sum_{i=1}^{N_c} (n_i^{FCC} - n_i^{ideal})} \right| \tag{2.36}$$

where: n_i is the average occupation number the spherical shell of width "t", N_C is the total number of shells, n_i^{ideal} is the shell occupation numbers for an ideal gas, FCC*:* face centered cube variant.

n_i^{FCC} :is the shell occupation numbers for an open FCC crystal lattice= either 4 or8. T is equal to zero for ideal gas and equals to one for perfect FCC spatial ordering. The orientation order equation is [68]:

$$Q_6 = \left(\frac{4\pi}{13} \sum_{m=-6}^{6} |\overline{Y_{6m}}|^2 \right)^{\frac{1}{2}} \tag{2.37}$$

where: $|\overline{Y_{6m}}|$: denotes an average over all bonds, Q_6 = 0, for a disordered system

2.2.6 RELATED EXISTING THEORIES

2.2.6.1 THE NON-LOCAL MODEL

Different but related theories reference a material's microstructure, based on considering a global statistic of the inclusions [68]. We need to capture the effect of every single inclusion on the fracture toughness through knowing the location of every single inclusion. Specially, in concrete and cementitious materials [5] and because of their spatial varying components and the distributed cracks, the non-local damage model is a suitable model to capture the damage due to the interaction from the adjacent micro-cracks that will lead to the material's failure. The other reason for considering non-local damage is that in concrete the macro- crack has non-negligible dimension and it is wider than the crack width. Certain parameters have to be determined such as the length parameter L or spatial parameter, which forms the constitutive models in driving the stress strain curve of the material [1]. As shown in Figure 2.17, the average strain along a representative volume centered at x will be considered for crack interaction.

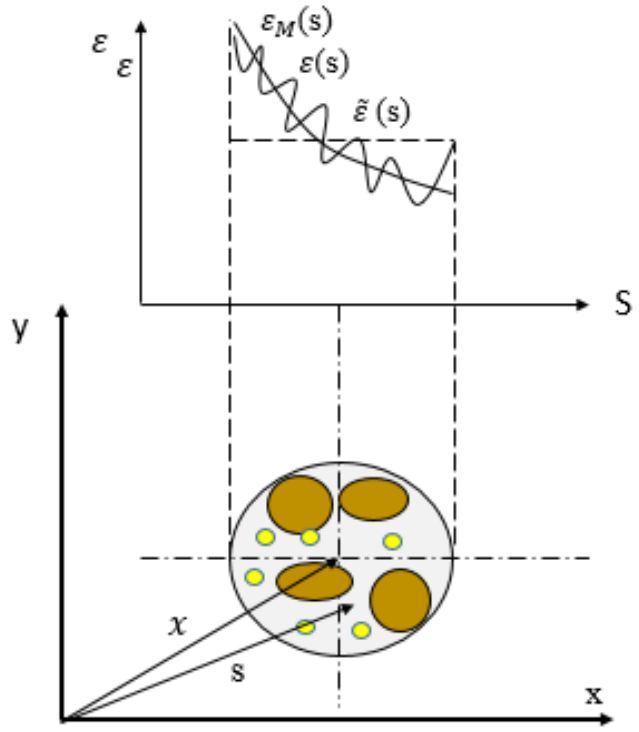

Figure 2.18. Diagrammatic illustrative of micro strain profile and average strain along a representative volume of a body [1]

2.2.6.2 THE STRONGEST BARRIER MODEL

As shown in Figure 2.18, in this model we are engaging a variety of different phases based on the nature of these heterogeneous materials, each with its own crack growth resistance having gradient colors. The material in front of the crack tip is divided into small cells with specific crack growth resistance *R* for each cell. The crack can grow and break the strong cell if the driving force φ is equal or greater than the crack growth resistance. The model relies on the probability of the crack being stopped by strong cells and their distributions. The limitation of this model is; it requires mode I type failure, to be combined with *R* curve, long material containing long crack and a

homogenous modulus. It does not account for the spatial arrangement of the microstructure in the material [1].

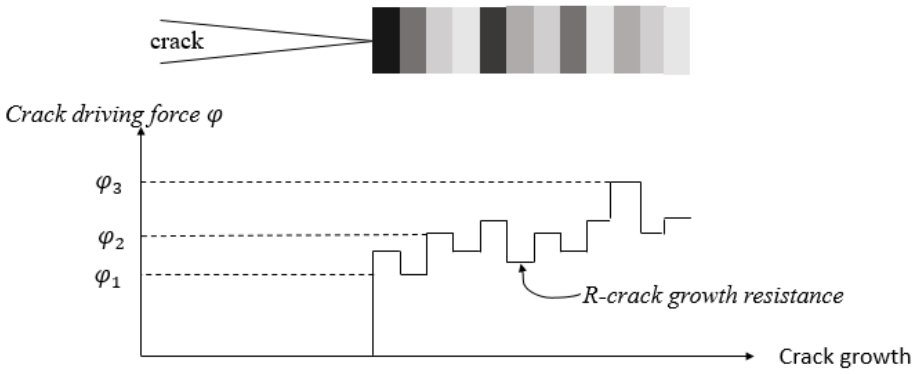

Figure 2.19. Random stepped R curve verses material's crack growth resistant φ [1]

Chapter 3 EXPERIMENTAL AND THEORETICAL INVESTIGATION OF THE FRACTURE BEHAVIOR OF GLASS BEADS/EPOXY COMPOSITIONS USING MICRO-SCRATCHING [1]

3.1 INTRODUCTION

To selectively study the impact of microstructure on fracture toughness, this chapter presents an experimental and theoretical investigation of the fracture toughness of a representative composite material consisting of glass beads embedded in epoxy using micro-scratching and conventional three-point bending tests. Existing analysis formulas for micro-scratch data assume homogeneity near the indenter tip. This chapter finds that this assumption may need to be reconsidered. By controlling the volume fraction of glass beads (inclusions) in the matrix of the composite material, it is possible to control the crack development and reduce the stress concentration within the material during loading [5]. Thus, an increase in the fracture toughness of the composites and improved fracture properties is obtained. As mentioned in the previous chapter, Akono *et al*. [5] used the scratch test to calculate the fracture toughness of a wide range of materials. Her work ignores the local effect of the inclusions on this stress field. In this paper we will consider this effect, which would allow us to further pursue the question: How can we improve the micro-scratch analysis methods? Is it possible to control the amount, or direction, of crack development by controlling the special distribution of the glass beads in the matrix?

---

[1]Adapted from Al wakeel, S. H., & Hubler, M. (2016). Experimental and theoretical investigation of the fracture behavior of glass beads/epoxy compositions using micro-scratching. Published in the 9th International Conference on Fracture Mechanics of Concrete and Concrete Structures University of California, Berkeley, CA.

3.2 EXPERIMENTAL WORK

3.2.1 RAW MATERIALS AND COMPOSITES PREPARATION

For all specimens, a hollow microsphere, 3M Scotchlite^{TM} glass beads (soda-lime) S38 microspheres have an average diameter of 40 μm, were used as the inclusions. The epoxy used as the binder consisted of the solid resin DGEBA (diglycidyl ether of bisphenol A) from Dow chemical Co. and the hardener DDS (4,4'-diaminodiphenylsulphone) from Sigma Aldrich Chemical Company. The physical properties of the epoxy "binder" and the glass bead "inclusions" are listed in Table 3.1.

Table 3.1. Physical properties of the epoxy and the glass beads

Material type	True density (g/cc)	Young's modulus (GPa)
DER 661/DDS	1.204	2.8
Glass beads S38	0.38	70

The fabrication of the composites was carried out using the following steps: (i) according to Ref. [12,22] the epoxy DER 661 was melted for an hour (ii) the glass beads were mixed with different volume percentages ranging from 0% to 50% at a time (iii) the mixture was combined with stoichiometric amounts of the curing agent DDS (98%) for thirty minutes (mix proportions are listed in Table 3.2) (iv) once uniform, the mixtures were cast in a pre-heated mold (v) finally, the specimens were placed in a convection oven for sixteen hours at 160°C when the temperature was increased to 200°C for two hours. Then the specimens were allowed to cool slowly in the oven to room temperature.

Table 3.2. Mix composition

Component	Composition
DER 661	100
DDS (98%)	12.2 ([1]phr)
Glass beads	0%, 5%, 25%, 50%

1Phr= Part per hundred of epoxide by weight

3.2.2 MICRO SCRATCH TEST

An Anton Paar micro-scratch tester with a capacity of 200N from was used to introduce a scratch in the specimen surface with a 200μm Rockwell diamond indenter as shown in Figure 3.1.

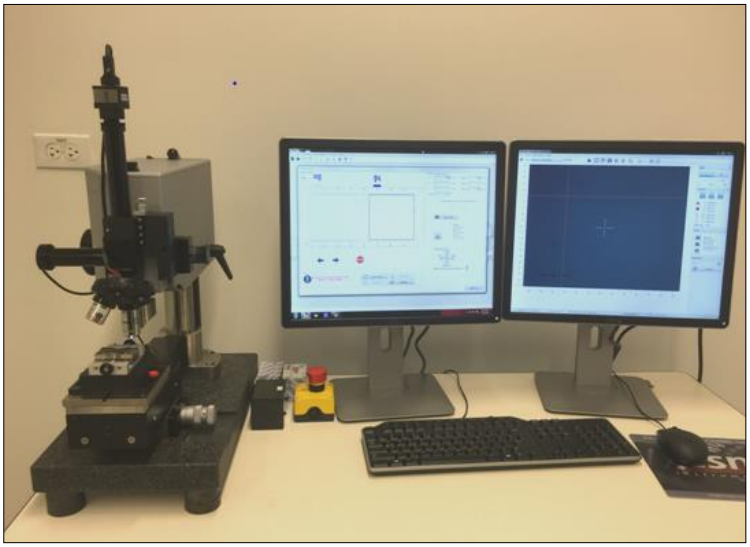

Figure 3.1. Scratch test equipment from Anton Paar

3.2.2.1 SPECIMEN SHAPE AND DIMENSIONS

In this study four small Aluminum molds with inner groove (20 x 40 x 10.59) mm^3 fabricated in Physics department's machine shop at University of Colorado-Boulder were used for the scratch test as shown in Figure 3.2. The specimen dimensions were selected carefully to fit in the scratching test equipment.

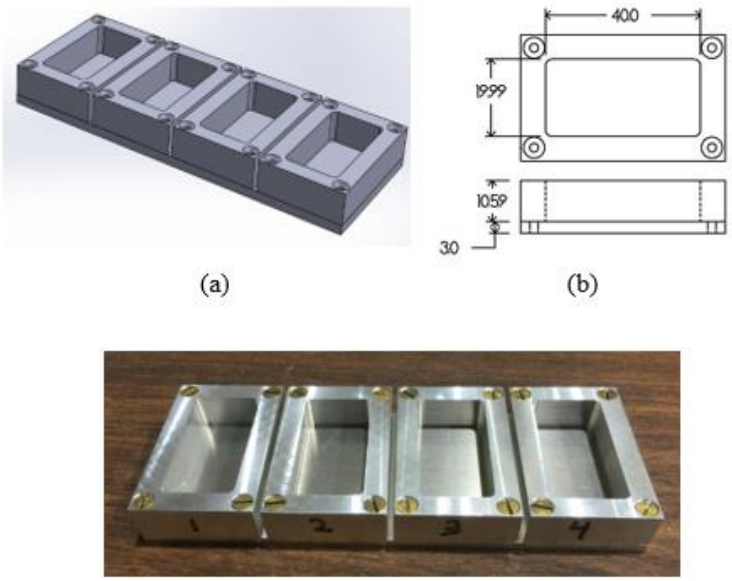

Figure 3.2. (a) Specimen's designed mold (b) Individual specimen's dimensions (in mm) (c) Final mold fabrication

Specimens with different glass beads created for the scratch test are shown in Figure 3.3.

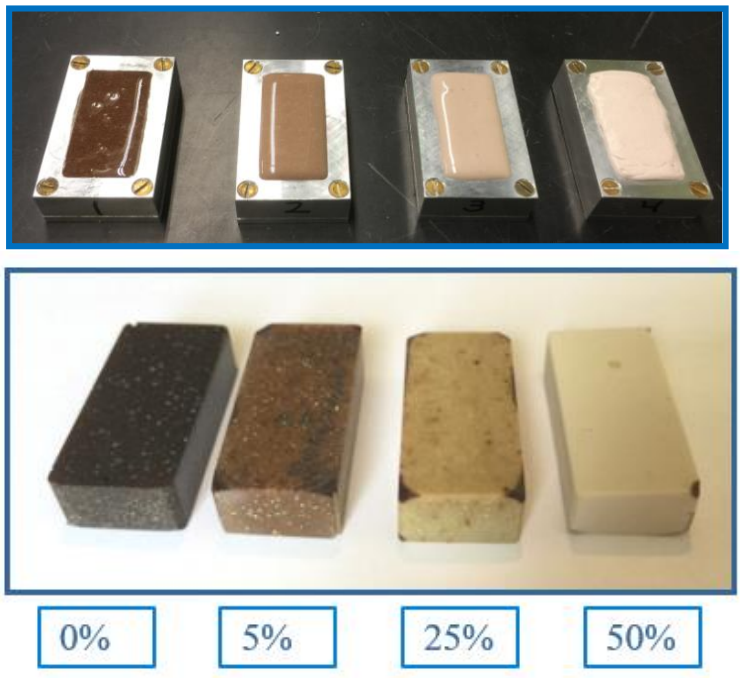

Figure 3.3. Specimens with different glass beads used in the scratch test

3.2.2.2 IMAGING AND SCANNING TECHNIQUE

Panoramic pictures of the surface were taken prior to performing any scratch as shown in Figure 3.4 to catalogue the inclusion and pore distribution. The scratch test was performed in three stages staring with a pre-scan phase in which the specimen surface was investigated by the indenter tip with a minimum load of 0.05 N.

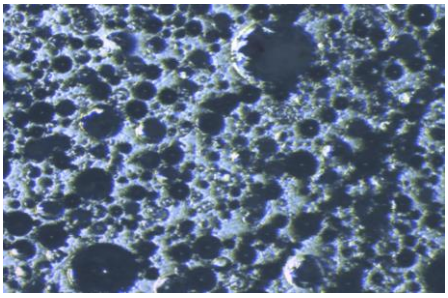

Figure 3.4. Typical SEM image of surface composites for 50% specimen. The different circular inclusions represent sections of the spherical glass beads which have been cut and polished down at different distance from their centers

During the second stage, a scratch is introduced on the specimen's surface. At the same time, the vertical and the horizontal forces as well as the penetration depth were recorded as the probe was pushed into the material until a depth d was reached. The scratch is produced by the projected horizontal load bearing contact area, not by the probe tip, as shown in Figure 3.5. The scratch testing parameters used in this test are listed in Table 3.3.

Table 3.3. Testing parameters used during the scratch test

Scratch test parameters	
Minimum vertical load (N)	0.05
Maximum vertical load (N)	0.5
Loading rate (N/min)	0.9
Speed (mm/min)	10
Scratch length (mm)	5

The scratch probe parameters used in this test are listed in Table 3.4.

Table 3.4. Scratch probe parameters

Indenter parameters	
Type	Rockwell
Material	Diamond
Radius (μm)	200

The last stage is the "panorama view phase". In order to image the physical crack, a series of panoramic pictures were taken across the whole scratch to image the physical cracks on the residual groove after the sample cracked, Figure 3.5 shows a sample of the panorama image.

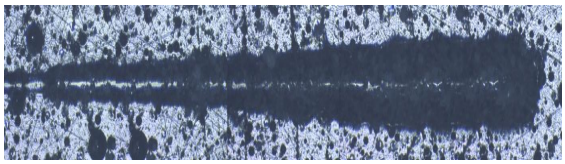

Figure 3.5. Panorama image of a scratch for 50% inclusion specimen

The fracture toughness in terms of (K_C), the stress intensity factor, was calculated according to the equation 2.25 developed by Akono et al [5]. The Panorama image of all the scratches are shown in Appendix A, section A.2.

3.2.3 SCANNING OF SPECIMEN SURFACE

Figure 3.6 represents the image segmentation by global thresholding using Otsu's algorithm [25]. Spatial statistics were used to check for the quality of the inclusion arrangement. The location of the inclusions is determined by implementing plot digitizer software. Data were collected as x and y coordinates associated with the inclusion locations from the images by placing the curser on the inclusions.

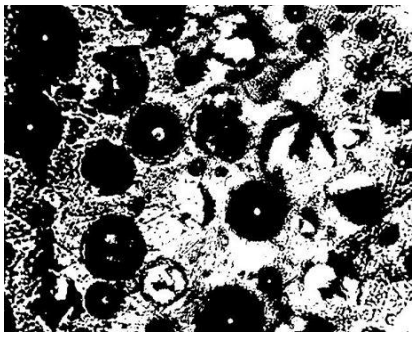

Figure 3.6. Segmented specimen's surface, converting the scanned surface pictures to black and white color using Otsu's algorithm for 50% glass beads

3.2.4 THE ASTM STANDARD THREE-POINT TEST

Three point bending tests on single-edge-notched specimens were conducted to determine the critical stress intensity factor K_C using standard methods for comparison. The specimen dimensions that were used in this study were the same as the specimen's dimensions used by Lee [12]. Per ASTM 399 section 91.4 [62], the width of the specimen $W = 2 * \text{thickness B}$. The thickness used in this study, B, was measured with a caliper on the specimen, an average value of 6.35 mm. Using the same method to measure the width W, an average value of 12.7 mm was found. A crack was created by inserting a razor blade into the specimen and measured to be equal to the thickness B [22]. The support span length S was measured to be equal to 50.8 mm. Figure 3.7 illustrates the specimen dimensions and notch shape.

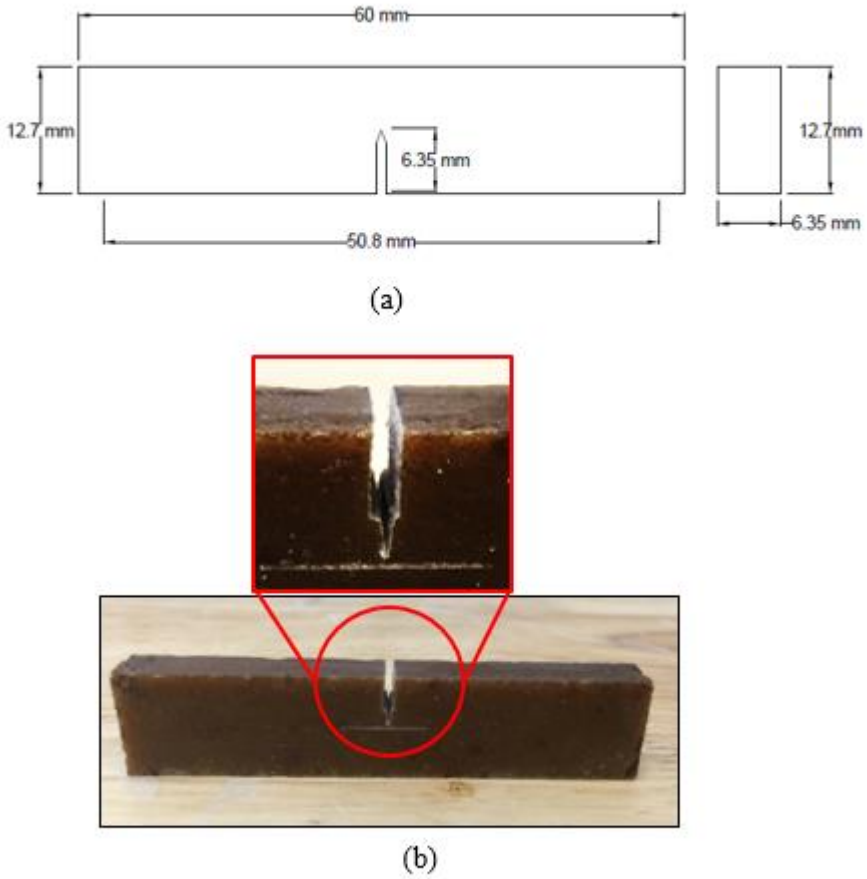

Figure 3.7. (a) Schematic representation of 3-pt specimen geometry used in this study; (b) 5% glass beads specimen

These dimensions were selected carefully to satisfy plane strain conditions:

$$B, a, (W - a) > \left(\frac{K_{IC}}{\sigma_y}\right)^2 \tag{3.1}$$

where B and a are measured with an average value of 6.35 mm, W is measured with an average value of 12.7 mm, K_{IC} is the fracture toughness obtained from the three-point bending test and σ_y is the calculated yield stress value from the tension test, 40, 40.1, 40.5 and 41 MPa for the polymer with 0%, 5%, 25% and 50% glass beads respectively.

3.2.5 THE ASTM STANDARD TENSILE TEST

A tensile test was carried out to determine the polymer tensile strength, which will be used to satisfy equation 3.1. The specimens were cast in a dog-bone shape mold as is illustrated in Figure 2.6 and were tested at room temperature using an Instron testing machine, shown in Figure 3.8. The Type I standard specimen's dimension was used per ASTM D638 [38]. The testing speed was 0.0416 mm/sec under displacement control mode using Instron machine.

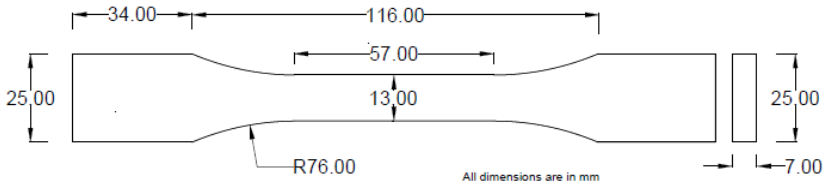

Figure 3.8. Specimen geometry for tensile test

Figure 3.9. Tensile test for 50% glass beads specimen loaded in Instron machine

After satisfying all the ASTM requirements, the three-point test was performed as illustrated in Figure 3.10. The load was applied by means of constant displacement at a cross head speed of 2.54 mm/min. The stress intensity factor was calculated using equation 2.32.

(a) *(b)*

Figure 3.10. Three-point test for 50% glass beads (a) before test; (b) after test

3.3 RESULTS AND DISCUSSION

Modeling and testing was performed on resin composites with four different volume fractures of microspheres ranging from 0%, 5%, 25% and 50% to study the influence of the microstructure inclusion content on the fracture parameters of the composite material. A comparison with the observed trend was then investigated using conventional three-point bending test on pre-cracked specimens.

3.3.1 FRACTURE TOUGHNESS USING MICRO SCRATCH

Figures 3.11-3.14 display the relation between the vertical force and the penetration depth for the four specimens considered in this task. Some scratch curves have kink points where they transition from a smooth parabolic curve to a noisy linear trend. In particular, those points occurred in the specimens that contained a 5% volume fraction of glass beads.

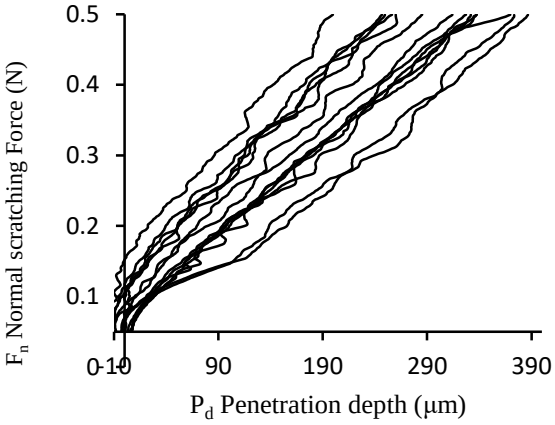

Figure 3.11. The relation between the normal scratching force and the penetration depth for 50% specimen

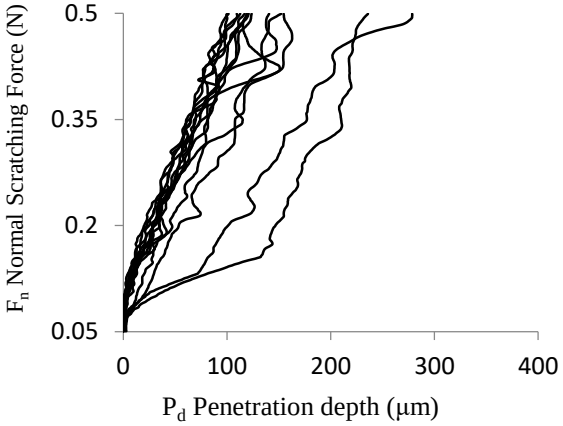

Figure 3.12. The relation between the normal scratching force and the penetration depth for 25% specimen

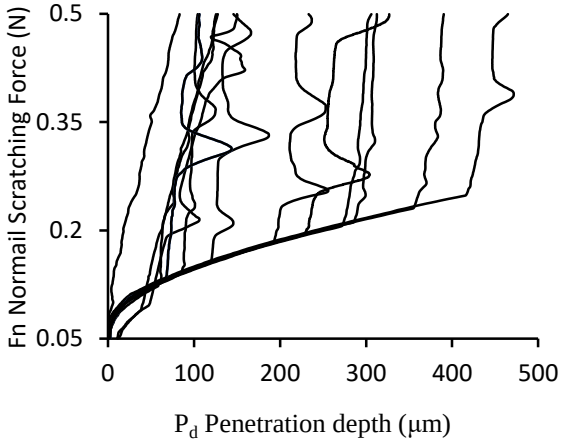

Figure 3.13. The relation between the normal scratching force and the penetration depth for 5% specimen

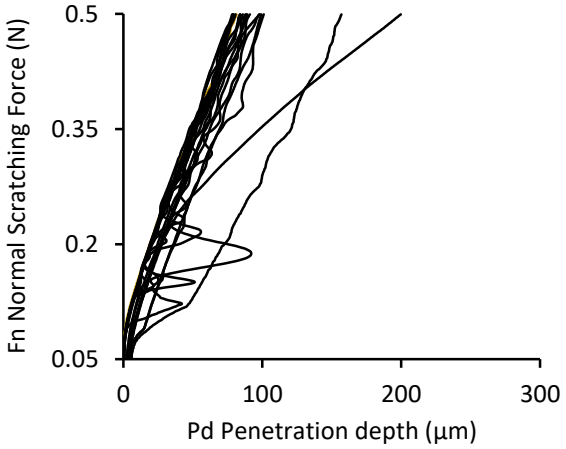

Figure 3.14. The relation between the normal scratching force and the penetration depth for 0% specimen.

Figure 3.15 shows the variation of the fracture toughness, as calculated using equation 2.21, for all the data the scratches with and without kink points, see Appendix A section A.1. Between 0% and 5% glass beads content, there is an increase in the fracture toughness value due to toughening mechanisms as the filler content increases. Beyond 5% glass bead content, the fracture toughness decreases due to microspheres de-bonding from the matrix. The de-bonding is accompanied by micro-cracks. If the directions of these cracks are parallel to the crack growth direction this would facilitate the crack propagation. Similar trends were found by Erwin *et al.* [22]. The most distinctive feature in Figure 3.15 is the significant decrease in the fracture toughness for inclusion content up to 50% compared to the neat epoxy resin. The reason behind that is the toughening mechanism is changing as the inclusion content is increased, which was explained by the particle spacing theory mentioned by Lee *et al.* [12] for glass beads embedded in epoxy resin composites. In this figure, we can notice that at 5% glass bead content the fracture toughness value is more scattered than for the other composites, greater variation in the arrangement of glass beads is possible at lower volume fractions.

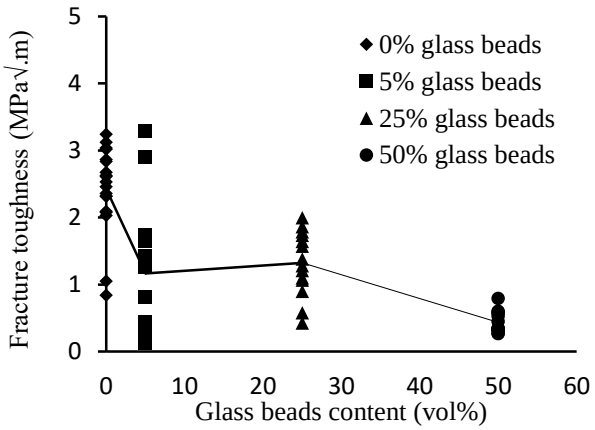

Figure 3.15. Fracture toughness range for different glass beads content using scratch test

3.3.2 FRACTURE TOUGHNESS FROM THREE-POINT TEST

A conventional three-point bending test with single edge notched geometry was also used to determine the material fracture toughness. The variation of the fracture toughness with the glass bead content for the three-point test is shown in Figure 3.16.

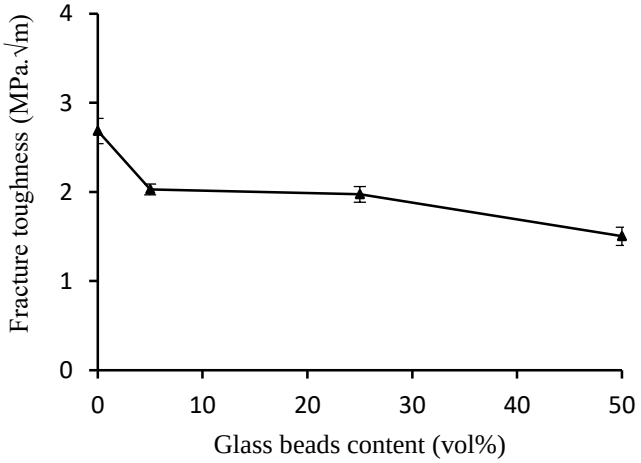

Figure 3.16. Fracture toughness range for different glass beads content using three-point test

A large discrepancy was found between the data sets shown in Figures 3.15 and 3.16. The curve has the same trend; however, the scratch values were systematically lower than the three-point test values. It was conjectured that this discrepancy could be from the effect of microstructural defects and system arrangement, which is detected by the micro-scratch test by pushing the probe along

of the specimen surface. However, it is also present in the zero inclusion case, so that it may just derive from the difference between the natures of the two tests. In the case of the three-point test, we load the material until failure and allow crack stresses to redistribute throughout the specimen, while in the micro-scratch test, we regulate the loading locally and do not allow the whole sample structure to assist in redistributing the applied load. As a result, local material crushing phenomena are much more prevalent in the scratch test than three-point bending tests and we do not allow the structure to act as a whole. In this chapter we will investigate the effect of the microstructure and leave the second hypotheses for future work.

3.3.3 INVESTIGATING THE MICROSTRUCTURE

The individual scratch test measurements for different inclusion contents were plotted in Figure 3.17. The increase in inclusion density as in curves (c) and (d) results in uniform and homogenous material behavior, with no kink or scatter in the plotted curves. There is a similar trend in the pure epoxy as indicated in curve (a). While a different trend can be noticed in (b), this implies that, in low concentrations of the inclusion, the behavior is changed because of the interaction with inclusions during the scratch test.

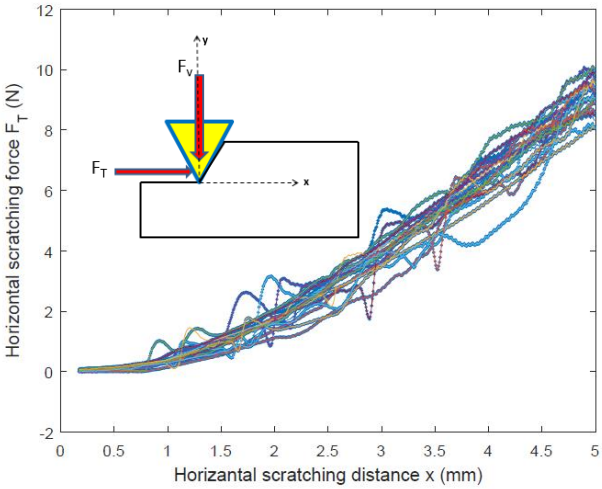

0% glass beads

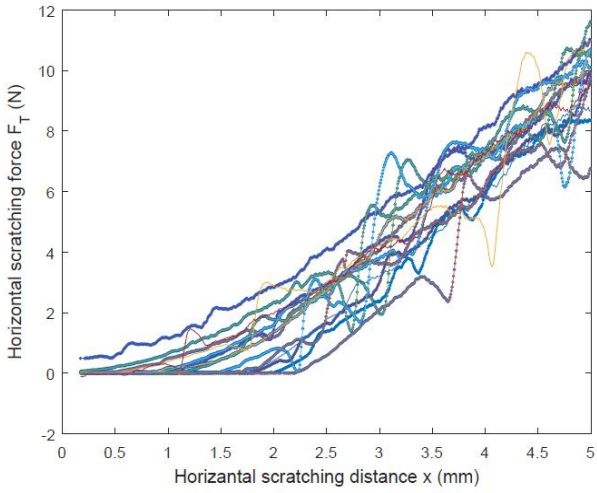

5% glass beads

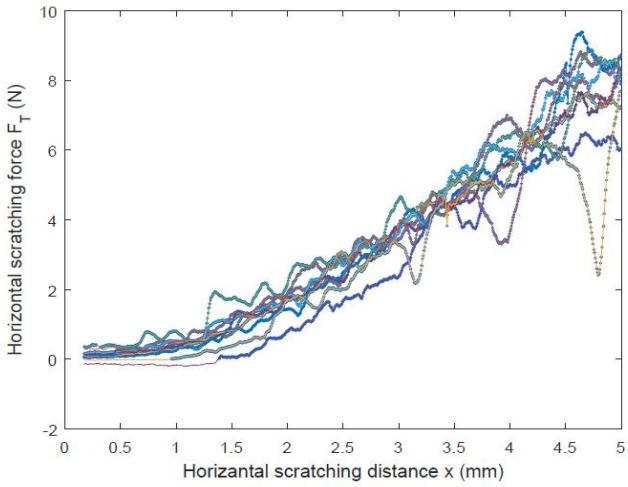

25% glass beads

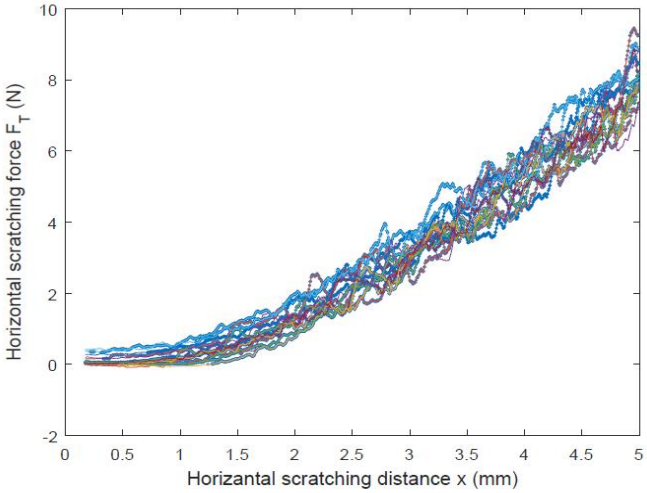

50% glass beads

Figure 3.17. Horizontal scratching force versus horizontal distance for different glass beads content using scratch test

By augmenting linear elastic fracture mechanics analysis of the scratch data, the fracture toughness for different compositions of the glass beads embedded in epoxy resin was derived. The fracture toughness, K_c for different compositions of the glass beads embedded in epoxy resin is presented in Figure 3.15. When considering the scatter in the results, no clear trend is observed. To test our hypothesis that the kink observed in some of the scratch data is due to the presence of the inclusions, we separated the data affected by the kink in Figure 3.15 to Figure 3.18 (a) and (b). After this separation, two clear trends are observed in the fracture response. Thus we propose that the kink is due to a change in boundary conditions when an inclusion is near the indentor tip. To confirm that such a change in boundary conditions could generate this effect, we will formulate a mathematical model considering this change and study the effect of probability of finding such an inclusion near the probe tip. See Appendix A, section A.3 for more details about the statistical analysis.

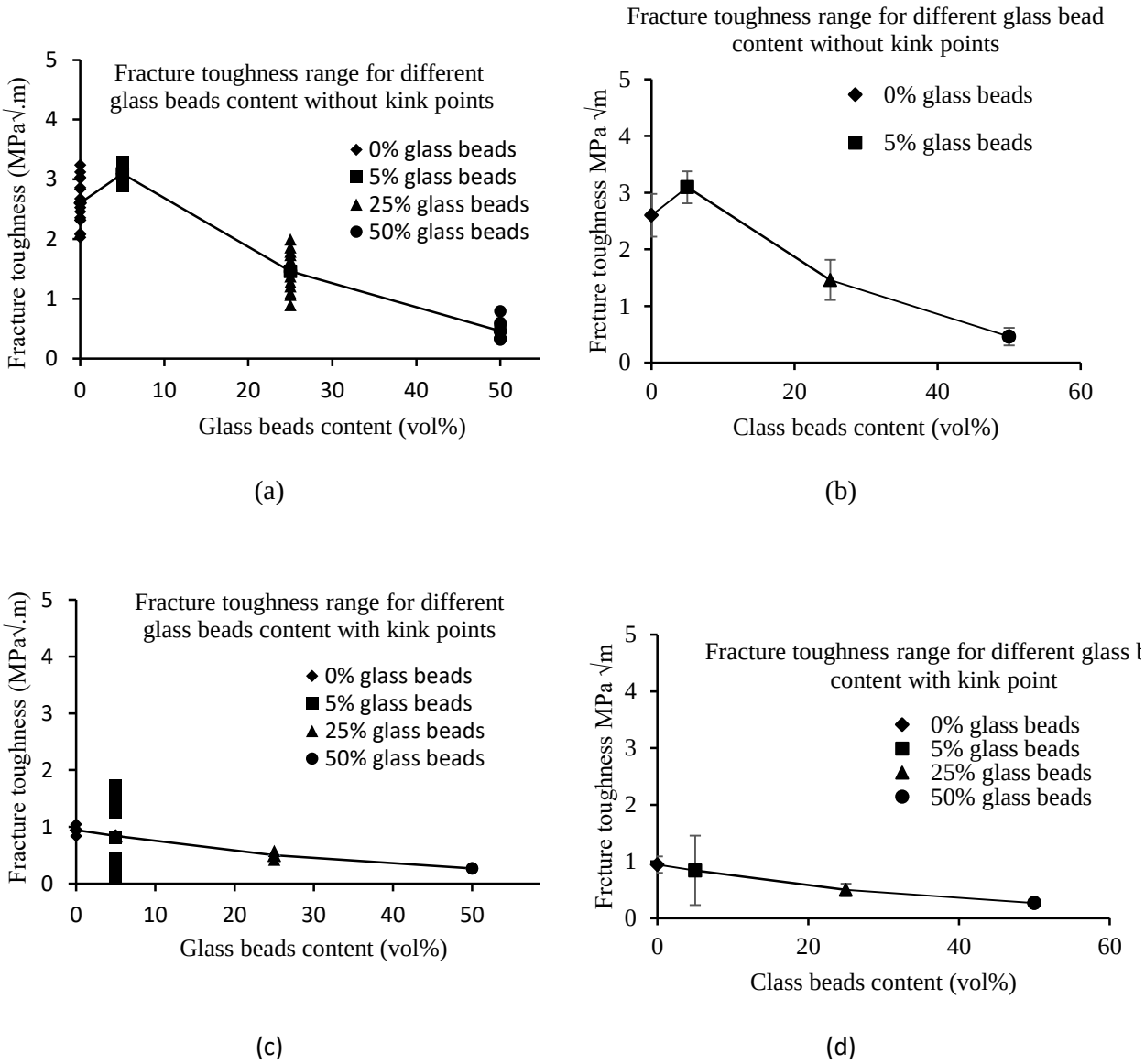

Figure 3.18. (a) On the left is the fracture toughness range for different glass beads content with kink points, on the right is the average data with the deviation in the data (b) On the left is the fracture toughness range for different glass beads content without kink points, on the right is the average data with the deviation in the data

3.3.4 EXPERIMENTAL AND NUMERICAL CONFIRMATION THAT KINK CURVES CAPTURE INCLUSIONS

As has been shown in Figure 3.18 (a), the shape of the fracture energy as a function of inclusion volume is due to a change in the microstructure of the material near the indenter tip. This only holds true for the curves showing a kink, which is hypothesized to relate the presence of an inclusion in front of the crack tip. In order to confirm the effect of microstructure on the material behavior, a numerical investigation is presented using finite element analysis of a centrally cracked composite material containing a single inclusion located near the crack tip. The fracture toughness is determined using the displacement extrapolation method, which uses nodal displacements near the crack tip. The analysis in this investigation is carried on the microstructure level; therefore, the fracture toughness is calculated based on the LEFM assumption and the concepts of plane strain conditions for mode I failure. The element used in this analysis is two dimensional with eight or six nodes having two degrees of freedom at each node. The deformed configuration of the specimen used in this simulation is shown in Figure 3.19.

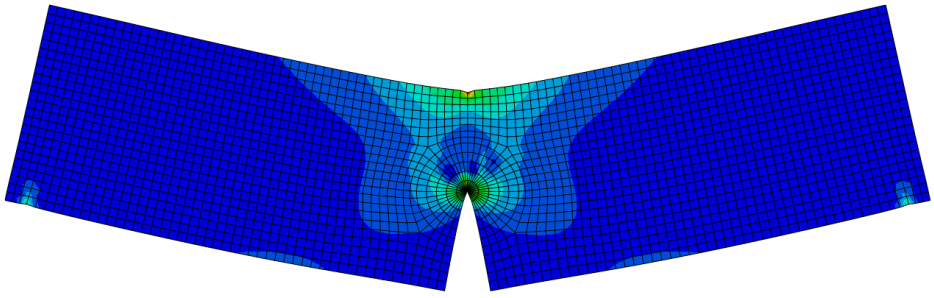

Figure 3.19. The deformed configuration of the specimen with inclusions located in front of the crack tip

3.3.5 MATHEMATICAL SIMULATION

We formulated the linear viscous behavior of glass beads embedded in epoxy resin composites during scratch testing. The standard linear solid (Zener model) [69] was used to interpret the experimental results and predict the behavior of the composite.

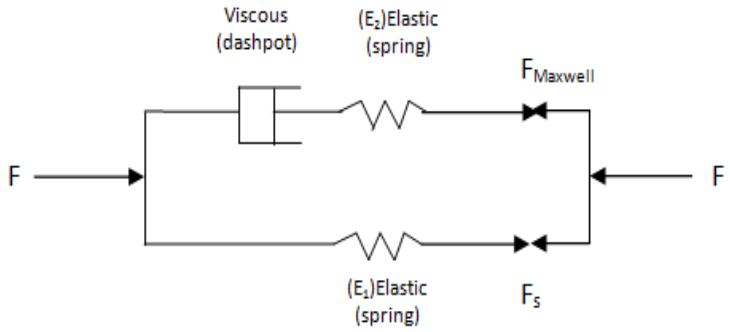

Figure 3.20: Standard linear solid (Zener model)

The following assumptions were made in modeling the behavior of the polymer: (a) The crack is a straight line and propagates along the x-axis, (b) two-dimensional representation of the model will be considered, (c) Cartesian coordinates will be used throughout the derivation.

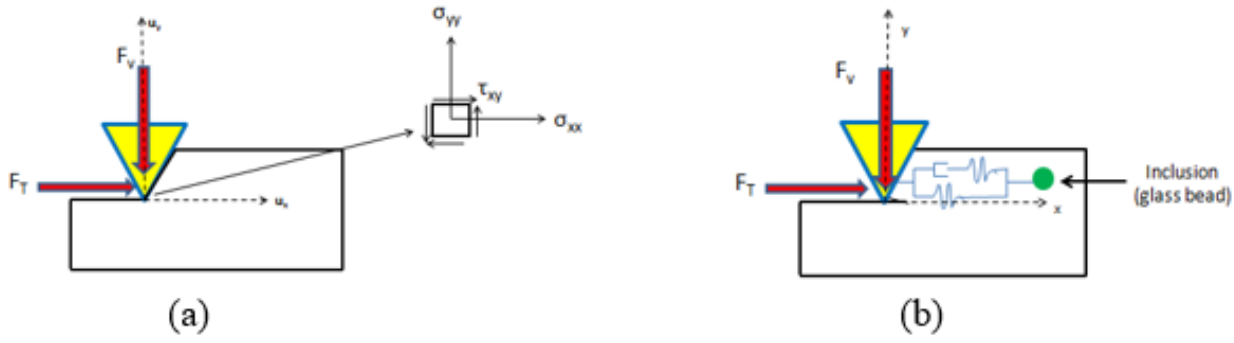

Figure 3.21. (a) Stress and displacement components in the Cartesian coordinate system (b) Using standard linear solid model to model the material behavior

A formulation of a visco-elastic stress strain constitutive relation was made of the material to mathematically simulate the behavior using the standard linear solid model illustrated in the Figure 3.21. The following constitutive equation has been used to relate the strain to the stress.

$$\varepsilon_t = \frac{\sigma_0}{(E_1+E_2)}\left[1 - e^{-\frac{(E_1+E_2)t}{\eta}}\right] \tag{3.2}$$

When the spring is connected to the dashpot in series, it yields a Maxwell model. A combination of the Maxwell model in parallel with a spring, as is illustrated in Figure 3.22, yields the model that we proposed to predict the shape of the compressive stress-strain curve [30]. If an inclusion is found far from the scratch probe the material is best represented with the spring moduli in the Zener model being identical, while very stiff and close inclusions will require unequal moduli. The observed transition point in the material response can be captured with this material model by changing the material stiffness to represent the various distances to the nearest inclusion as shown in Figure 3.22. Detailed derivation for equation 3.2 is provided in Appendix A, section A.4.

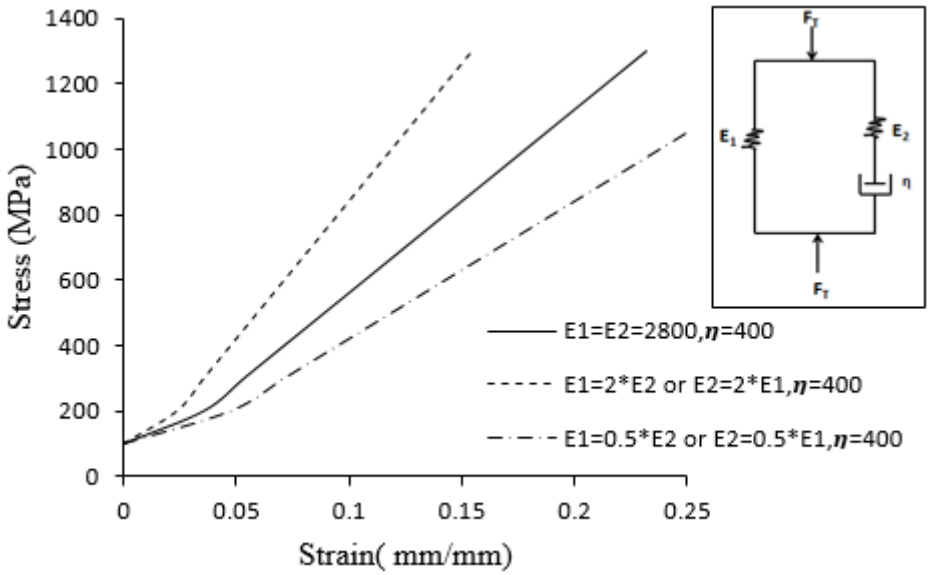

Figure 3.22. Compression stress-strain curve describes by the model on the right side of the figure

3.3.6 RANDOM PROBABILITY DISTRIBUTION

Random probability distributions were generated to test if the increase in noise is also due to the arrangement of the inclusions. Three different populations of random probability distribution of particles (pixels) were generated to calculate $g_{(r)}$ [68], the radial distribution function. This represents the probability of finding a nearby inclusion at any location in the sample. A random placement of inclusions was generated using MATLAB code to create sixty different fields of distributions of random pixels for each population. The populations were chosen to match the experimental test ranging from 5%, 25% and 50% volume fraction. Figure 3.23 illustrate the results of this analysis. The commented MATLAB code is shown in Appendix A, section A.5.

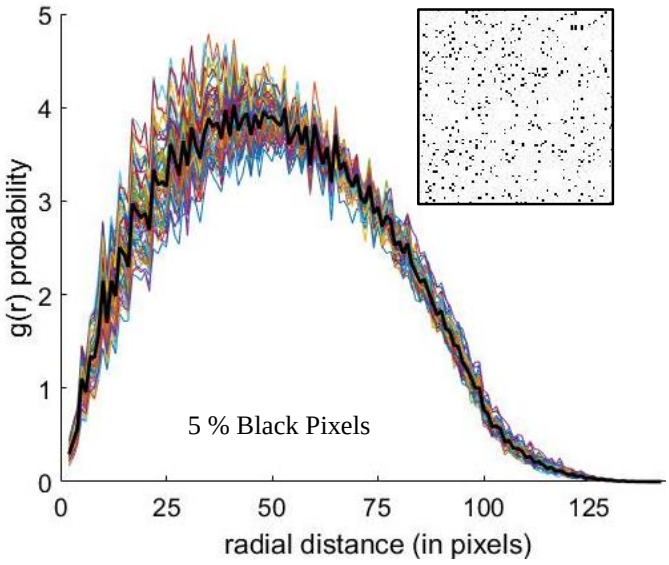

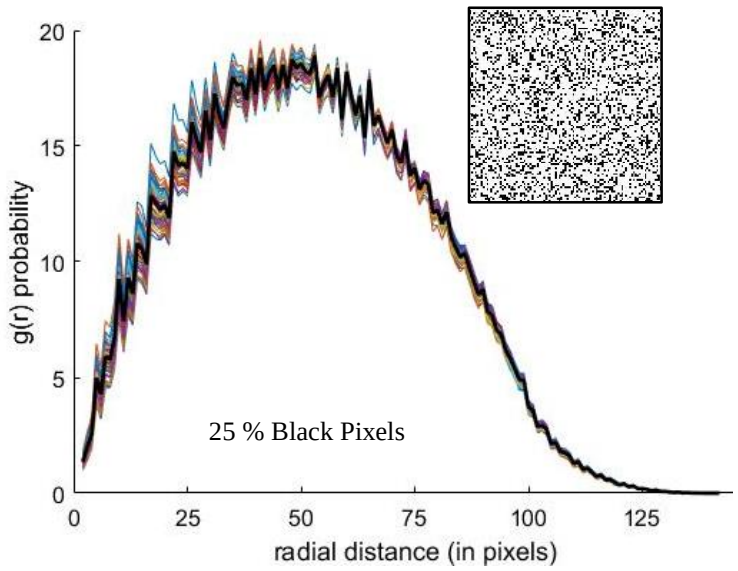

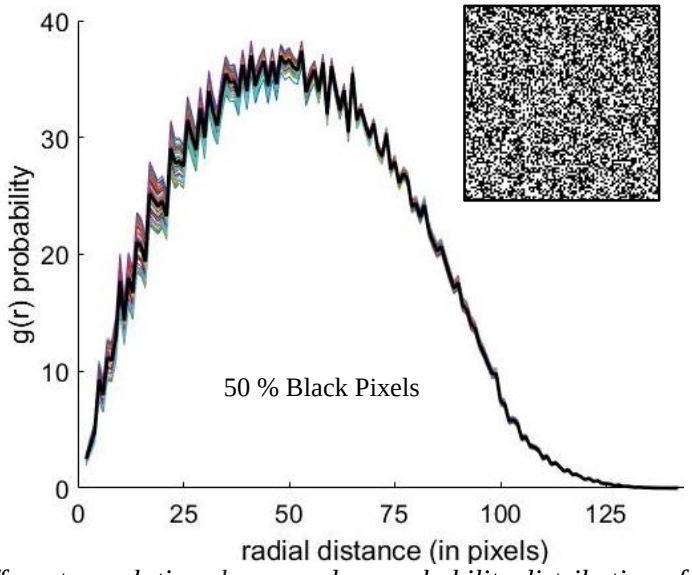

Figure 3.23. Three different populations have random probability distribution of particles (pixels) 5%, 25% and 50% particles content.

Numerical distributions were generated and confirm that 5% inclusions will cause the highest scatter due to the spatial arrangement of inclusions. The figures show the radial distribution functions for three different random arrangements of beads.

3.4 CONCLUSION

The microstructure near the indentor tip has a predictable and consistent impact on the fracture toughness, based on the following observations:

1. The fracture toughness changes in the experimental model system in which this is the only variable.

2. The 'kink' trend observed in the model system can be reproduced with a viscoelastic model that considers the effect of the nearest inclusion to the indentor probe

3. The trend in scatter with volume fraction of beads matches the probability of finding an inclusion near the indentor probe.

As a result, we propose a new formulation is required to obtain agreement between scratch and three-point fracture parameters by updating the *J*-integral formulation found in Akono *et al* [5].to capture the effect of local inclusions on the stress field generated by the indenter.

Chapter 4 FRACTURE TOUGHNESS DERIVED FROM THE MICRO-SCRATCH VERSUS 3-PT BENDING [2]

4.1 INTRODUCTION

To gain insight into the discrepancy of fracture toughness found in the previous chapter derived from micro-scale and macro-scale tests we studied the effect of explicitly considering inclusions within the material matrix. We find that by analytically formulating the effect of the inclusions on the fracture resistance of a crack within a particle composite reduces the discrepancy of fracture toughness derived from different tests, and matches the trend of fracture toughness values as a function of particle volume fraction. An explicit fracture mechanics representation of the fracture process zone is proposed to study the effect of inclusions and their effect on the energy release of the crack both in the near field and the far field from the crack tip. The derived formulations match the experimental behavior of polymers containing glass inclusions tested using two different experimental approaches: one based on the standard three-point test single edge notch and the other on the micro-scratch test. Existing crack growth design considerations of random composites rely on numerical models, which employ an inverse design process. The results of this work allow us to move towards a forward design method to design particulate composite microstructures for improved fracture resistance.

---

[2]Adapted from Al wakeel, S. H., & Hubler, M. (2017). Introducing heterogeneity into the micro-scratch test fracture toughness relation. Currently under review by the Journal of Experimental Mechanics.

4.2 EXISTING ANALYSIS OF MICROSTRUCTURE TEST

As mentioned previously in chapter two section 2.1.6, we considered two zones where the local arrangement of inclusions and stress shielding plays a role and not necessary be a Fracture Process Zone (FPZ) in front of the crack tip. In these zones, the crack is subjected to closure tractions, as first derived by Dugdale and Barenblatt [70, 71]. Both researchers extended LEFM and developed models by introducing a narrow zone of yielded material around crack tips. Wells observed that the crack faces shifted with plastic deformation—later leading to the development of the crack tip opening displacement concept [71]. Current fracture toughness formulations derived from micro-scale test data do not explicitly account for the material microstructure and its statistical distribution although it assumes that the fracture starts within a scalable FPZ under external loading [30]. The influence of the microstructure, such as inclusion distribution and inclusion content on the failure mechanisms within the composite material and its fracture toughness, will be investigated in this work. The development of a method for fracture analysis in multi-scale materials that specifically considers the microstructure is important to the understanding of how materials fail; and it is a main research direction in materials science research [20].

4.3 IMPACT OF INTERACTION OF CRACK-INCLUSION ON FRACTURE TOUGHNESS

For a material made of stiff inclusions embedded in a matrix, the existence of inclusions affects the deformations in the neighboring matrix material during loading and generates stress concentrations [30]. The stress field of a crack and inclusion interact and impact fracture toughness measures of the material. Remote inclusions dispersed within the matrix can also have an impact on the fracture toughness of the material in a homogenized sense. A study [50] was presented by several authors proposing that such an interaction yields stress shielding; reducing the stress intensity at the main crack tip. Their analysis considers the crack-inclusion problem using a global

energy balance. It was found that for small inclusion sizes, the crack growth requires more energy because the energy release rate decreases as the inclusion size decreases for the same applied load. Also, higher crack speeds were found for weakly bounded inclusions compared to the strongly bonded case [72-74]. Most of these studies discuss the influence of the existence of one inclusion ahead of the crack tip in a general sense, but not applied to a particular fracture toughness test.

The focus of this work is to develop a formula that considers the effect of the inclusions ahead of the crack tip in a scratch test and then compare the results with the ones that have been calculated from the standard three-point bend test to gain insight into the source of the difference between fracture toughness values measured on different scales. In particular, the fracture mechanics framework for micro-scale fracture toughness testing is updated to explicitly consider the effects of distributed cracks, voids, and inclusions. To selectively study the impact of microstructure, we introduce an inclusion in front of the crack tip to develop an analytical J-integral relation for a crack interacting with inclusions. Near-field and far-field interactions of the microstructure on the crack growth are accounted for separately. In the last part of this chapter, we show how the derived formulation captures the discrepancy between fracture toughness values derived from micro-scratch tests and classical three-point bending tests.

4.4 THEORETICAL DEVELOPMENT

4.4.1 J-INTEGRAL FORMULATION FOR MICRO-SCRATCH TEST

In 1968, Rice [37] began his development of the J-integral by considering notched two-dimensional homogenous linear and non-linear elastic bodies. Using Green's theorem, he proved that this definition of the J-integral is path independent (equal to zero) for any closed path Γ as defined below:

$$J = \int_{\Gamma} \left[W\, dy - T_i \frac{\partial u_i}{\partial x}\, ds \right] \tag{4.1}$$

where W is the strain energy density, T_i are components of traction on the surface of the interior body cut by Γ and ∂u_i are displacement components in the Cartesian coordinates x and y. Recently, Akono and Ulm [76] and Akono *et al.* [77], estimated the energy release rate for the scratch test geometry using the J-integral. With the resulting formulation, they presented a technique using a micro-scratch test carried out with a sharp blade pushed into the material surface under increasing load to estimate the energy release rate. This induces damage, including a horizontal crack which releases energy at the probe-material interface S:

$$G = \frac{1}{p} \int_{S} \left(\psi N_x - T_i \frac{\partial U_i}{\partial x} \right) DS \tag{4.2}$$

where $\boldsymbol{G}$ is the energy release rate, $\boldsymbol{p}$ is the perimeter of the probe projected onto the scratch direction, $\boldsymbol{S}$ is an integration path surrounding the crack tip, $\boldsymbol{\psi}$ is the free energy and $\boldsymbol{t_i}$ are the surface traction components. In Akono's work, the assumption that the energy release rate is equal to the $\boldsymbol{J}$-integral value leads to calculate the fracture toughness though equation 2.12 [5]. Throughout Akono's work, the fracture toughness formula was derived assuming material homogeneity ahead of the probe during the scratch test by directly applying Rice's formula. Additionally, it was assumed that the generated crack only propagates in the plane of the direction of motion. For the application of the $\boldsymbol{J}$-integral that we are proposing, the existence of one or more inclusions ahead or around the crack tip is considered. Their presence will influence the potential energy during the fracture process since a different amount of energy is dissipated. The $\boldsymbol{J}$-integral of a cracked material with an inclusion has been investigated by some researchers [48, 73- 75]. The objective of this work is to calculate the stress intensity factor using a closed path surrounding

the crack tip with embedded inclusions. To selectively study the impact of microstructure on the micro-scale fracture parameter, our investigation considers the impact of the distribution of inclusions and voids in the matrix of the composite material.

Let us consider a cracked specimen with an arbitrarily located inclusion as shown in Figure 4.1. A closed path counter is drawn clockwise from the lower crack face to the upper crack face which does not enclose the crack tip singularity in the local field. Only mode I loading will be considered here.

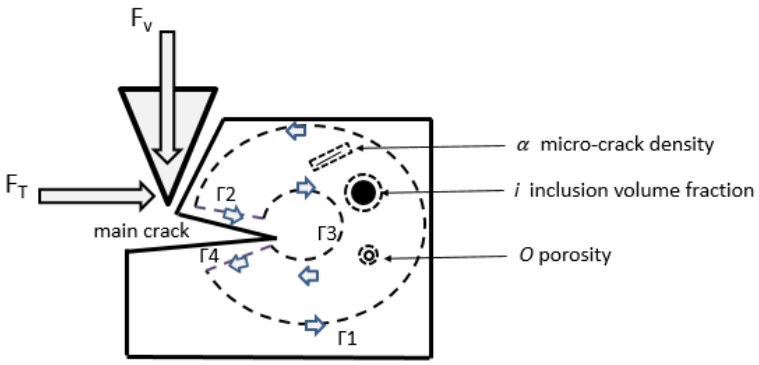

Figure 4.1. Path definition for a cracked specimen with arbitrary an arbitrary located inclusion.

The size and density of the inclusions in the material are such that at some point in the scratch process the path must be drawn with the arbitrary inclusion inside the contour integral. We can apply Rice's formula to the bounded region in Figure 4.1, whose boundary consists of Γ_1, Γ_2, Γ_3, Γ_4 and Ω,where Ω is the boundary of the inclusion. It is assumed that we can find a closed path that excludes the singularity and never goes through the inclusion, then the total contour integral is equal to:

$$\int_{\text{total}}[\quad] = \int_{\Gamma_1}[\quad] + \int_{\Gamma_2}[\quad] - \int_{\Gamma_3}[\quad] + \int_{\Gamma_4}[\quad] + \int_{\Omega}[\quad] = 0 \tag{4.3}$$

where $[\quad] = W\,dy - T_i \frac{\partial u_i}{\partial x}\,ds$ (4.4)

The contribution of the two parts $\boldsymbol{\Gamma_2}$ and $\boldsymbol{\Gamma_4}$ to the $\boldsymbol{J}$-iintegral is zero since the crack faces are stress free: $\boldsymbol{T = 0}$ and $\boldsymbol{dy = 0}$. Contour $\boldsymbol{\Gamma_1}$ is eliminated since the specimen surface is assumed to be stress free. In other words, the remaining parts are:

$\int_{\text{total}}[\quad] = \int_{\Gamma_3}[\quad] - \int_{\Omega}[\quad]$, thus (4.5)

$\boldsymbol{J = J_{\Gamma_3} - J_{\Omega}}$ with one inclusion (4.6)

$J = J_{\Gamma_3} - \sum_{K=1}^{\infty} J_{\Omega_K}$ Considering multiple inclusions (4.7)

Since the traction components are equal to zero near the specimen and crack surfaces (stress free) the only remaining term in Equation 2.8 is the strain energy density term $\boldsymbol{W}$. Based on Equation 4.7, it becomes clear that the presence of inclusions will cause a change in the $\boldsymbol{J}$ -integral value. We evaluate this change explicitly for pores, distributed cracks, and inclusions in the near and far field next.

4.4.2 FAR FIELD INTERACTION

To evaluate the far field stress, we use the expression for the change in the potential energy proposed by Karchanov *et* al [72]. By doing so we can link the *J*-integral and the potential energy in the matrix. Our analysis accounts for the change in the potential energy due to the existence of inclusions, which is represented by:

$$\frac{1}{2}\,\sigma : \varepsilon(\sigma) = \frac{1}{2}\,\sigma : M^{\circ} : \sigma + \frac{1}{2}\,\sigma : H : \sigma = f_0 + \Delta f \quad (4.8)$$

where f_0 is the potential of the matrix; Δf the change in the potential due to the introduction of the inclusion, σ is the applied stress; a colon denotes contraction over two indices; ε the strain due to inclusion volume M° is the compliance tensor of the matrix; and H is the inclusion compliance tensor [72]. For an isotropic elastic material, the potential energy of the matrix without inclusions is appropriately presented as,

$$f_0 = \frac{1 + v_o}{2E_0}\sigma_{ij}\sigma_{ji} - \frac{v_0}{2E_0}(\sigma_{kk})^2 \tag{4.9}$$

where, E_0 is the composite modulus of elasticity calculated using the slope of linear portion of the stress-strain curve, the average modulus epoxy/glass beads was found to be 1850 MPa from detailed calculations is in Appendix B, section B.1 For plane strain requirements, E_0 is replaced by $(E/(1-v^2))$, v_0 is Poisson's ratio equals to 0.25 [78] and it is replaced by $(v/(1-v^2))$, σ_{ij} is the component of Cauchy stress tensor and $\sigma_{kk}$is the sum of the stresses on the main diagonal of the stress tensor. The induced damage will propagate in the direction of $x = +\infty$, $dy = 0$ so that the only component of the Cauchy stress that will be considered is σ_{xx}. The stress field equation in the neighborhood of a crack tip for opening in mode I in an isotropic linear, elastic material:

$$\sigma_{xx} = \frac{K_I}{\sqrt{2\pi r}}\cos\left(\frac{\theta}{2}\right)\left(1 - \sin\left(\frac{\theta}{2}\right)\sin\left(\frac{3\theta}{2}\right)\right) + \sigma_{0x} \tag{4.10}$$

where, (r, θ) is any location where the stress is to be calculated, σ_{ox} is a term corresponding to a uniform stress parallel to the crack [31]. This term will not be included in the analysis as Irwin showed that this stress has no influence on the stress intensity factor and contributes nothing to the crack opening stress, although it may slightly effect the size of any plastic zone [31].

In terms of the elastic potential, the representation of the potential energy for the microstructure of a cracked solid material containing inclusions, pores and micro-cracks is given by:

$$f = f_{0_{Matrix}} + \Delta f_{Inclusion} + \Delta f_{Pore} + \Delta f_{Microcrack} \tag{4.11}$$

The total potential energy will be the sum of all interacting microstructure components [45]. The elastic potential contribution from the matrix is given by equation 4.10. For a mixture of interacting inclusions, the change in the matrix potential is:

$$\Delta f_{inclusion} = \frac{1}{(1-i)} \frac{1-v^2}{2E_0} \left[i[4tr\sigma . \sigma - (tr\sigma)^2] \right] \tag{4.12}$$

where, i is the inclusion volume fractions, values of 0%, 5%, 25% and 50% were used to match the experimental work. The change in potential due to pores is:

$$\Delta \boldsymbol{f_{pore}} = \frac{\mathbf{1}}{(\mathbf{1}-\boldsymbol{o})} \frac{\mathbf{1}}{\mathbf{2}\boldsymbol{E_0}} \left[\boldsymbol{O}\left[\mathbf{4}\boldsymbol{tr\sigma} . \boldsymbol{\sigma} - (\boldsymbol{tr\sigma})^{\mathbf{2}} \right] \right] \tag{4.13}$$

where O is the porosity by volume, this value was calculated theoretically following the ASTM D2734 [79], it was found to be 0.05, 0.05, 0.04 and 0.03 for 0%, 5%, 25% and 50% respectively, detailed calculation is in Appendix B, section B.2. The change in potential due to micro-cracks is:

$$\Delta f_{micro-crack} = \frac{8(1-v^2)}{3E_0} \frac{1-\frac{v_0}{4}}{1-\frac{v_0}{2}} \sigma . \sigma : \alpha \tag{4.14}$$

where α is the crack density. The polymer crack density used in this work is equal to 0.15, based on using the same loading condition as in [72]. Crack density can be calculated using the following equation [80-84], after initiating damage using uniaxial tension specimen. The cracks were observed under an optical microscope, then the average number of microcracks were counted per unit volume.

$$\alpha = N \frac{\bar{v}}{\eta} \tag{4.15}$$

where, N is the number of the cracks per unit volume, η is the crack aspect ratio, $\eta = \frac{a_1}{a}$, a_1 is the crack length a is the half axes of penny-shaped crack.

Substituting equations 4.9 and 4.12-4.14 into equation 4.1 leads to a new formula for a matrix with interacting inclusions, pores and micro-cracks in the following expression of the *J*-integral:

$$J = f_0 = \frac{1+v_o}{2E_0}\sigma_{ij}\sigma_{ji} - \frac{v_0}{2E_0}(\sigma_{kk})^2 +$$
$$\frac{1}{(1-i)}\frac{1-v^2}{2E_0}\left[i[4tr\sigma.\sigma - (tr\sigma)^2]\right] +$$
$$\frac{\mathbf{1}}{\mathbf{(1-o)}}\frac{\mathbf{1}}{\mathbf{2E_0}}\left[O[4tr\sigma.\sigma - (tr\sigma)^2]\right] +$$
$$\frac{8(1-v^2)}{3E_0}\frac{1-\frac{v_0}{4}}{1-\frac{v_0}{2}}\sigma.\sigma:\alpha \qquad (4.15)$$

where i represents different volume fractions of inclusions, O is the porosity by volume, and α is the crack density.

4.4.3 NEAR FIELD INTERACTION

Many researchers have presented a complex form of the Airy stress function to solve near crack tip problems, including Westergaard 1939 [34], Rice 1969 [36], Muskhelishvili 1953 [85], Paris and Sih 1965 [86], Goodier 1969 [87], and Eftis and Liebowitz 1972 [88]. To formulate the near field stress field of the evolving crack tip for the scratch problem, we use the Westergaard stress function for its ability to solve a wide range of crack problems analytically. In general, any choice of the stress function must satisfy the following biharmonic equation [34]:

$$\frac{\partial^4\Phi}{\partial^4 x} + 2\frac{\partial^4\Phi}{\partial^2 x\partial^2 y} + \frac{\partial^4\Phi}{\partial^4 y} = 0 \qquad (4.16)$$

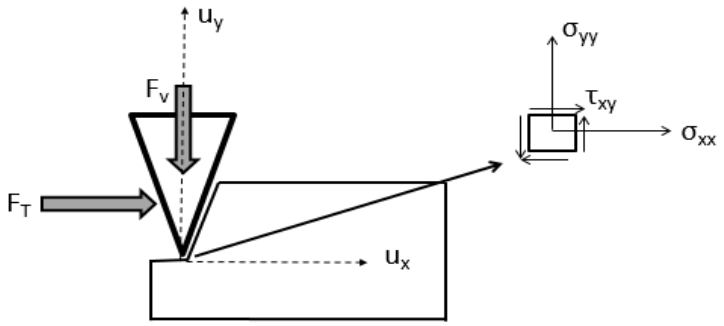

Figure 4.2. Definition of the coordinate axis in front of a crack tip with stress and displacement components in the Cartesian coordinate system.

In this derivation, two-dimensional geometry is assumed. Cartesian coordinates are used and the crack is assumed to be a horizontal line deriving from the crack tip that propagates along the x-axis throughout the scratch test. Figure 4.2 shows the displacement in the x and y directions, respectively. The corresponding stress components are σ_{xx}, σ_{yy}, σ_{xy}. These stress components must satisfy the governing compatibility equation

$$\mathrm{Z_{(z)}} = \sum_{\mathrm{j=0}}^{\infty} \mathrm{A_j\, z^{j-\frac{1}{2}}} \tag{4.17}$$

The Westergaard stress function $Z_{(z)}$ [34] has been employed for a cracked material, assuming that the shear stress σ_{xz} is equal to zero. For the leading terms $j = 0$ and ($Z = re^{i\theta}$) where $e^{i\theta} = \cos\theta - i\sin\theta$, we get the following set of equations:

$$\sigma = \sigma_{xx} = Re(Z_{(z)}) = A_0 r^{-\frac{1}{2}}\left[cos(-\frac{1}{2})\beta - (-\frac{1}{2})\, sin\,\beta\, sin(-\frac{3}{2})\beta\right]$$

$$= A_0 r^{-\frac{1}{2}}\left[cos(\frac{\beta}{2}) - (\frac{1}{2})\, sin\,\beta\, sin(\frac{3\beta}{2})\right] \tag{4.18}$$

The coefficient A_0 can be calculated after performing the tension test to determine the stresses in x and y directions by using the equation below:

$$A_0 = \frac{\sigma_{xx}\ (r^{0.5}\ )}{(cos\ \beta - \frac{1}{2} sin\ \beta\ sin\frac{3\beta}{2})} \tag{4.19}$$

The location of the inclusion is defined by the angle β with respect to the crack tip [49] as shown in the Figure 4.3.

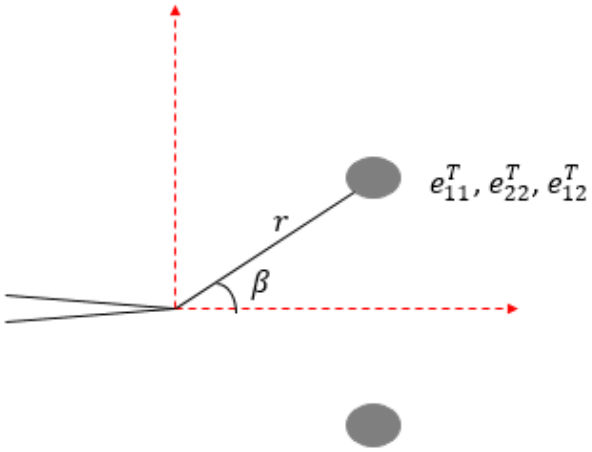

Figure 4.3. Two inclusions symmetrically located in front of the crack tip with respect to the crack plane

Since we are dealing with material microstructure, in which the probability of an inclusion or void existing above or below the crack tip is equal, we can assume on average that $\beta = 0$. A small value for r specifies that the inclusion must be within the near-field stress region of the crack tip, thus,

$$\boldsymbol{\sigma = \sigma_{xx} = \sigma_{yy} = A_0 r^{-1/2}} \qquad \text{for } \boldsymbol{y = 0} \text{ and } \boldsymbol{\beta = 0} \tag{4.20}$$

To investigate the effect of inclusions near the crack tip on the fracture toughness we define a near-field volume in front of the crack tip and investigate the effect of the inclusion in this volume on

the material fracture toughness. We assume that the Local Spherical Representation Volume (LSRV) is a symmetrical spherical domain of finite size located in front of the crack tip. A cut-off stress may be chosen to scale as a function of the microstructural feature size to capture the extent of the stress field interactions between the crack tip and feature.

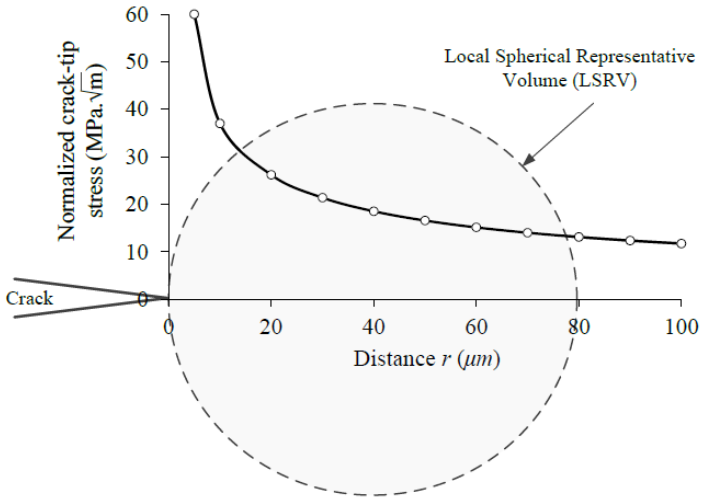

Figure 4.4. The normalized crack-tip stress as a function of the distance r in front of the crack tip and the LSRV. The LSRV is located at the head of the crack tip

Using equation 4.20, the way the normalized crack-tip stress decays along $y = 0$ is illustrated in Figure 4.4. The volume of the LSRV is calculated using the standard formula for a sphere. Then the number of inclusions per unit volume can be determined by incorporating the volume fraction of inclusions in the LSRV region. The radius of the near-field region is chosen to be double the inclusion size to allow for some stress shielding. The near field crack inclusion interaction is considered within this volume. Throughout this analysis, the shape of the inclusion is assumed to be a spherical and arbitrarily distributed in this volume. Perfect bonding is assumed between the matrix and the inclusion, although an imperfect bond may be introduced. As presented by Li. *et*

al. [49], it is possible to calculate the change in stress intensity where the inclusion is symmetrically placed with respect to the crack plane by:

$$\Delta K_{tip} = \frac{1}{2\sqrt{2\pi}} \frac{E_0}{1-\nu^2} r^{-3/2} \Omega\left(e^T_{\alpha,\gamma}, \beta\right) dA \tag{4.21}$$

where

$$\Omega\left(e^T_{\alpha,\gamma}, \beta\right) = (e^T_{11} + e^T_{22}) \cos\frac{3\beta}{2} + 3e^T_{12} \cos\frac{5\beta}{2} \sin\beta + \frac{3}{2}(e^T_{22} - e^T_{11}) \sin\beta \sin\frac{5\beta}{2} \tag{4.22}$$

The terms e^T_{11}, e^T_{22} and e^T_{12} represent unconstrained strains in the area located at (r, β) as it is shown in Figure 4.3, their values were calculated using equation 4.22. The fracture toughness at the crack tip can then be calculated using the following expression [49]:

$$K_{tip} = K_0 + \Delta K_{tip} \tag{4.23}$$

where K_0 represents the stress intensity for the matrix without inclusions as given by standard 3-pt bending equations and ΔK_{tip} represents the variation of the stress intensity induced by the inclusion located within crack tip field as given by equation 4.21. An upper and lower limit of this equation can be calculated within the range of admissible β angles, which represent possible inclusion configurations in the near field.

4.5 STRESS INTENSITY FACTOR BASED ON FRACTURE TESTING

To elucidate the formulas from previous section, we performed two different types of fracture toughness tests at different scales: the standard three-point bending and the micro-scratch tests on resin composites with four different volume fractures of microspheres ranging from 0%, 5%, 25% and 50%. These tests were described in Chapter 3 and their results will be utilized here.

4.5.1 COMPARISON WITH THEORETICAL FORMULATION

The number of inclusions for each volume fraction of the mix (Table 4.1) was calculated based on, the percent of inclusion content, LSRV volume (1,206,372 μm3) and the inclusion volume (150796 μm3).

Table 4.1 Number of inclusions based on percent content of inclusion, volume of inclusion and the LSRV volume

Inclusion content (vol.%)	*Number of inclusion (inclusion)*
0%	*0*
5%	*1*
25%	*2*
50%	4

The strain values for equation 4.22 were calculated using the stress-strain relation for plane strain, equation 4.23, for each volume fraction of inclusions tested.

$$\begin{Bmatrix}\varepsilon_{11}\\ \varepsilon_{22}\\ \varepsilon_{12}\end{Bmatrix} = \frac{1+v}{E}\begin{bmatrix}(1-v) & -v & 0\\ -v & (1-v) & 0\\ 0 & 0 & 1\end{bmatrix}\begin{Bmatrix}\sigma_{11}\\ \sigma_{22}\\ \sigma_{12}\end{Bmatrix} \tag{4.24}$$

For calculating ΔK_{tip} using equations 4.21, it was reported by Li. *et al.* [49]that the value of β should be less than $\pi/3$. They investigated the crack-inclusion interaction of two circular inclusions symmetrically located with respect to the crack tip. If the spots were located within a 120° fan in front of the tip (i.e. $\beta < \pi/3$) increases were observed in the stress intensity at the crack tip, while any location beyond this fan reduced the intensity. As the interest of this work is to investigate the near-tip intensity due to the interaction of crack-and-inclusion on the fracture toughness of the material, the β value used in this analysis was less than $\pi/3$. Three different values for β angles were used: 0, $\pi/4$ and $\pi/6$, to probe the solution space. The term Ω in equation 27 was calculated using the β values mentioned above and the strain values from equation 30. The porosity was calculated to be 0.5% and the crack density as 0.15 based on data presented in [72].

Different scenarios are presented in Figure 4.5 in which we investigate the interaction of a crack and inclusions in a random system on the near tip intensity stress. ΔK_{tip} was calculated based on

the probability of finding individual, two, and four inclusions within the selected β range. For the individual inclusion case half the ΔK_{tip} value was used, since the ΔK_{tip} equation considers two spots symmetrically located with respect to the crack tip. In the case of four inclusions the ΔK_{tip} were multiplied by 2. The plot in Figure 4.5 (a, b, c and d) illustrates the ΔK_{tip} decay for one, two and four inclusions located within the LSRV region for 0%, 5%, 25% and 50%, volume fraction of inclusions. The x-axis represents the distance in front of the crack tip. The amount of energy released during the fracture process was determined by integrating the area under the curves. Then by dividing the area by r, we could calculate the fracture toughness. In Figure 4.5, the light gray represents a region between upper and lower bounds for the angle β , the case when four inclusions are located in front of the crack tip while the medium and the dark gray are for two and one inclusion respectively.

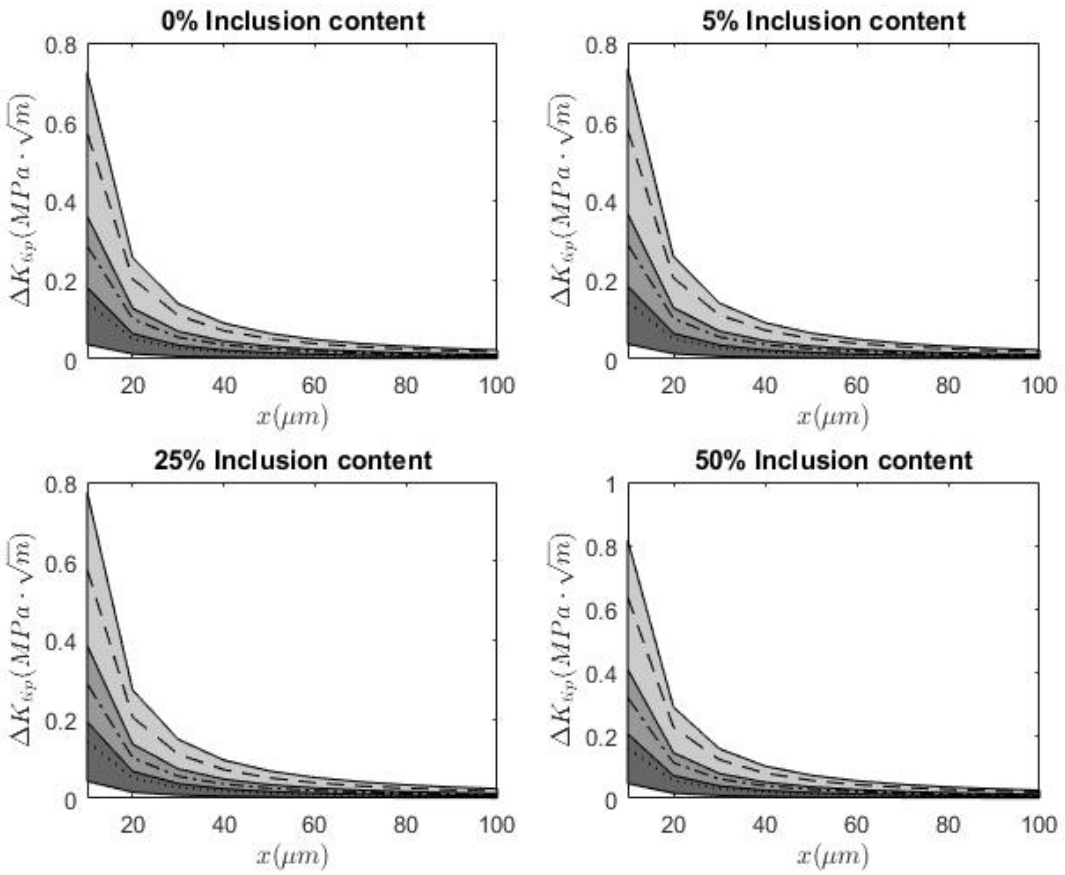

Figure 4.5. ΔK_{tip} decay representation for different inclusion contents, where the dash lines, center lines and the dotted lines are representing the probability of finding four, two and one inclusion respectively in front of the crack tip

Figure. 4.6 summarizes the results of this work and shows that as we add microstructure details to the analytical fracture toughness relation, we capture the trends both in the macroscale 3pt bending tests and microscale scratch tests. The first line (Homogenization) applies the homogenous material behavior assumption using equation 4.9 (matrix only). This line is horizontal and serves as a reference point, since it shows no effect of changing the inclusion content when calculating the fracture toughness since we are only considering the matrix. The second line (Far field interaction) represents the matrix behavior augmented with the far field interaction for the mixture of interacting inclusions using equation 4.13. The third data set (3PB test) illustrates the fracture toughness assessment using macroscale tests: single-edge notched bend specimens loaded in three-

point bend geometry. The fracture toughness was estimated using the ASTM standard relation. As the inclusion content increases, the fracture toughness decreases. This mechanism is influenced by the inter-particle spacing theory as explained by Lee and Yee. The increase in the inclusion content beyond the wetting capability of the epoxy will also introduce a stress concentration and will allow the inclusion to deboned from the matrix [12]. The fourth line (Near and Far field interaction) was constructed using the new formulation proposed here in equations 4.21-4.23 By using the new formulation, we could capture the effect of local inclusions on the stress field generated by the indenter as well as far field effects. A series of data sets representing the maximum and minimum limits of equation 4.22 were plotted using β values of zero and $\pi/4$. These upper and lower limits represent possible inclusion configurations and are shown in Figure 4.6 as dashed lines. The last line (scratch data) is a series of data points representing the fracture toughness assessed using the formula for fracture toughness from scratch data, proposed by Akono *et al*. [5]. Akono's formula, equation 2.21 here, ignores the effect of local inclusions on the stress field. It gives the lowest value and largest discrepancy to the macroscale scratch values. The new formulation proposed here adds to the J-integral formulation found in Akono *et al.* to capture the effect of local inclusions on the stress field generated by the indenter as well as far field effects.

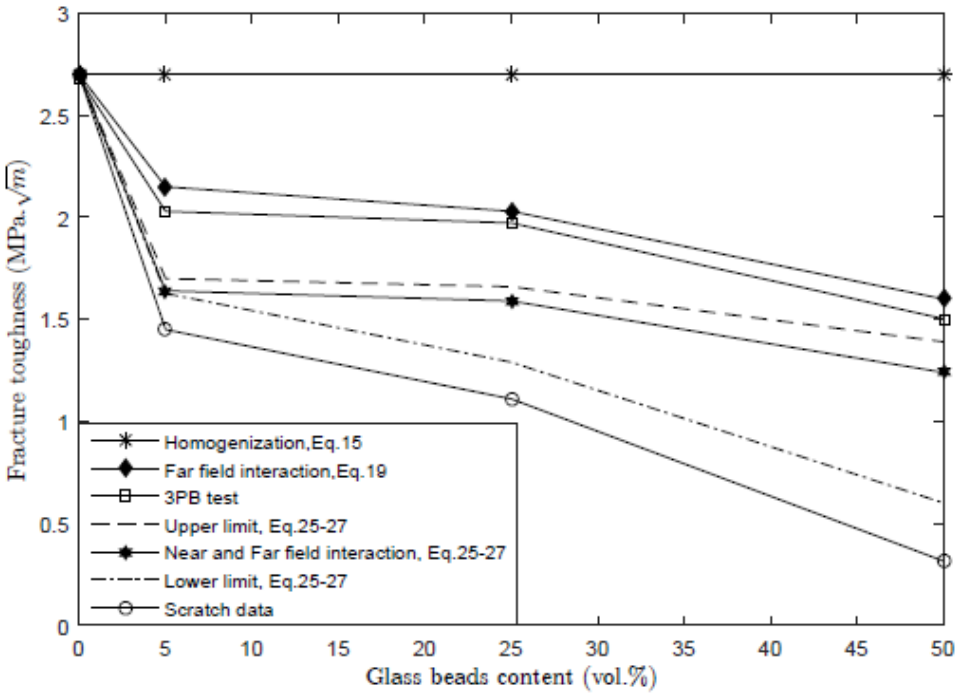

Figure 4.6. Comparison between theoretical and experimental work. Plot illustrate the discrepancy between different methods

The scratch data falls near the bounds of the new fracture toughness formulation, equations 4.21-4.23, capturing the experimental trend. This agreement suggests we have analytically captured the missing microscale mechanisms, which are the significant source of the discrepancy between the fracture toughness derived from macroscale tests and microscale scratch tests. There is still a consistent discrepancy, though much smaller, which is independent of inclusion content and may be due to the following three reasons:

1. We assume mode I failure for the crack propagation in the scratch test. In real tests when applying load, the crack surfaces move relative to each other. There is a possibility that the failure or the displacement will be due to mode I, mode II or mode III. Generally, it is possible to describe the crack tip stress correctly by considering all these failure modes as explained previously in chapter 2, section 2.1.3.

2. The arrangement of the micro-structure in front of the crack tip may be spatially ordered or jammed such that stable damage evolution or unstable reorganization of material is encouraged. This is not considered in any current formulation.

3. Crack branching and coalescence is not explicitly modeled. Cracks will extend into the material if the strain energy release exceeds the energy rate needed to form a new surface. This depends on the ability of the particles to translate position and how much packing constraints exist are in the system.

4.6 CONCLUSIONS

Based on the results, it was concluded that increasing filler content led to an increase of the linear elastic energy release rate and a reduction in the material fracture toughness. The difference between material fracture toughness obtained from standard three-point tests and the micro-scratch test could be described mostly by the effect of microstructural defects in front of the crack tip in micro-scratch tests that have not been explicitly modeled. The micro-scratch test can detect the microstructure by pushing the probe along the specimen surface and does not allow the whole sample structure to assist in redistributing the applied load. On the contrary, in the three-point test we load the material until failure and allow crack stresses to redistribute loading throughout the sample. Thus, local material crushing phenomena is much more prevalent in the scratch test than three-point bending tests and the local stress field is critical in the formulation of the fracture toughness from scratch data. Introducing a region in front of the crack tip to calculate the energy release rate during the fracture process and accounting for the heterogeneity of this region not only addresses the difference in fracture toughness measures, but gives a better understanding of how we can engineer the material to increase fracture toughness for failure on the material length scale.

Chapter 5 EFFECT OF PARTICLE INJECTION ON THE FRACTURE TOUGHNESS OF CRACKED CEMENT [3]

5.1 MOTIVATION

Based on the results of the previous chapter, a theoretical formulation exists accounting for the heterogeneity of the material in front of the crack-tip and its effect on the fracture toughness measure. In this chapter, this formulation will be applied to a real-life problem; injecting particles in a wellbore cracked class G cement paste for leak remediation. The goal of this study is to identify guidelines for selecting particles to seal cracks in aged cement paste class G based on their impact on the mechanical behavior of the matrix. By incorporating particles, we can improve the durability and sustainability of the cement paste but the particle content must be selected to avoid further cracking. To investigate this, silica particles were injected in a cracked class G wellbore cement paste cylinder to model leak remediation. A methodology was developed to determine the direct effect of the microstructure of the cement paste near an existing crack tip. The impact of surrounding cracks, pores, and stiff particles on the fracture toughness of the material was formulated analytically using an extension to the classical *J*-integral derived in chapter 4. Such a formulation allows us to perform a forward analysis in design, avoiding complex numerical models during the particle selection process of the particle repair technology. We find that the introduction of particles into aged cementitious materials for sealing purposes can cause new stress concentrations, which encourage further brittle cracking of the material.

---

[3]Adapted from Al wakeel, S. *et al.* Effect of particles injection on the fracture toughness of cracked cement. will be submitted for publication in the Journal of Construction and Building Materials.

The mechanical behavior of the cement paste containing micro-particles was characterized by standard three-point bending tests. Both the experimental and analytical results agree that an optimum nanoparticle content can be found that extends the lifetime of the cement without encouraging further crack development in the material.

5.2 INTRODUCTION

Particles can be added to the cement to improve some properties such as low electrical resistivity, self-cleaning, self-sensing capabilities, high ductility. The size of such particles ranges from 1 to 100 nm and the surface area is relatively high, shown in Figure 5.1 [90].

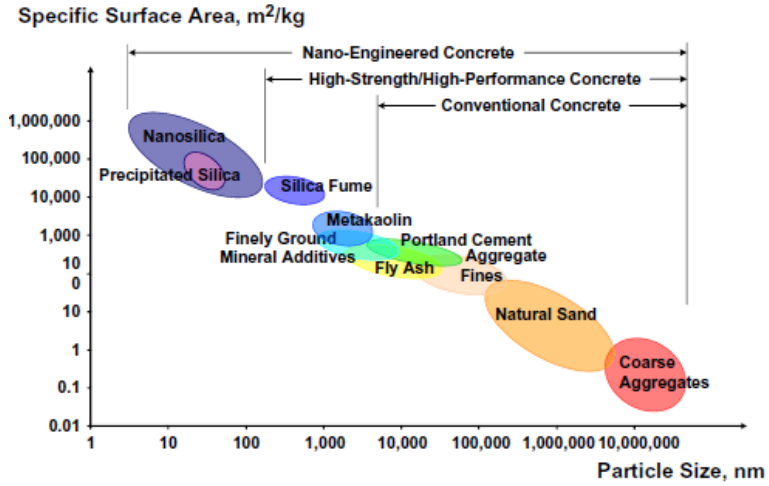

Figure 5.1: Particle size and specific surface area related to construction materials [91].

5.3 ROLE OF PARTICLES IN REPAIRING WELLBORE DETERIORATION

Due to the high surface area-to-volume ratio, particles can be used as a filler to seal the cracks and voids in the cracked concrete [91]. The purpose of injecting particles is to remediate cementing needs and improve durability, which is a vital factor in the long-term performance of the cementitious materials. Particles can reduce porosity and increase strength as they seal cracks and voids induced due to the environment or because of material aging [91]. In chapter 2 section 2.2.2,

we explained that the fracture resistance of concrete or any cementitious materials are strongly related to the C-S-H structure as it occupies more than 60% of the solid volume and generally the structure of C-S-H changes with time [4]. In this chapter, we will study the effect of adding particles to the wellbores cement class G to seal the cracks and voids as they can cause the leakage of CO_2 gas. After injection underground, CO_2 gas can move upward or sideways due to unbalanced subsurface pressures [92]. CO_2 may leak from the interface of different materials, such as the interface of steel casing and cement, the interface between steel casing and cement plug, the voids inside the cement, the crack of steel casing, the crack of cement, and the interface of rock and cement, Figure 5.2, shows possible leakage pathways of the CO_2 gas. It can leak between the cement and the casing, as in pathways a and b, or through the cement itself pathway c, or due to a fracture pathway e, or by pathway f which can be between the cement and formation. The cementing process can be divided into two types: primary cementing and remedial cementing. For both types of oil well cementing, cement slurry is poured into the bottom of the well and presses up into the gap between the steel casing and rock formation [93].

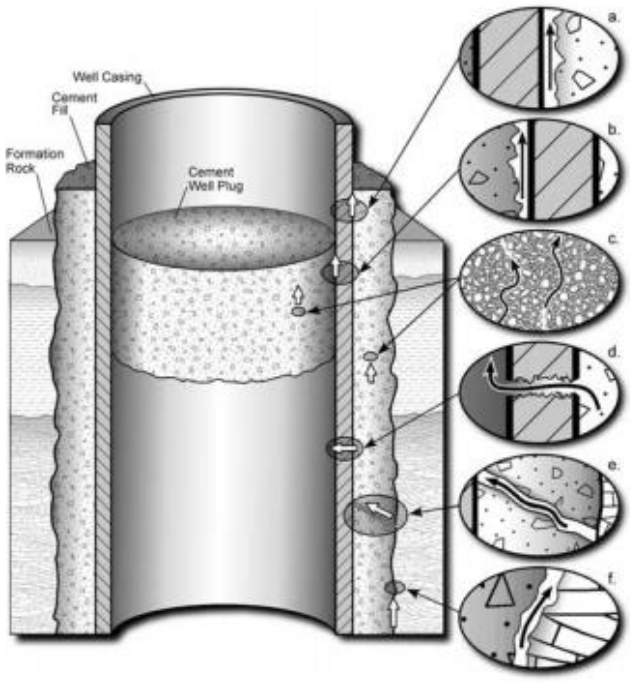

Figure 5.2. Possible leaking paths for CO2 as explained above in section 5.3 [94]

5.4 PREDICTION OF CRACK GROWTH RESISTANCE WITH THE INJECTED AGED CEMENT

With time, borehole cement can result in a more ductile material, due to the distributed micro-cracks developed at the C-S-H structure. The existence of cracks within the material can result in stress relaxation and thus make the cement more ductile. In this work, we aim to select the optimal particles to seal crack networks without introducing new stress concentrations that will encourage embrittlement and further cracking within the material [95]. Jo [96] has suggested that adding silica particles at (53.67–63.9%) and (52.5–62.7%) at seven and twenty-eight to the cement mortar will improve cement compressive strength.

5.5 GLASS G CEMENT PROPERTIES / MATERIAL BACKGROUND

Per API 10A specification for cements and materials for well cementing [97], there are six classes for oil well cement: A, B, C, D, G, and H. Each class can be subdivided into three grades: ordinary (O), moderate sulfate-resistant (MSR), and high sulfate-resistant (HSR). Cement class G and H have better performance when they are in contact with soil than the other cement classes. Other types of cements that can be used for oil well cement include Pozzolanic-Portland Cement, Gypsum Cement, Microfine Cement, Expanding Cements, Calcium Aluminate Cement, ThermaLockTM, Latex Cement, Resin or Plastic Cements, Sorel Cement, and EverCRETETM CO_2, [98-100]. In the US, approximately 80% of all oil well projects adopt Class G and H cement.

5.6 REPAIR TECHNOLOGY OF THE CRACKED SYSTEM

To repair the leaking areas near the steel casing, we propose the particle injection technology to be descended in this section. Figure 5.3 illustrate the technology used in this manner, with two methods that can be used to configure the electrodes. The first way is place an electrode rod through one squeeze point and the other electrode is the steel casing. The second approach is to place two electrodes through the squeeze points. Two holes in the steel pipe, can be used as squeeze points. The particle solutions will be introduced through hollow metal rods that can also carry a positive or negative charge to the repair site. Those metal rods are connected to a DC power source and an anion and cation reservoir will connect to these rods outside of the borehole setup. The setup of the positive and negative rods will be such that the flow of particles in the same direction as gravity. The rod in the borehole wall system can allow for the discharge of particles in the cement alone or in both the cement and rock regions to repair leaks in both areas.

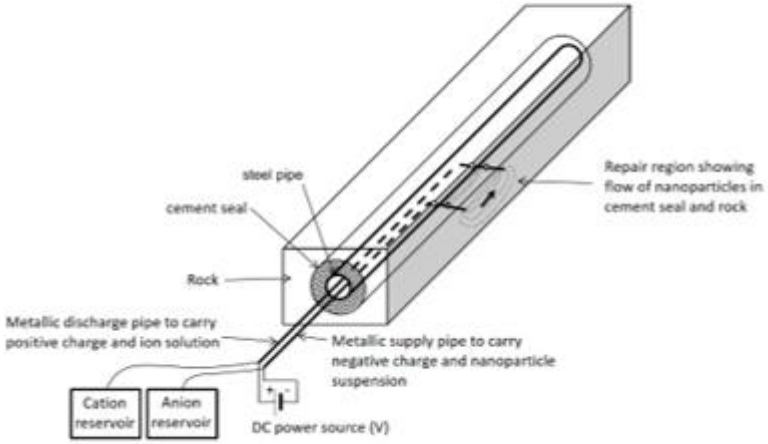

Figure 5.3. particle Injection Mechanism

5.7 DETERMINE FRACTURE TOUGHNESS AND THEORY METHODS

5.7.1 FRACTURE TOUGHNESS CALCULATION

The formulation derived in chapter 4 will be employed to consider the microstructure defects of the aged borehole cement system with the introduction of nanoparticles, as represented in Figure 5.4

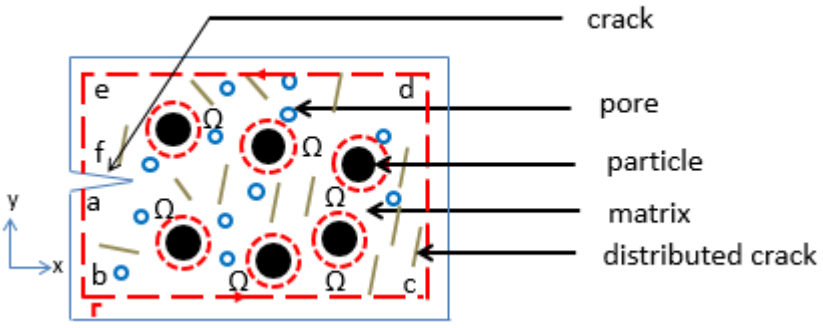

Figure 5.4. A specimen with particles, pores and cracks arbitrary distributed in the matrix

As discussed in chapter 4 this results in the following expression of the *J*-integral [54]:

$$J = f_0 = \frac{1+v_o}{2E_0}\sigma_{ij}\sigma_{ji} - \frac{v_0}{2E_0}(\sigma_{kk})^2 +$$

$$\frac{1}{(1-i)}\frac{1-v^2}{2E_0}\left[i[4tr\sigma.\sigma - (tr\sigma)^2]\right] +$$

$$\frac{\mathbf{1}}{(\mathbf{1}-\boldsymbol{o})}\frac{1}{2E_0}\left[O[4tr\sigma.\sigma - (tr\sigma)^2]\right] +$$

$$\frac{8(1-v^2)}{3E_0}\frac{1-\frac{v_0}{4}}{1-\frac{v_0}{2}}\sigma.\sigma:\alpha$$

where, E_0 is the modulus of elasticity of the cement paste (21 GPa), v_0 cement Poison's ratio (0.2), i is the particles percent content by volume (0%, 5%, 25% and 50%), v particle Poison's ratio (0.17), O is the cement paste porosity, per ASTM C830 [101], an experimental work was performed to calculate the porosity in each slice and the average value was found to be equal to 0.4, the detailed calculation is in Appendix C, section C.1.

5.7.2 COMPOSITE MODULUS

In the present work, three existing models have been selected to estimate the composite modulus needed for equation 4.15. The following assumptions were made in order to calculate the composite modulus: perfect bonding between the matrix and the particles in a cracked sample and random dispersed in the matrix. The subscripts *c, m* and *i* stand for composite, matrix and particles, respectively. The properties of the composite material can be determined from properties of its constituents using the following models [27].

5.7.2.1 VOIGT MODEL (ROLE OF MIXTURE)

The Voigt model gives the composite modulus, E_c, as:

$$E_c = E_i\ V_i + E_p V_p + E_m\ (V_T - V_i - V_P) \quad (5.1)$$

where E_c is the composite Young modulus, E_i is the particle Young modulus (60 GPa), V_i is the volume fraction (0%, 5%, 25% and 50%), E_p is the pore Young modulus (which is equal to zero), V_i is the pore volume fraction, E_m is the matrix Young modulus (21 GPa), v_0 cement Poison's ratio (0.2) and V_T is the total specimen's volume.

5.7.2.2 HALPHIN-TSAI MODEL (SEMI EMPIRICAL MODEL)

A simple semi-empirical equation was developed by Halphin and Tsai shown below:

$$E_c = E_i\ V_i + E_m\ V_m \tag{5.2}$$

5.7.2.3 LEWIS AND NIELSON (ISO-STRESS MODEL)

The Lewis and Nielson model give the composite modulus, E_c, as:

$$E_c = \frac{E_m(1 + AB\emptyset)}{(1 - 1 + B\psi\emptyset)} \tag{5.3}$$

where A is a constant, which for randomly packed spheres takes the value of 1.15 [27],and B is a constant, with B = $\frac{(\frac{E_i}{E_m} - 1)}{(\frac{E_i}{E_m} + A)}$; $\emptyset$ = particle fraction volume, ψ is a numerical factor expressed by ψ = 1+ $\left(\frac{1-\emptyset_{max}}{\emptyset_{max}^2}\right)\emptyset$, $\emptyset_{max}$ = matrix filler packing fraction = 0.625, is picked for prepared systems by using different methods like extraction, injection and compression [27].

The theoretical values of the composite Young's modul are plotted in Figure 5.5. The plot shows that the composite Young's modul increases with increasing volume fraction of the particles. This stems from the fact that the particles modulus is higher than the cement paste modulus.

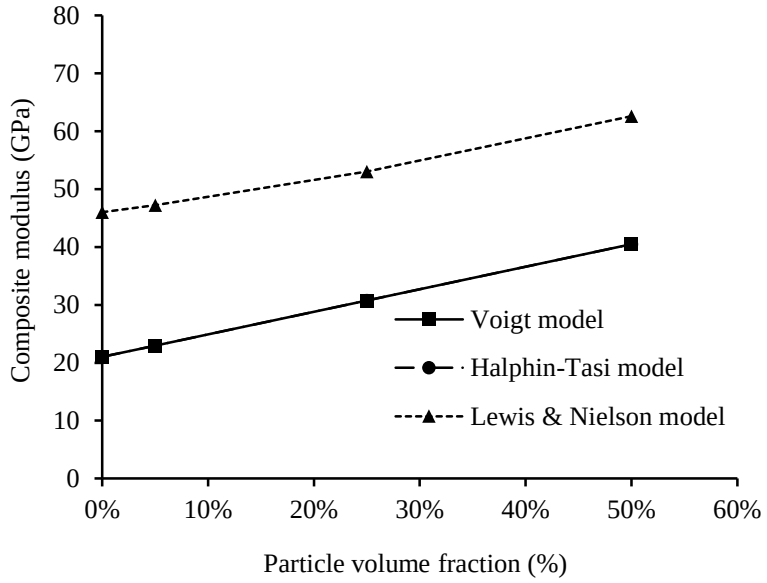

Figure 5.5. Relation between the composite's modulus and the particles volume fraction

5.7.3 SAMPLE PREPARATION PROCEDURE

Following up the procedure prescribed in the API Standard 10A [97], cement class G was mixed at a water-to-cement ratio of 0.44 without the usage of aggregate or additives. The specimens were cylinders with dimensions of 100 mm diameter and 200 mm height as shown in Figure 5.6. A Waring Blender Model 686CS was used to mix the cementitious material, which can be programmed to the speed of 4000±200 r/min for 15 seconds and 12000±500 r/min for 35 seconds. After mixing, the cylinders were placed in water within the first day of mixing, per API 10A Standard, the water temperature was 38°C. The samples were cured for 7 days before testing. A 10 mm slice was removed from the top and bottom cylinder to produce a smooth surface.

Figure 5.6. Sample Cutting Size

After cutting, the sample was immediately sealed.

5.7.4 PARTICLES INJECTION TECHNOLOGY

Particles were injected into the cementitious materials by using external current. This technology was performance according to the ASTM C1202 [102]. As illustrated in Figure 5.7, the cement cylinder was placed in the middle part of the chamber.

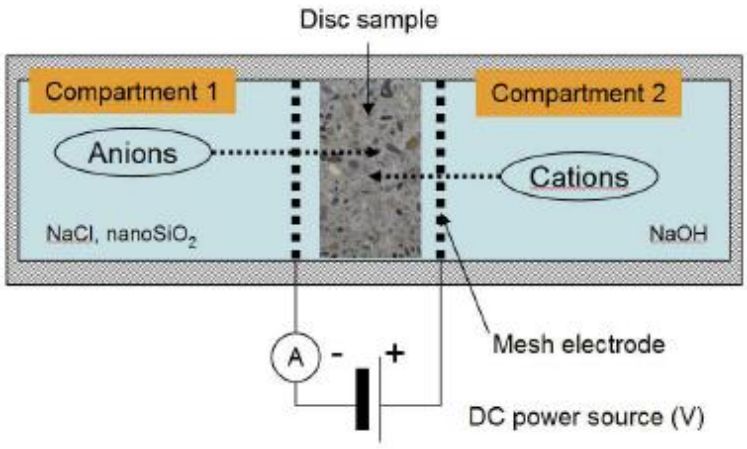

Figure 5.7. Electro-migration chamber used for ionic exchange test

The apparatus used here consisted of two compartments. Compartment 1 was called “the upstream chamber” filled with a sodium chloride solution, and it connects with the negative polarity.

Depending on the external current, the anions of solution in this compartment would be injected into the cementitious material. Compartment 2, was filled with a sodium hydroxide in all cases. The concentrations of sodium hydroxide and sodium chloride were 0.3N and 3% by mass, respectively. The size of the disc sample were 100× 50mm. The particle sizes and types were selected in this study are listed in Table 5.1.

Table 5.1 Different particles Used in Injection Test

particles	Size	Weight %	Manufacturer
SiO_2	7 nm	30	Sigma®
SiO_2	22 nm	40	Sigma®
Al_2O_3	50 μm	40	Sigma®

The voltage magnitude used during the injection was 60V. The penetration is much lower with Class G cement than with regular concrete per ASTM C1202 [102]. The particles were injected from the surface close to the negative polarity. To simulated the underground environmental, the whole test unit was put into an incubator at 49 °C. Over forty percent of particles would generate severe crystal generation which would block the path of injection. In order to inject particles into the oil well cement, the apparatus was run for 12 hours

5.7.5 EFFECT OF PARTICLE INJECTION ON THE FRACTURE TOUGHNESS OF CEMENT

We have developed a sample preparation method and testing plan to experimentally verify the derived fracture toughness trends for the oil well cement. Single Edge Notch Bend (SENB) geometry was used for fracture toughness assessment. Specimen dimensions were selected to satisfy ASTM 399 plane strain requirements [62] as shown in Figure 5.8.A sharp crack was created by inserting a fresh razor blade into the notch.

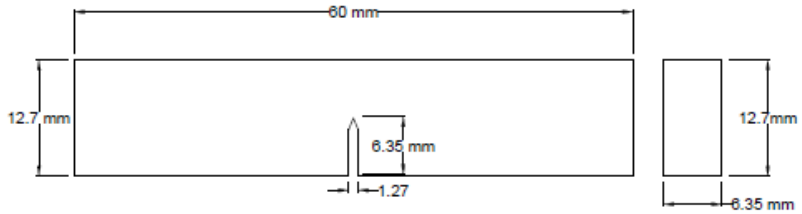

Figure 5.8. Specimen geometry and dimensions

The cylinder was sliced into 7 circular disks as shown in Figure 5.9. At least 3 cylinders with different size (7 μm, 22 μm and 50 μm) injected particles were cut into disks for analysis.

Figure 5.9. Specimen slicing

The challenge in this stage was how to construct specimens from a disk made of cement paste injected by particles such as nanosilica. The material is brittle and soft such that adding any pressure on the disks broke them. The decision was made to extract these specimens using water jet cutting. We were able to extract three pieces from each slice as shown in Figure 5.10.

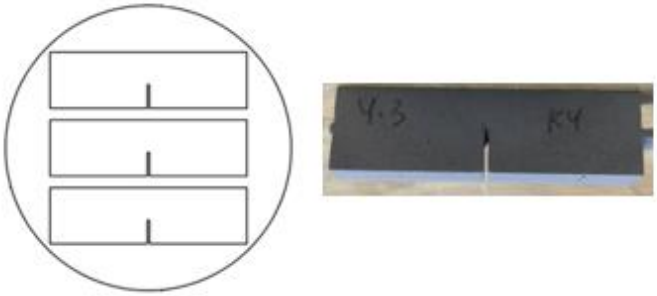

Figure 5.10. Disk with three specimens to be extracted and a sample that has been cut from the repaired cement using the water jet cutter.

5.7.5.1 THE ASTM STANDARD THREE-POINT TEST

The standard three-point test were performed with the aid of an Instron testing machine. A constant displacement load was applied on the specimens. Then fracture toughness was determined using the standard formula for the three-point bend geometry from equations 2.32 and 2.33.

5.8 RESULTS AND DISCUSSION

5.8.1 STATISTICAL ANALYSIS USING ANOVA

Analysis of variance "ANOVA" were performed on the data obtained from the tests. This method was used to analyze the data obtained from the 3p test, a statistical difference was found between the tested data, detailed calculations are listed in Appendix C, section C.2. Figure 5.11 shows the results of this analysis for the SiO_2 particles.

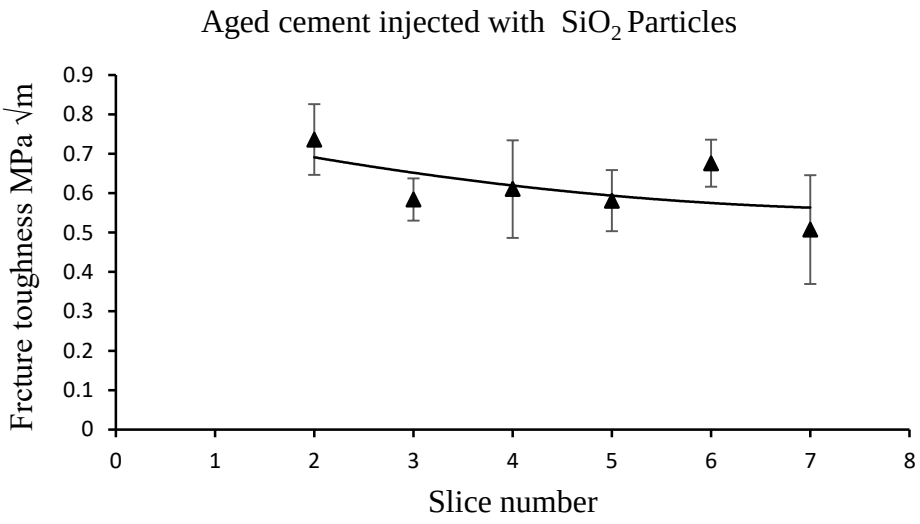

Figure 5.11. Relation between fracture toughness and slice location for cylinders injected with SiO_2 particles

As is illustrated in Figure 5.11, the fracture toughness value is decreasing from slice 2 (with no particles) to slide 7 (injected side of the cylinder).

The following trends were obtained from the application of the different volume fractions of particles considered in the derived formula for the fracture toughness of the aged cement-nanoparticle system.

1. The relation between *J*-integral and crack density for a particles volume fraction of 5 % and porosity 4% is illustrated in Figure 5.12, shows that the fracture parameter *J* will significantly increase as the crack density increases. That is expected since increasing the amount of cracks in the matrix will increase the potential energy in the system and its tendency to fracture.

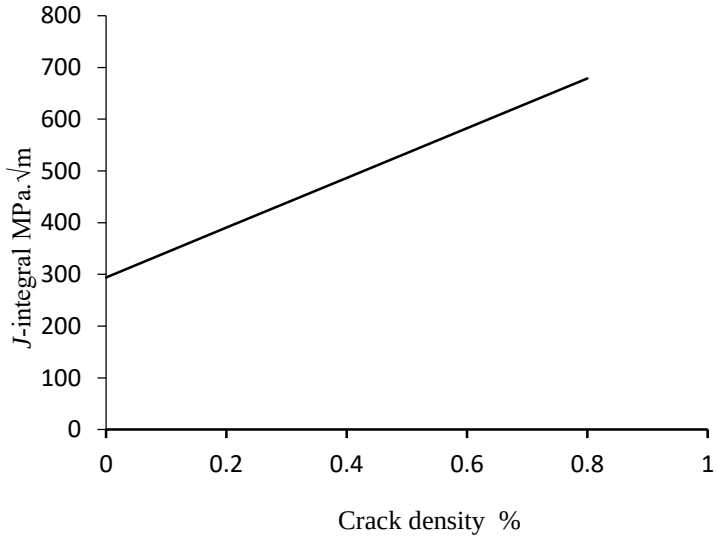

Figure 5.12. Relation between J -integral and crack density values

2. The relation between *J* -integral and particles size for particles contained = 5%, porosity = 10% and crack density = 20%, is illustrated in Figure 5.13 which shows the relation between the particle size and the *J*-integral value. It can be observed that changing the size of the particles has no significant influence on the fracture parameter. That makes sense

since the particles size is of order 10^{-9} m even when we consider particle agglomerate as shown in the last data point.

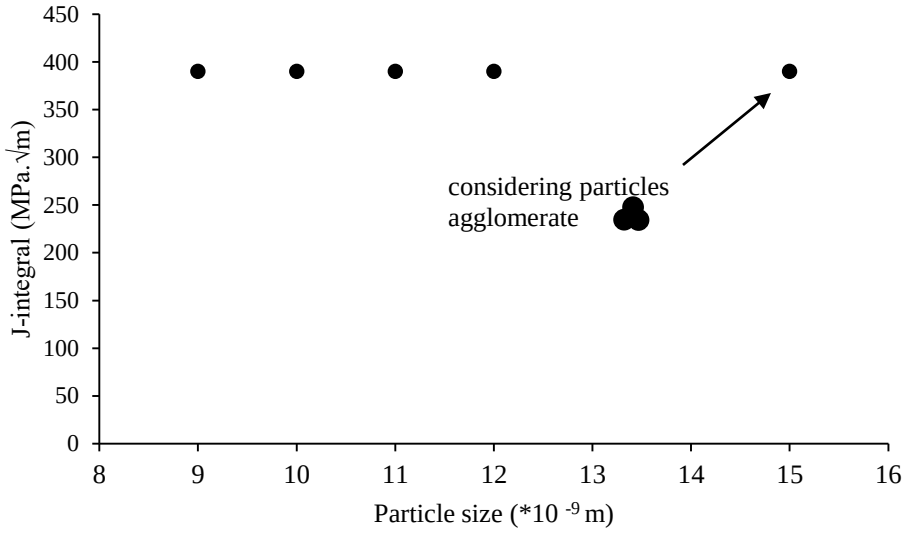

Figure 5.13. Relation between J- integral and particle size

3. The relation between the J-integral and the particle volume fraction for porosity =4% and crack density = 20%, is illustrated in Figure 5.14, which shows that increasing the volume fraction of particles yields a decrease in the J–integral fracture parameter. The reason is that increasing the volume fraction of the particles will increase the brittleness of the concrete and it tendency to develop more cracks as becomes more brittle.

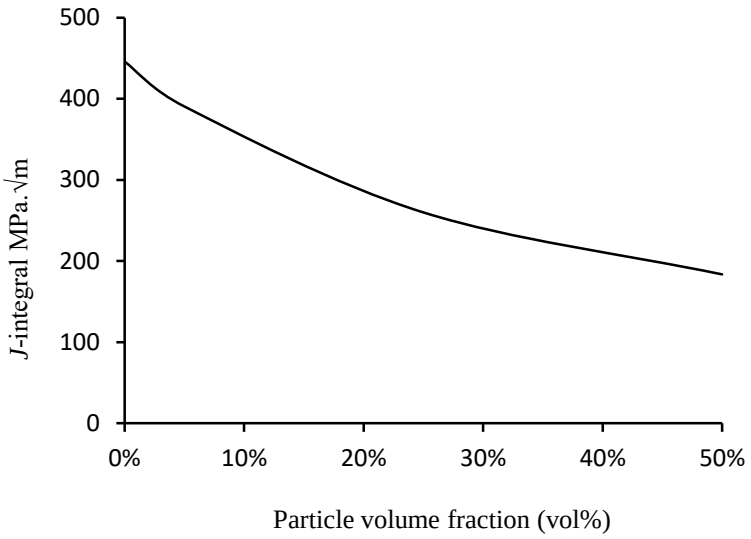

Figure 5.14. Relation between J -integral and particles volume fraction

The inspection of particles into the cracked oil well cement paste can fill the spaces and the cracks in the matrix and act as a seal in the material flow network. Adding the particles would also increase the brittleness of the concrete and its tendency to develop more cracks. By incorporating particles, we can improve the durability and sustainability of concrete but must select a particle content that avoid creating a more brittle material than the existing material. With the newly derived equation, we can now conduct this analysis.

5.9 CONCLUSIONS

Based on the results obtained from the analytical and experiment analysis, it was concluded that:

1. The composites Young's modulus increases with increasing volume fraction of the nanoparticles. This is related to the fact that the particles modulus is higher than the cement paste modulus.
2. The fracture toughness value is decreasing from slice to another, this is due to the different in particle contained in different location within the same cylinder.

3. The fracture parameter *J*-integral significantly increases as the crack density increases. That is expected since increasing the amount of cracks in the matrix will increase the potential energy in the system and its tendency to fracture.
4. It is observed that changing the size of the injected particles has no significant influence on the fracture parameter. That makes sense since the particle size of order 10^{-9} .
5. Similar trend was found from the theoretical formulation and the three-point bending.

Chapter 6 PARTICLE JAMMING EFFECT ON THE FRACTURE TOUGHNESS OF HETEROGENOUS MATERIAL [4]

6.1 MOTIVATION

Based on the findings in chapter 4, and to explain the remaining discrepancy found between the scratch and three-point tests, in this chapter we study how the degree of spatial ordering of the particles will affect the fracture toughness of heterogeneous material [4]. For the spatial arrangement of the inclusion to be the cause of the fracture testing discrepancy, the following conjecture must be true: fracture toughness of a particle composite depends on a statistic of the particle arrangement, and not their exact locations. By applying LEFM in a cracked body of arbitrary shape subjected to mode I configuration, a theoretical formulation is presented where packing scenarios and fracture response are linked using order and jamming as quantifiers. The methodology presented in this work shows that incorporating the degree of randomness in particle packing in determining material fracture toughness will improve structure's ability to withstand local damage without fracturing. This concept is generalized to capture a trend in fracture toughness with a single statistical variable; as mentioned in chapter 2, the translation parameter T used in this study, equation 2.36. In an ordered system, T is equal to one, such as the case of FCC while it equals zero for the case of ideal gas. The orientation order equation was discussed more thoroughly in chapter 2, equation 2.36 [68].

---

[4]Adapted from Al wakeel, S. *et al.* Particle jamming effect on the fracture toughness of heterogeneous material. will be submitted for publication in the Journal of Construction and Building Materials.

6.2 INTRODUCTION AND BACKGROUND RELEVANT TO PREVIOUS WORK

6.2.1 MICROSTRUCTURE ARRANGEMENT AND PARTICLE PACKING

The most suitable way to define the arrangement of inclusions in a system is by knowing how packed the system is, or we can say how jammed or unjammed the system is. The concept of jamming is used to determine the degree of particle packing within a system [103]. At a high density and when applying external load, the particles are in contact with each other and there is no free space available for them to move. In other words, the stress is supported by a network of particles and the close packing of these particles will lead the system to yield [103]. As an application of this problem we consider concrete and cementitious materials at multiple length scales: molecular to macroscale. These scales exhibit different structures each with degrees of randomness or order as characterized by a jamming phase diagram Figure 6.1 [4, 104]. The structure of the hardening cement paste is the core matter in multi-scale modeling of concrete, since it changes upon changing the cement hydration rate (different microstructure at different times). For example, the development of shear strength in the cement matrix has been tied to jamming of the hydration product. By incorporating information from the material structure, as well as the defects, we can better explain the fracturing and cracking of concrete or any composite material [103]. In this study, we will introduce a formula to predict the change in crack-tip SIF due to different particle packing arrangements and validate it numerically.

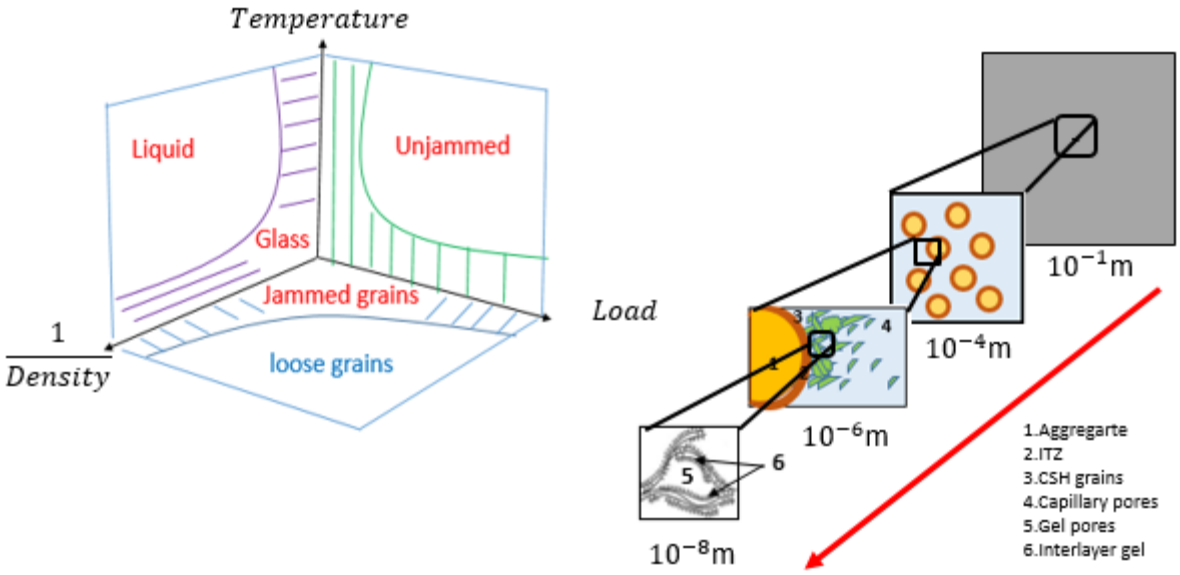

Figure 6.1. Jamming phase diagram [105]*, concrete or cementitious material's structure* [4]

6.2.2 ARRANGEMENT STATISTIC FOR FRACTURE PREDICTION

To study the fracture behavior of a heterogonous material, it is important to investigate the impact of particle packing and arrangement on macro-scale fracture parameters. Within the framework of the LEFM, the concept of the fracture resistance using energy criteria was presented by Irwin and Kies [31]. In 1962, Krafft, Sullivan and Boyle [31] introduced the R -curve. They argued that each material has a distinctive R -curve at a particular thickness under a given loading rate and temperature, and has nothing to do with the initial crack length and specimen size and shape. This work aims to address the problem of a crack growing in a random medium formulated by Planas [1]. Concrete and cementitious materials are heterogeneous with highly complex random microstructure. In concrete the micro-cracks and voids formulation exist even before loading; generally, it is assumed micro-cracks are engaged from strain localization in front of the crack tip forming a zone known as the fracture process zone [9]. Spatial flaw and inclusion distributions

within this zone strongly affect crack growth. Let us represent the fracture process zone by drawing a small cube ahead the crack tip having gradient colors representing different crack growth resistance R as it is shown in Figure 6.2. Since concrete is a quasi-brittle material the fracture process zone will stretch far from the crack tip and engage a variety of different phases in the concrete composite, each with its own crack growth resistance [31]. By assuming fracture mode I under fracture energy force φ, the crack will grow as long as the fracture energy force φ is greater than the crack growth resistances R along the crack track $(\varphi = \varphi_1)$. Assuming R will vary randomly in front of the crack tip based on the nature of these heterogeneous materials, the probability of crack growth is thus totally related to the probability of finding a weaker cube along the crack path, but the crack won't run if there is a strong cube existing in front of the crack path [31]. This type of theory has been explored by Planas to describe the effect of arrangement on fracture resistance, but it can only account for a linear variation ahead of a crack tip, which is not realistic for a 3D stress field and doesn't capture the effect material phases have on each other as the crack grows. A more accurate description of the microstructure is needed.

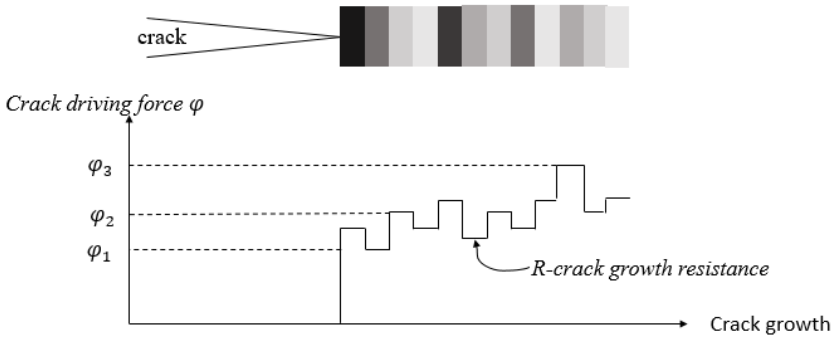

Figure 6.2. Problem statement proposed by Planas [1]

6.2.3 MICROSTRUCTURE RELATED THEORY: RADIAL DISTRIBUTION FUNCTION

In order to understand the physical behavior and fracture of any material which consists of different regions, such as concrete, it is important to consider the microstructure information, including the

spatial distribution of phases in the material. A number of approaches can be used to describe the spatial distribution within the material [104]. The Radial Distribution Function (RDF) computes the possibility of finding a particle at a distance between r and $r + \Delta r$ from a reference particle. It is a normalized pair correlation function. It is used to define how the particles arranged inside material structure [104]:

$$g_{(r)} = \frac{n_{(r)}}{\rho * 4 * \pi * r^2 * \Delta r} \tag{6.1}$$

where $g_{(r)}$ is the radial distribution function, $n_{(r)}$ is the number of particles in a shell of width Δr at a distance r, ρ is the particle density

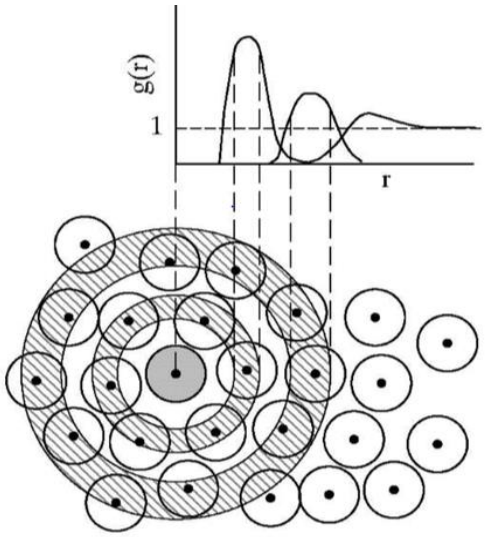

Figure 6.3. Radial distribution function in two dimensional fluids [105]

The RDF can be plotted versus the inter-particle separation distance r as shown in Figure 6.3. The probability of finding a particle at a distance equal to the particle diameter is zero while when increasing the distance r there is a high probability of finding particles. In other words, at short separation distance (less than the particle diameter) the RDF is zero while it is equal to 1 at large

value of r. This is the case if there is no long-range order in the system and the correlation is lost, *ie*. the system become more homogeneous [103], as illustrated in Figure 6.3. Flexible solids have fixed particles positions that do not overlap. The most suitable way to define this system is by defining how packed the system is or jammed. A jammed system is a mechanically stable system but not in its lowest energy state. The density of particle packing can be defined as a function of space occupied by the particles; the following formula represents the packing fraction [103]:

$$\emptyset = \frac{A_{particle}}{A_{box}} = \frac{V_{particle}}{V_{box}} \quad (6.2)$$

Applying any external force on the jammed system may cause particle rearrangements if the system is packed but in a jammed state. In this case, the material turns into an amorphous solid and develops a yield stress [103]. To confirm the jamming effect, we will present a comparison between the theoretical formulation and the numerical analysis in the next section.

6.3 FRACTURE FORMULATION

6.3.1 LINEAR ELASTIC FRACTURE MECHANICS

The fracture of the brittle material can be modelled by LEFM if the fracture process is small compared to the size of the structure [1]. The sharp drop of the stress strain curve characterizes the behavior of the quasi-brittle materials after the highest stress is reached as illustrated in Figure 6.4. Tension softening behavior can be elucidated by damage mechanics due to the initiation, growth and coalescences of microcracks [30]. Griffith was the first who assumed that preexisting cracks could be found in most quasi-brittle materials. He determined how crack size would change with the change in energy, ΔU [32]. LEFM will be implemented to study crack resistance in this study.

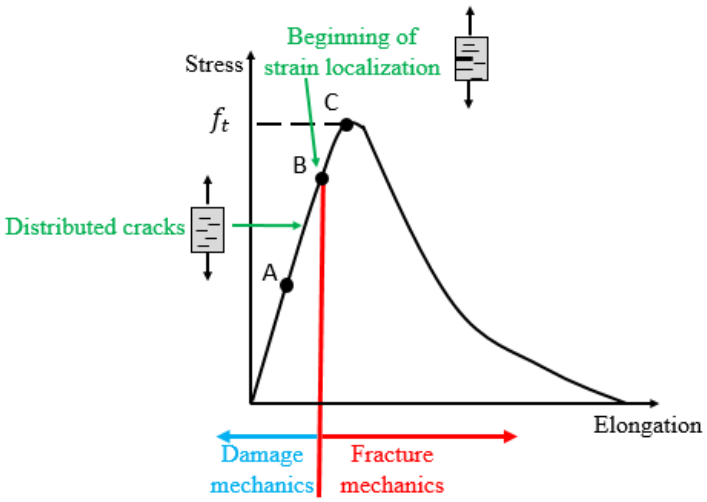

Figure 6.4. Crack propagation in concrete under axial tension [30]

6.3.2 FRACTURE TOUGHNESS BASED ON FINITE ELEMENT ANALYSIS

ABAQUS [58] has the capability to calculate the LEFM stress intensity factors parameter K_I within the ABAQUS postprocessor using the displacement extrapolation method. The SIF is determined by implementation of the concepts of plane strain conditions, the J-integral, and mode I failure. A study has been conducted to examine the sensitivity of the solution. Various levels of refinement were generated in the model domain using the mesh tool to ensure the convergence of the solution. As the mesh size is reduced (number of elements increased), the change in the value of the SIF decreases as shown in Figure 6.5. The mesh refinement study showed the influence of the number of elements in front of the crack tip on the SIF value.

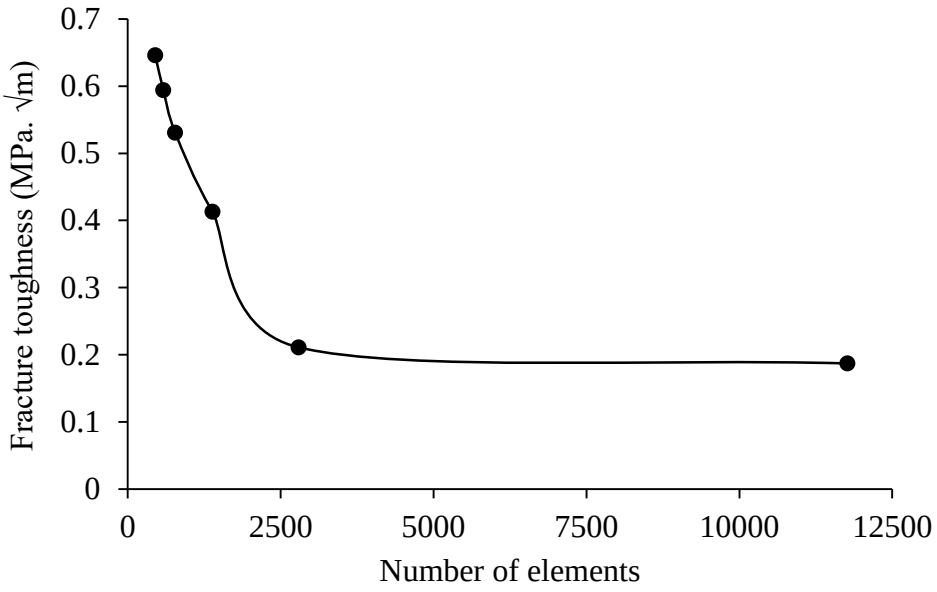

Figure 6.5. A Convergence study of the fracture toughness as the number of elements increases

The element size at convergence used in this study is 0.5 mm and the element shape is rectangular. Figure 6.6 shows the meshed element used in this analysis.

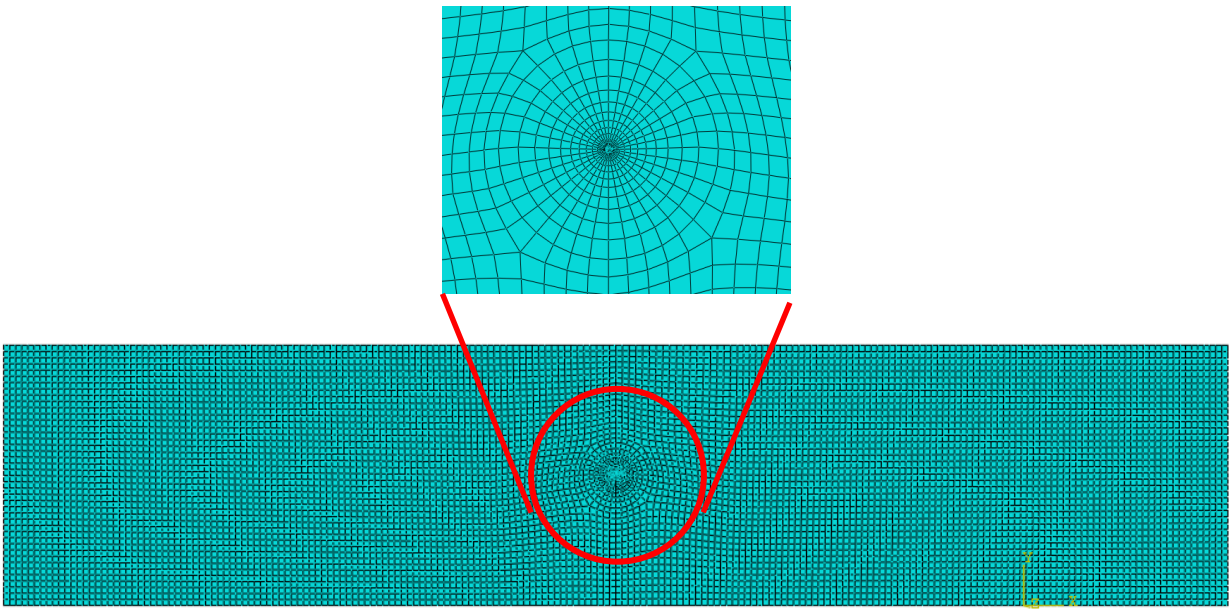

Figure 6.6. Mesh size and shape used in this analysis

A series of numerical simulations was conducted selecting different inclusion Young's moduli (E_i) for the embedded inclusion in front of the crack tip to evaluate the relation between the normalized

fracture toughness (K_I/K_0) and the normalized modulus of elasticity (E_i/E_0). E_0 and E_i represent the Young's modulus for matrix and inclusion, respectively and K_0 and K_I are the fracture toughness without and with inclusion respectively. The results are presented in Figure 6.7 (b). As the value of the inclusion stiffness increases the stress intensity factor value decreases. A good agreement was found between the results of this analysis as presented in Figure 6.7 (a & b) and the experimental work presented by Papaioannou et al [106] as shown in Figure 6.7 (c). The same trend found from the theory for various ratios of Young's modulus (E_i/E_0) presented by Li et al. [49] as illustrated in the Figure 6.7 (d).

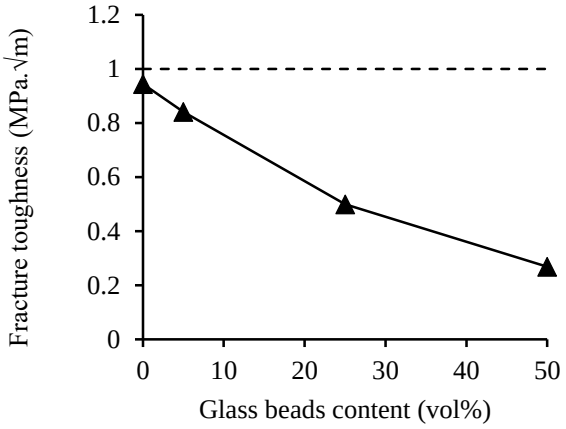

(a)

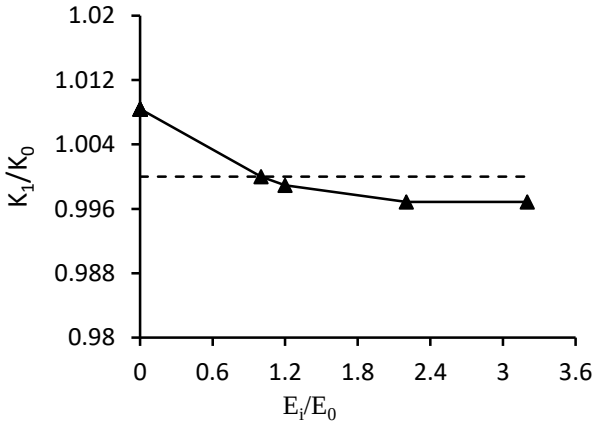

(b)

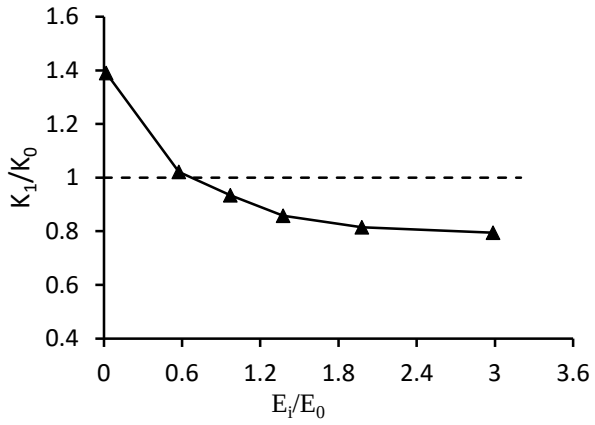

(c)

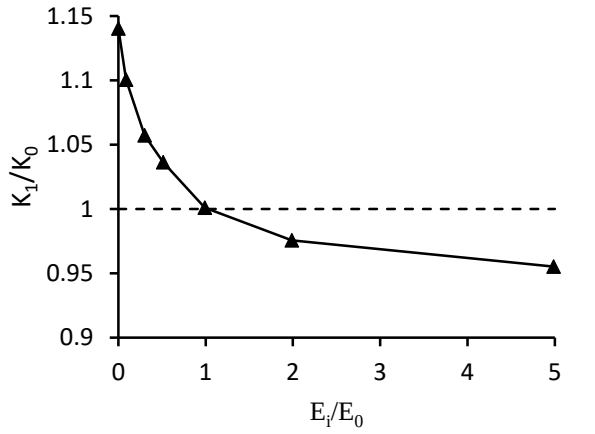

(d)

Figure 6.7. Comparison between numerical and theoretical formulations behavior of crack-inclusion interaction within crack tip field for mode I failure. The fracture toughness has different values based on different materials: (a) The average values of the fracture toughness from the scratch test for the curves showing a kink-current work. (b) Fracture toughness from numerical simulation-current work. (c) Numerical formulation for central cracked specimen by Papaioannou et al [106]. *(d) Theoretical formulation for the impact of single inclusion located ahead of crack tip in 3PB specimen by Li et al* [49].

6.3.3 NUMERICAL MODELING USING ABAQUS

In chapter 4, we defined a volume in front of the crack tip and investigated the effect of the inclusion existence in this volume and their spatial statistic on the material fracture toughness. We assume that the LSRV is a symmetrical spherical domain of finite size located in front of the crack tip. Linear elastic inhomogeneous behavior is assumed. Jamming can be introduced by changing the particle packing in the LSRV. For an accurate prediction of the material fracture, we accounted

for the statistical arrangement or packing of the particles in the LSRV. We will briefly consider three microstructure scenarios of dimensional bodies of heterogeneous material having a straight crack. The three bodies contain identical number of particles but different configurations or arrangement as shown in Figure 6.8. The left panel represents a system which contains a symmetric distribution of particles; the middle panel an asymmetric distribution; and the right panel shows a system that represents clumped or jammed particle geometry. The clumped particles consist of two particles that behave as a single rigid body. These clumped particles do not overlap and will not break apart regardless of the forces acting upon them. For the three different particle arrangements, attention was focused on investigating the variation of the stress intensity as a function of particle arrangement.

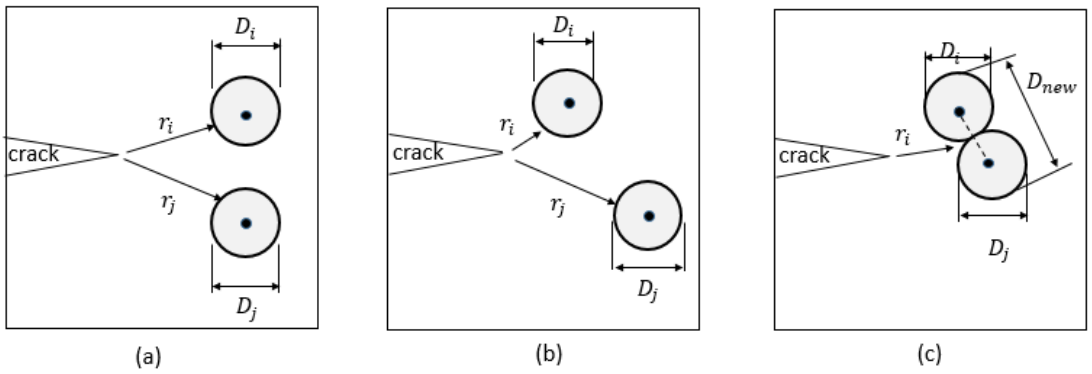

Figure 6.8. 2D problem fluctuating particles arrangement: (a) ordered particles (b) randomly arrangement of particles (c) clumped particles

6.3.4 THEORETICAL CONSIDERATION FOR PARTICLE ORIENTATION

To capture the fracture behavior and the crack growing in a random material, an expression for the change in the potential energy proposed by Karchanov *et* al [54] will be used. The location of the particle is defined by the angle β with respect to the crack tip as shown in Figure 6.9. Equations 4.21-4.23, presented by Li et al [49] and explained in chapter 4, were used to calculate the change in the SIF where the inclusion is symmetrically placed with respect to the crack plane, is again

applied here to model the interaction of the stress field from the crack and any other microcracks or pores.

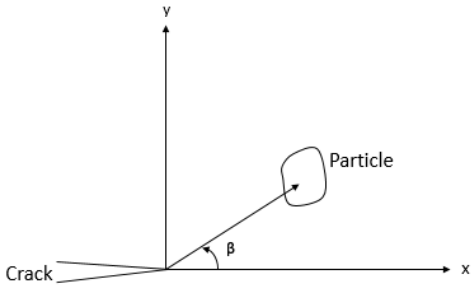

Figure 6.9. Arbitrary particle shape located in front of a crack tip

$$K_{tip} = K_0 + \Delta K_{tip} \tag{6.3}$$

where K_0 represents the stress intensity for the matrix with no particle and ΔK_{tip} represents the variation of the stress intensity induced by a particle orientation within the crack tip field as given by the following equations [73]. The change in the stress intensity for an individual circular particle located at (r, β) can be formulated by the equation below:

$$\Delta K_{tip} = \frac{\pi\, E\, e^T\, R^2 \cos(\frac{3\beta}{2})}{6\sqrt{2\pi}(1-v)r^{3/2}} \tag{6.4}$$

where: ΔK_{tip} is the change in the stress intensity for individual circular particle, E the moduli of the particle, R particle radius and e^T the strain at (r, β). This relation was derived based on energy changes provided by the induced stresses considering a contour around the crack tip.

The contribution of multiple particles to the stress intensity will be considered by integrating over particle volume and material volume:

$$\Delta K_{tip} = \frac{E\, e^T}{6\sqrt{2\pi}(1-v)} \int_0^{R_c} \rho(R)\, dR \int_{A(R)} \frac{1}{r^{3/2}} \left[\cos\left(\frac{3\theta}{2}\right)\right] dA \tag{6.5}$$

where $\rho(R)$ represents the concentration of particles per unit volume and $A(R)$ is the material area around the crack tip [73]. We have chosen to consider the clumped particles as an elliptical particle as shown in Figure 6.10. The strain in the ΔK_{tip} expression is expressed in terms of particle geometry and loading orientation as introduced by Kachanov et al [54]:

$$\varepsilon = \frac{P}{E}\,\frac{1}{A}\,\pi a[a - (a+b)\cos 2\alpha] \tag{6.6}$$

where a, b are the axes of the elliptical particle and α is the angle of the uniaxial loading P.

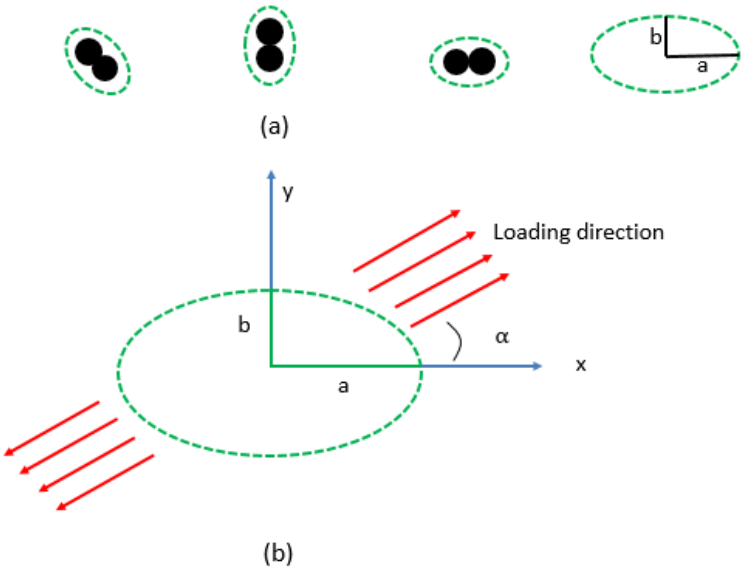

Figure 6.10. (a) Clumped particle shape considered in the present work
(b) Clumped particle under uniaxial loading

Lastly, we can simulate the orientation effect of the clumped particles by combining the ΔK_{tip} equation for multi-particles and the above strain equation for different particle orientation as shown in Figure 6.11.

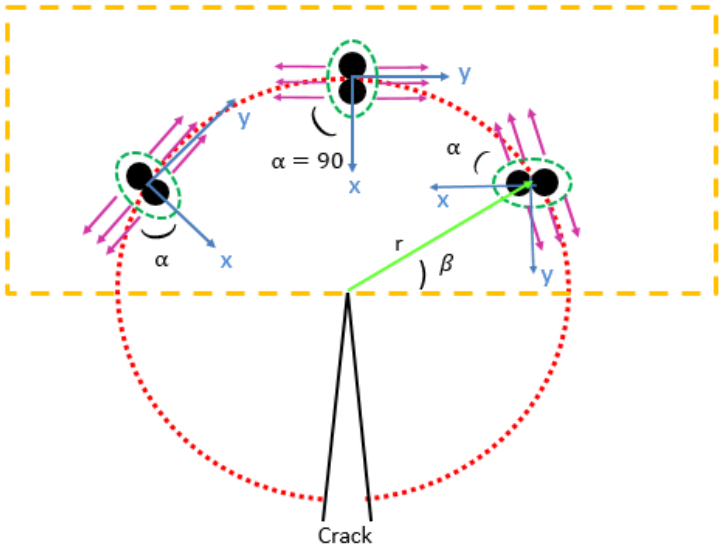

Figure 6.11. Arbitrary particle shape located in front of a crack tip

6.4 RESULTS AND DISCUSSIONS

To allow for a direct forward design method, a key insight from this work shows the analytically formulated particle orientation effect in the crack near field on the fracture toughness of the composite material. Various particle configurations were simulated to verify the theory that the jamming and configuration systematically affect the fracture toughness irrelevant of the particular inclusion locations. A series of numerical simulations was conducted selecting 60 exclusive fields of ordered, random and clumped arrangements, MATLAB code is generated for this purpose, the commented MATLAB code is shown in Appendix D, section D.1. Figure 6.12 shows examples of different configurations that were considered in this study. More configurations are in Appendix D, section D.2.

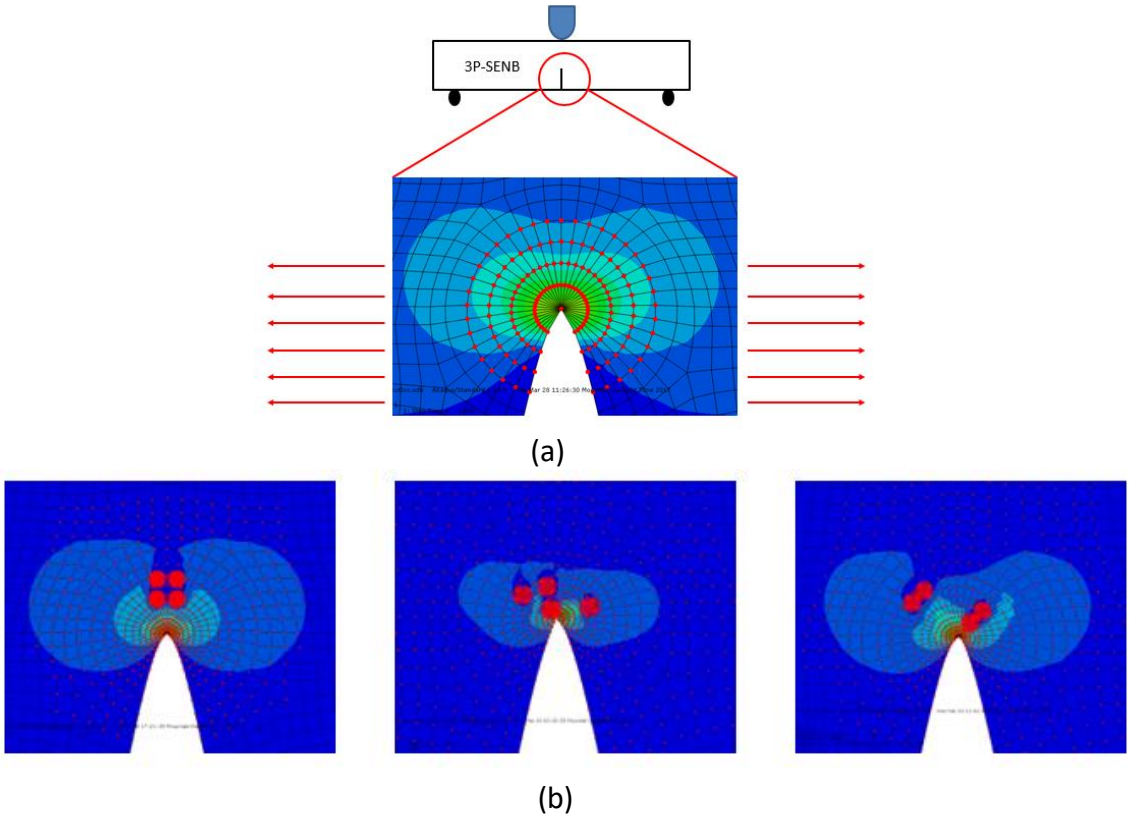

Figure 6.12. (a) Stress field around the crack tip (b) Different particle arrangement, for more detailed configuration see appendix D

As the interest of this study is to investigate the interaction between the SIF and the particle arrangement, a comparison was made between theoretical and numerical analysis summarized in Table 1. It can be noticed that the differences between numerical results and analytical results are in good agreement with less than 2% difference.

Table 6.1. SIF values calculated using average of 60 fields numerical and theoretical analysis for each arrangement

Arrangement	Theory		2D ABAQUS	
	ΔK_{tip} (MPa. $\sqrt{\text{m}}$)	STDEV	ΔK_{tip} (MPa. $\sqrt{\text{m}}$)	STDEV
Ordered	0.235	0.0753	0.231	0.152
Random	0.505	0.0603	0.490	0.207
Jammed	0.7761	0.2204	0.761	0.387

Since the above results are only for one parameter set, a parameter study for was conducted to determine the maximum effect the particle arrangement could have on this geometry. Different

particle sizes and modulus of materials were used to study the effect of changing these variables on ΔK_{tip} for 60 arrangements. Summary of this study is listed in Table 6.2, using double and half values of particle size and double and half values of the modulus. As shown in Table 6.2, when doubling the particle size twice the difference in the ΔK_{tip} value is observed between the ordered and the jammed arrangement than the ΔK_{tip} value found in Table 6.1. This shows that while the effect of arrangement is proportionally smaller than other contributions to the fracture toughness for our experiment, it can be more prominent depending on the composite properties.

Table 6.2. Summary of the variables considered for each arrangement used in this study

Parameter study		Arrangements		
		Ordered	Random	Jammed
Double particle size	ΔK_{tip} (MPa$\sqrt{m}$)	0.464	1.374	2.343
	STDEV	0.029	0.067	0.056
Half particle size	ΔK_{tip} (MPa$\sqrt{m}$)	0.044	0.072	0.153
	STDEV	0.003	0.004	0.025
Double modulus value	ΔK_{tip} (MPa$\sqrt{m}$)	0.385	0.574	1.035
	STDEV	0.037	0.024	0.084
Half particle value	ΔK_{tip} (MPa$\sqrt{m}$)	0.079	0.164	0.202
	STDEV	0.007	0.027	0.013

6.5 EXTEND FORMULA CONSIDERING SPATIAL ARRANGEMENT OF MICRO-STRUCTURE

To generalize the trend observed in section 6.4, namely that arrangement is linked to stress intensity of a material, we introduced the concept of translational order parameter T defined in equation 2.36, which measures the degree of spatial ordering. By using finite element analysis with the Abaqus software and through the displacement extrapolation method during post-processing based on nodal displacements near the crack tip, we developed a systematic study to test for a trend

in fracture toughness as a function of translation order of the inclusions within a composite material. A 3D model was generated to consider particle arrangement on the fracture toughness. Figure 6.13 shows the three-point bending simulation of the model used in this work.

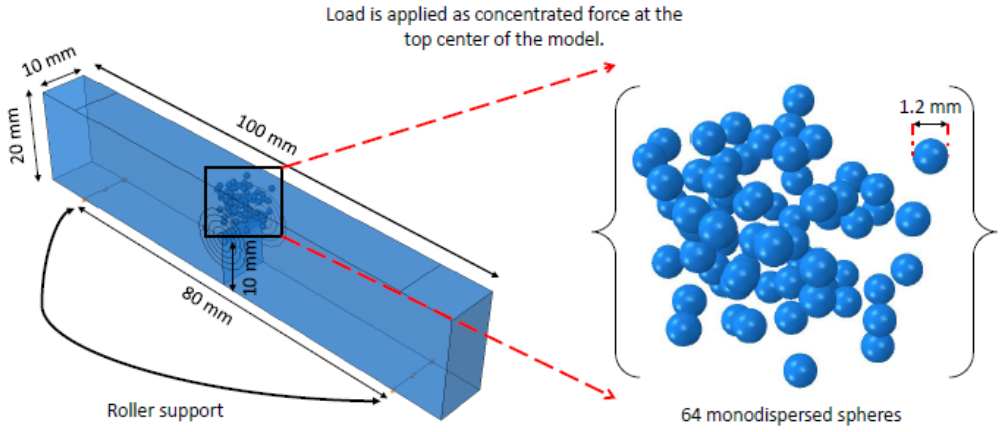

Figure 6.13. 3D geometry and boundary conditions used in this study

As shown in Figure 6.13, particles were placed randomly in the LSRV in front of the crack tip to study the impact of particle arrangement on the SIF value. Numerous instances of randomly arranged inclusions with computed T parameters were tested in bending. With this we were able to generate the trend seen in Figure 6.14.

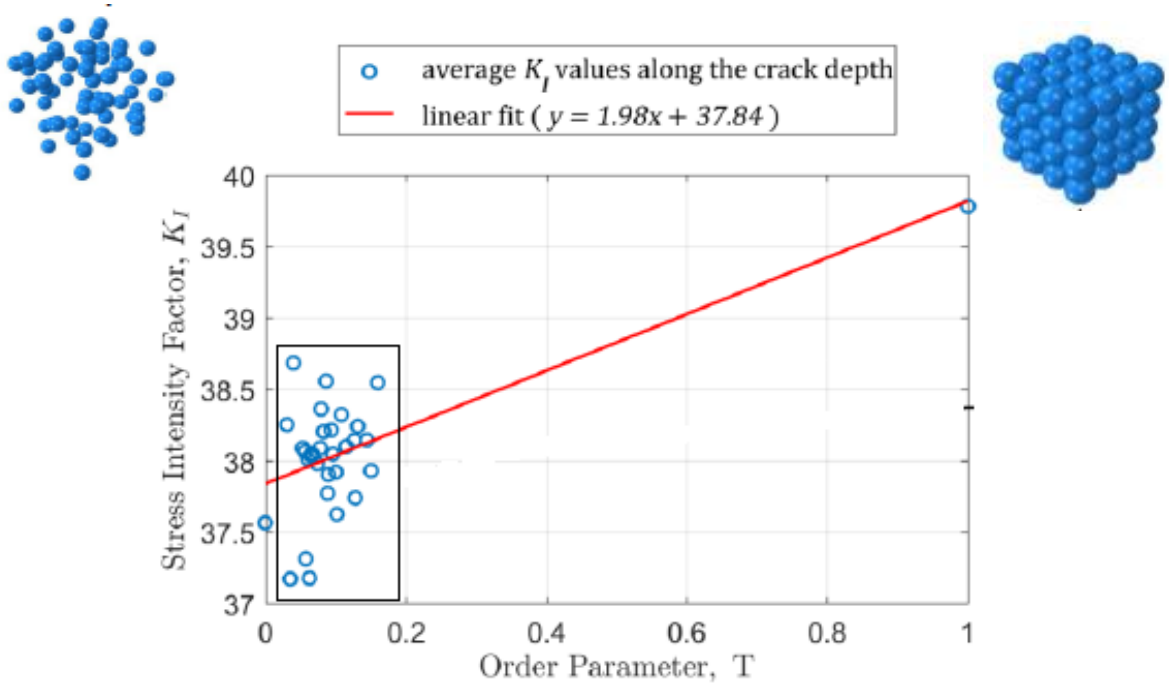

Figure 6.14. Randomly arranged inclusions with computed T parameters in front of a crack tip

Figure 6.14 clearly demonstrates that the state of particle ordered represented by the T parameter will have impact on the SIF value. As the system approaches the ordered state, the value of SIF increases and this would encourage the cracks to initiate and propagate. The difference in the SIF magnitude in Figure 6.14 makes sense since it matches the difference we were seeking in the remaining discrepancy between the scratch and 3p-tests shown in Figure 4.6 after addressing the near and far field microstructure interactions. As shown in the parameter study, a larger difference due to particle arrangement may be observed if different material parameters are considered.

6.6 CONCLUSIONS

By exploring a set of simple systems of different particles packing with the same volume fraction of particles, we quantified the packing effect on the material's fracture toughness. Results shows that for accurate prediction of the stress intensity factor, it is necessary to account for the material microstructure including particle packing and orientation. Introducing jamming and unjamming

effects in the system, meaning that the system moves to its lowest energy, it becomes more stable and rigid. According to this definition, in an unjammed heterogeneous material with low volume fraction of particles and at a certain stage of stress, the particles are free to explore different arrangement within the system. This will encourage the crack to propagate.

1. This chapter provides an evaluation of the SIF based on particle packing and arrangement near the crack tip in a heterogeneous material.
2. A good agreement between the theoretical and the numerical analysis based on the SIF values was fond for different particle configurations.
3. For an accurate calculation of the SIF, triangular singular elements were considered at the crack tip in the finite element analysis.
4. As the mesh size is reduced, the change in the value of the SIF decreases.
5. For different particle sizes selected to be embedded in front of the crack tip, the SIF value decreases as the particle size increases.

Chapter 7 CONCLUSIONS AND SUMMARY

7.1 SUMMARY

This dissertation presents methodological contributions toward incorporating material heterogeneity in particulate composites via the degree of spatial ordering, disordering and packing of the inclusions in determining the fracture toughness of the heterogeneous material. In addition, the overreaching theme was to provide insight into the investigation of the effect of inclusions in front of a crack tip as given by their spatial statistics, arrangement and orientation on the fracture resistance value. Specifically, this research addresses the following contributions.

7.2 METHODOLOGICAL CONTRIBUTIONS

Each of the four chapters present a concept as summarized in the following sections:

7.2.1 VERIFY FRACTURE TOUGHNESS MEASUREMENT DISCREPANCIES

In chapter 3, heterogeneity was considered near the indenter tip. A study of the impact of microstructure on micro-scale fracture parameters was presented using an experimental and theoretical investigation of the fracture toughness of a representative composite material consisting of glass beads embedded in epoxy using micro-scratching and conventional three-point bending tests. A discrepancy was found between the fracture toughness obtained from standard three-point test and the micro-scratch test as described in chapter 4, is shown in Figure 7.1. Based on this finding and to capture the effect of local inclusion on the stress field generated by the indenter, the need for an updated *J*-integral formulation for micro-scale tests was clearly demonstrated due to the interactions of inclusions with the scratch probe.

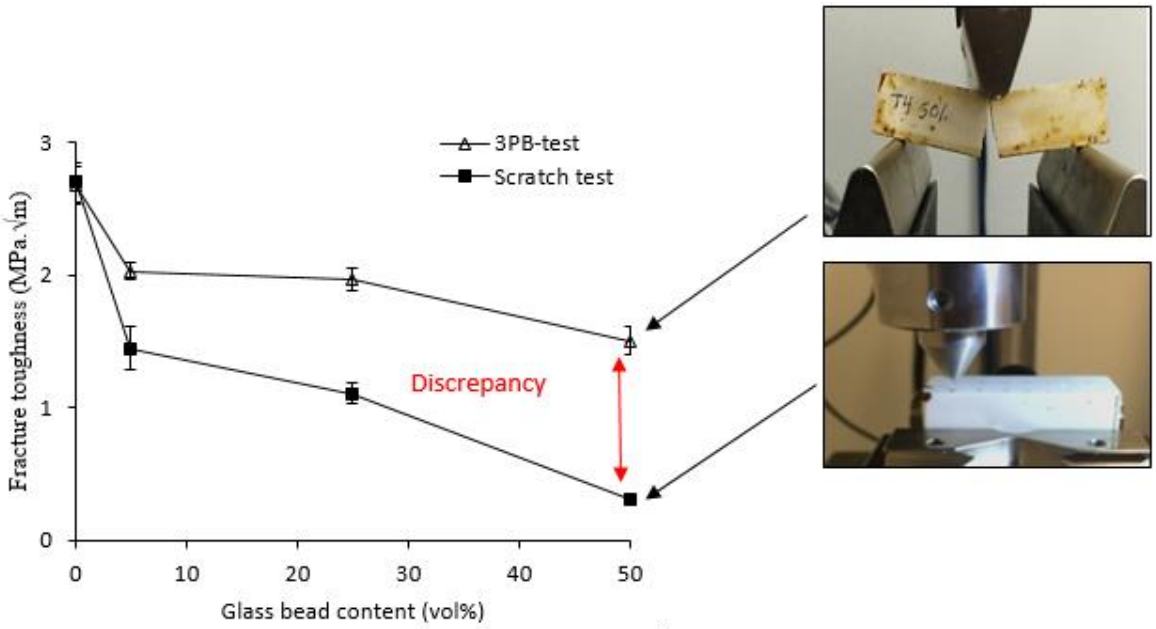

Figure 7.1. Fracture toughness range for different glass beads content using scratch and three-point tests

7.2.2 NEW FORMULATION FOR DATA ANALYSIS TO DESCRIBE DISCREPANCY

In chapter 4, we proposed a new formulation required to obtain agreement between scratch and three-point fracture parameters by updating the J-integral formulation found in Akono et al [5]. by introducing the heterogeneity to capture the effect of local inclusions on the stress field generated by the indenter.

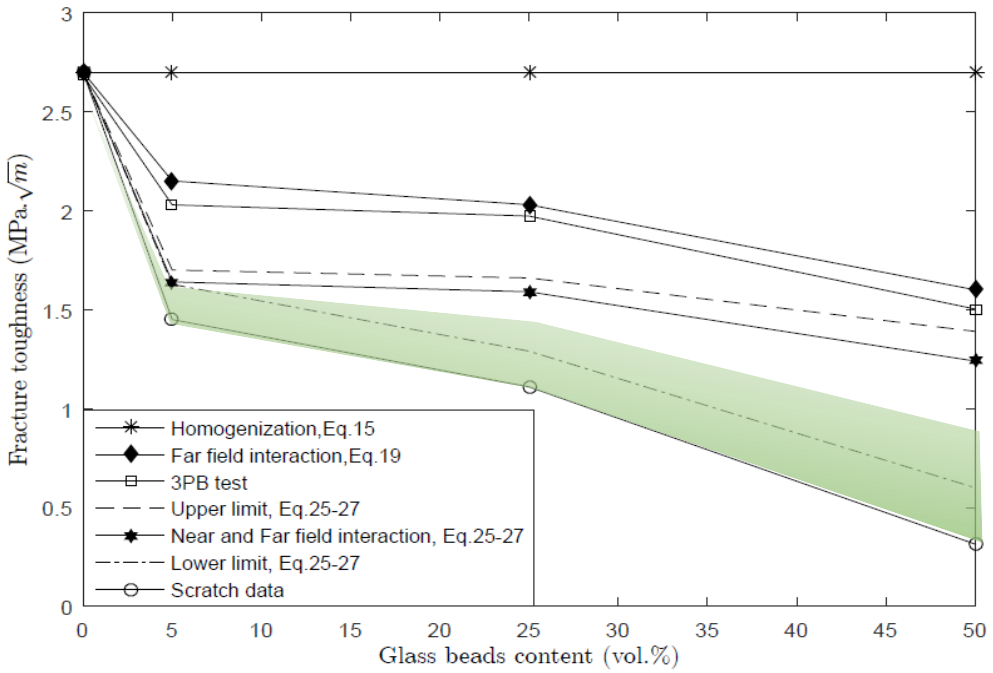

Figure 7.2. Comparison between theoretical and experimental work. Plot illustrates the discrepancy between different methods

Chapter 4 addressed the following key points:

- Introduces two regions in front of the crack tip to account for the heterogeneity (pores, cracks, and inclusions) of these regions to address the difference in fracture toughness measures.
- Gave a better understanding of how we can engineer the material to increase fracture toughness for failure on the material length scale.
- Further consideration of inclusion arrangement is needed.

The derived formulations match the experimental behavior. Existing crack growth design considerations of random composites rely on numerical models that employ an inverse design process. The results of this work allow us to move towards a forward design method to design microstructures for improved fracture resistance.

7.2.3 APPLICATION: BOREHOLE CEMENT

In chapter 5, the main finding was that the introduction of particles into aged cementitious materials for sealing purposes can cause new stress concentrations that encourage further brittle cracking of the material. The mechanical behavior of the cement containing particles was characterized by standard three-point bending tests. Both the experimental and analytical results agree that an optimum nanoparticle content can be found that extends the lifetime of the cement without encouraging further crack development in the material. This result is illustrated in Figure 7.3. The images from the left to the right side of the figure shows the stages of cement samples behavior at different time periods. The first image shows newly mixed cement that has a considerable amount of voids. With aging, loading and other behaviors such as shrinkage the amount of the cracks will increase and that is illustrated in the second image. By adding particles into the network to seal leaks, as illustrated in the third image, it is expected that the cracks would be sealed but at the same time the fracture parameter J-integral will decreases with the time as illustrated in the curve in Figure 7.3.

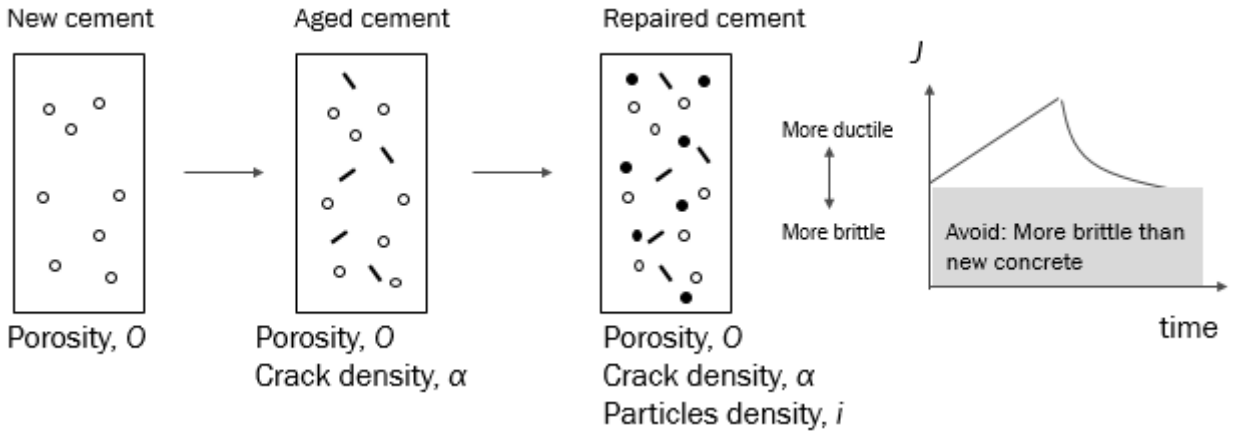

Figure 7.3. New, aged and fixed concrete behavior after adding particles

Based on the results obtained from the analytical and experiment analysis, it was concluded that:

- The formulas derived in Chapter 4 can be applied to accurately predict trends in cement behavior.
- By adding nanoparticles into the network to seal leaks, it is expected that the cracks would be sealed but at the same time the fracture parameter *J* integral will decreases with time.

7.2.4 EXTEND FORMULA CONSIDERING SPATIAL ARRANGEMENT OF MICROSTRUCTURE

In chapter 6, we introduced jamming and unjamming effects in the inclusion system to characterize fracture interaction with inclusions. We show that as the system moves to its lowest energy, it becomes more stable and rigid. Per this definition, in an unjammed heterogeneous material with low volume fraction of particles and at a certain stage of stress, the particles are free to explore different arrangement within the system. This will encourage cracks to propagate. The analysis was performed using theoretical and numerical analysis for the three-point bending specimen.

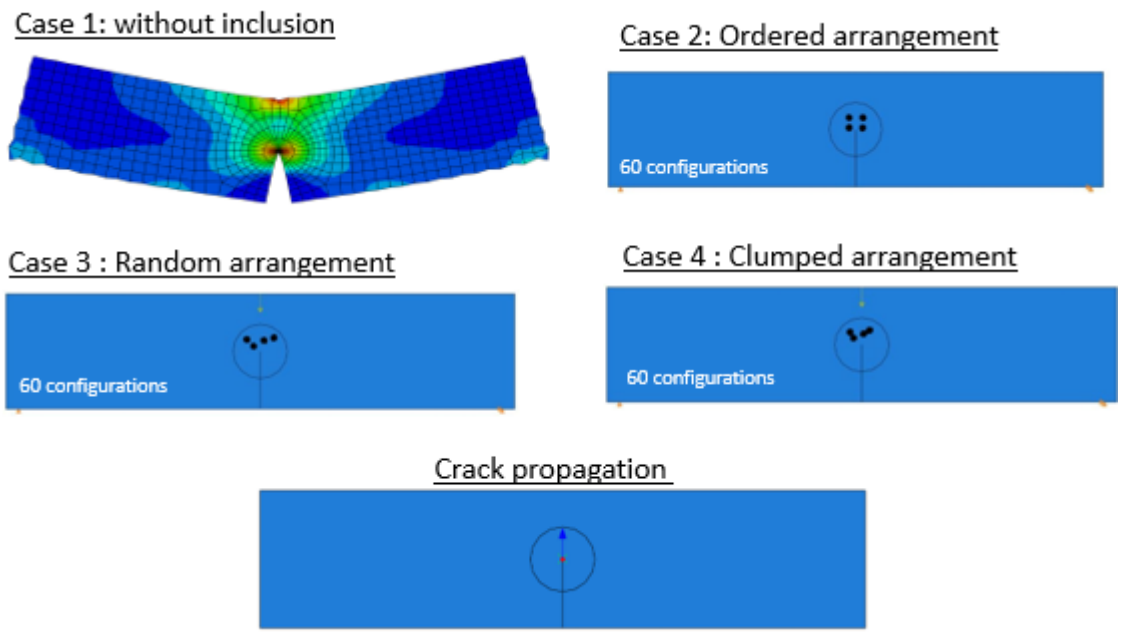

Figure 7.4. Considering particle jamming effect on the fracture toughness

Based on the results obtained from the analytical and numerical analysis, it was concluded that:

1. There is good agreement between the theoretical and the numerical analysis based on the SIF values for different particle configurations, so closed form equations can be used to make design considerations of inclusions.
2. The translational order parameter can be used as a quantifier of inclusion arrangement to capture the trend of fracture toughness of a material.
3. The remaining discrepancy in experimental results between micro- and macro-scale fracture tests could be attributed to the effect of inclusion arrangement. The difference between fracture toughness between ordered and random systems is exactly 0.5 MPa$\sqrt{m}$.

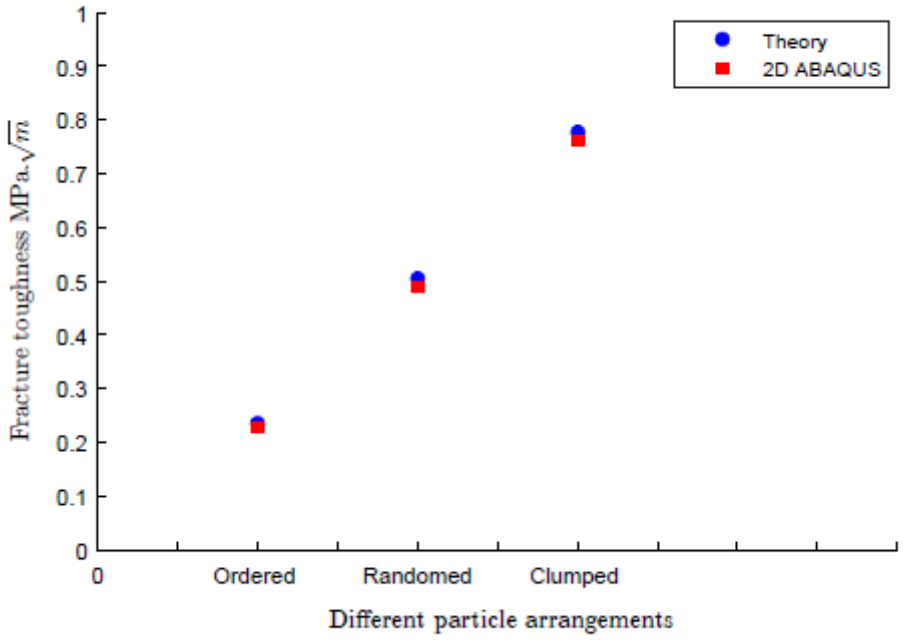

Figure 7.5. Theoretical and numerical agreement based on the fracture toughness values

REFERENCES

[1] Bažant ZP, Planas J. 1998. Fracture and size effect in concrete and other quasibrittle materials. Boca raton, FL: CRC Press .pp7-22.

[2] Kachanov, M.1997. Stress concentrations and micro-fracturing patterns in a brittle-elastic solid with interacting pores of diverse shapes. International journal of solids and structures, volume 34, Issue 22. 2887-2904.

[3] Gross, D., Seelig, T. 2006. Fracture mechanics with an introduction to micromechanics. Springer-verlag berlin heidelberg, pp.218-287.

[4] Mehta, P. Kumar. 1986. Concrete structure, properties and materials. Prentice-Hill, Inc.

[5] Akono, AT. 2013. Assessment of fracture properties and rate effects on fracture of materials by micro scratching application to gas shale. PhD dissertation, Massachusetts institute of technology. pp. 23-50.

[6] FHWA. 2011. Bridges by posting status, Federal highway administration, Washington, DC.

[7] McAllister, T. 2013. National institute of standards and technology technical note 1795, developing guidelines and standards for disaster resilience of the built environment, Engineering laboratory materials and structural systems.

[8] Johnson, G. R. and Stryk, R. A. 1987. "Eroding interface and improved tetrahedral element algorithms for high-velocity impact computations in three dimensions," International journal of impact engineering, vol. 5, no. 1–4, pp. 411–421.

[9] Belytschko, T. and Lin, J. I. 1987. "A three-dimensional impact penetration algorithm with erosion," International journal of impact engineering, vol. 5, no. 1–4, pp. 111–127.

[10] Beissel, S. R. Johnson, G. R. and Popelar, C. H. 1998. "An element failure algorithm for dynamic crack propagation in general directions," Engineering fracture mechanics, vol. 61, no. 3-4, pp. 407–425.

[11] Fan, R. and Fish, J. 2008. "The rs-method for material failure simulations," International journal for numerical methods in engineering, vol. 73, no. 11, pp. 1607–1623.

[12] Lee, J., and Yee, A.F. 2000. "Fracture of glass bead/epoxy composites: on micro- mechanical deformations." Polymer 41. pp 8363-8373.

[13] Wouterson, E., Freddy Y.C.B., Hu, X. and Wong, S. 2005. "Specific properties and fracture toughness of syntactic foam: Effect of foam microstructures." Composites science and technology 65. pp 1840-1850.

[14] Sanchez-Soto, M. Pages, P. Lacort, T. and Briceno K. 2007. Curing FTIR study and mechanical characterization of glass filled trifunctional epoxy composites. Composites science and technology 67. pp 1974-1985.

[15] Kouznetsova, V. Brekelmans, W. A. M. and Baaijens, F. P. T. 2001. An approach to micro-macro modeling of heterogeneous materials. Computational mechanics 27. pp 37-48.

[16] Nguyen, V. Lioberas-Valls, O., Stroeven, M. and Johannes, L. 2011. Homogenization-based multiscale crack modeling: from micro-diffusive damage to macro-cracks. Computational methods application of mechanics 200. pp 1220-1236.

[17] Hori, M. and Nemat-Nasser, S. (1999). On two micromechanics theories for determining micro-macro relations in heterogenous solids. Mechanics of materials 31. pp 667-682.

[18] Lamon J. 2016. Brittle fracture and damage of brittle materials and composites. ISTE Press Ltd and elsevier Ltd. pp. 1-33.

[19] Lemaitre, J. 1992. A course on damage mechanics. Spring-Verlag New York. pp. 11-37.

[20] Akono, A.T., Randall, N.X., Ulm, F. J. E. 2012. Experimental determination of fracture toughness via micros scratch tests: Application to polymers, ceramics and metals. Materials research society. Vol. 27, No. 2. pp. 485-493.

[21] Anderson, T.L. 2005. Fracture Mechanics fundamentals and applications. pp. 103-168.

[22] Erwin M. Wouterson, Freddy Y.C. Boey, Xiao Hu, Shing-Chung Wong. 2005. "Specific properties and fracture toughness of syntactic foam: Effect of foam microstructures." Composites science and technology 65. pp 1840-1850.

[23] Bengisu, M. 2001. Engineering ceramics. Spring-Verlag Berlin Heidelberg.

[24] Gouda, P.S.S., Kudari, S.K., Prabhuswamy, S. 2011. Fracture toughness of glass carbon (0/90) s fiber reinforced polymer composite-An experimental and numerical study. Journal of minerals and materials characterization & engineering. Vol. 10, No.8, pp. 671-682.

[25] Otsu, N. 1979. A threshold selection method from gray-level histograms. IEEE transaction on systems. Man, and cybernetics. Vol. 9. pp. 62-66.

[26] Wouterson E.M., Boey F.Y.C., Wong, S.C. 2005. Specific properties and fracture toughness of syntactic foam: Effect of foam microstructures. Composites science and Technology. Vol.65. pp.1840-1850.

[27] Sanchez-Soto M., Pages P., Lacort T., Briceno K. 2007. Curing FTIR study and mechanical characterization of glass filled trifunctional epoxy composites. Composites science and Technology. Vol.67. pp. 1974-1985.

[28] Vecchio K.S., Jiang F. 2016. Fracture toughness of Ceramic-Fiber-Reinforced Metallic-Intermetallic-Laminate (CFR-MIL) composites. Materials Science and Engineering. A 649. pp. 407-416.

[29] Inglis, C.E. 1913. Stresses in a plates due to the presence of cracks and sharp corners. Transactions of the Institute of Naval Architects. Vol. 55, pp. 219-241.

[30] Anderson, T. 2005. Fracture Mechanics Fundamentals and Applications. Third edition. Taylor and Francis Group.

[31] Sanford, R.J. 2003. Principles of fracture mechanics. Pearson Education, Inc.pp. 92-96.

[32] Griffith, A.A. 1921.The phenomena of rupture and flow in solids. Phil. trans. roy. soc. London, A221:163-197.

[33] Irwin, G.R. 1957. Analysis of stress and strain near the end of a crack traversing a plate. Journal of Applied Mechanics. Volume 4. pp.361-364.

[34] Westergaard, H.M. 1939. Bearing pressure and cracks. Journal of applied mechanics. Vol.6. A49-53.

[35] Boresi A., Schmidt R. 2002. Advanced mechanics of materials. John Wiley & Sons, Inc 6th edition. pp.80-90.

[36] Rice, J.R. 1974. Limitations to the small scale yielding approximation for crack tip plasticity. Journal of the mechanics and physics of solids. Vol.22. pp.17-26.

[37] Rice, J.R. 1968. A Path Independent Integral and the Approximate Analysis of Strain Concentration by Notches and Cracks. Journal of applied mechanics. pp. 379-386.

[38] Anon. 2003. Standard Test Method for Tensile Properties of Plastics, ASTM International, ASTM D638-14West Conshohocken, PA.

[39] Hubler, M.H., Ulm, F. J.2016. Size-effect law for scratch tests of axisymmetric shape. Journal of engineering mechanics. Vol.142, no. 12 04016094-1-11.

[40] Akono, A.T., Ulm, F. J. E. 2014. An improved technique for characterizing the fracture toughness via scratch test experiments. Wear. Vol. 313. pp. 117-124.

[41] Cherepanov AG, Cherepanov GP. 1990.Cutting resistance of rocks. Strength material. Vol.22. pp.1626–45.

[42] Qian, X., Yang, W. 2010. A hybrid approach to determine fracture resistance for mode I and mixed-mode I and II fracture specimens. Fatigue and Fracture of Engineering Materials & Structures. Vol.34. pp.305-320.

[43] Kasavajhala, A.R.M., Gu, L. 2011. Fracture analysis of Kevlar-49/epoxy and e-glass/epoxy doublers for reinforcement of cracked aluminum plates. Composite Structures. pp. 1-6.

[44] Pook, L. P., Campagnolo, A., Berto, F., Lazzarin, P. 2015. Coupled fracture mode of a cracked plate under anti-plane loading. Engineering Fracture Mechanics. Vol. 134. pp. 391-403.

[45] Bard, R. 2008. Analysis of the scratch test for cohessive-frictional materials. PhD dissertation, Massachusetts Institute of Technology.

[46] Xie, Z.-H. Munroe, P.R., Moon, R.J., Hoffman, M. 2003. Characterization of surface contact-induced fracture in ceramics using a focused ion beam miller. Wear Vol. 255. pp. 651–656.

[47] Eshelby J. D. 1957.The determination of the elastic field of an ellipsoidal inclusion, and related problems. Proc Roy Soc Lon. pp. 376-96.

[48] Li H., Yang J., Li Z. 2014. An approximation solution for the plane stress mode I crack interacting with an inclusion of arbitrary shape. Engineering Fracture Mechanics. Vol. 116. pp. 190-196.

[49] Li, Z., Chen Q. 2003. Some simple formulas to predict the variation of stress intensity factors for mode I crack induced by near crack-tip inclusion. Engineering Fracture Mechanics. Vol.70, pp. 581-587.

[50] Kachanov M., Tsukrov I. and Shafiro B. 1994. Effective Moduli of solids with cavities of various shapes. Applied Mechanics Research. Vol.47, no.1. pp. S151-S174.

[51] Atluri S.N., Nakagaki M., Chen W.H. 1977. Flaw Growth and Fracture. STP 631. American Society for Testing and Materials. Philadelphia. pp. 376-96.

[52] Chen W.H., Huang Y.H. 1979. On the J-integral for cracked structure with inclusions. International Journal of Fracture. Vol. 15, Issue 2, pp. R73-R76.

[53] Jajam K.C., Tippur H.V. 2011. An experimental investigation of dynamic crack growth past a stiff inclusion. Engineering fracture mechanics. Vol. 78, pp. 1289-1305.

[54] Karchanov M. 1993. Elastic solids with many cracks and related problems. Advanced applied mechanics. Vol. 30, pp. 259-445.

[55] Johnson, C.V. Chen, J. Hasparyk, N.P. Monteiro, P.J.M. Akono, A.T. 2017. Fracture properties of the alkali silicate gel using microscopic scratch testing. Cement and Concrete Composites. Vol. 79. pp.71-75

[56] Akono, A.T. Bouché, G. A. 2016. Rebuttal: Shallow and deep scratch tests as powerful alternatives to assess the fracture properties of quasi-brittle materials. Engineering Fracture Mechanics. Vol. 158. pp. 23–38.

[57] Akono, A.T. Kabir, P. 2016. Microscopic fracture characterization of gas shale via scratch testing. Mechanics Research Communications. Vol. 78. Pp. 86–92.

[58] Abaqus 6.12. Getting started with Abaqus. Dassault Systemes Simulia Corp., Providence, RI, USA.

[59] Shih, C. F., Moran, B. and Nakamura, T. 1986.Energy Release Rate along a Three-Dimensional Crack Front in a Thermally Stressed Body. International Journal of Fracture. Vol. 30, pp. 79–102.

[60] Barsoum, R.S. 1977. International Journal for Numerical Methods in Engineering. pp. 85-98.

[61] Hussain, M.A. Shih, C.F. and German, M.D. 1980. Lagrangian Elements as Singularity Elements in Crack Analysis. General Electric Company, Technical Information Series Report No. 80CRD291.

[62] Anon.2012. Standard test method for Linear-Elastic Plain-Strain Fracture Toughness KIC of Metallic Materials. ASTM E399-12. New York.

[63] Lawn B.R. 1966. Partial cone crack formation in a brittle material loaded with a sliding spherical indenter. Proceedings of the Royal Society. Series A, Mathematical and Physical Sciences. Vol. 299, pp. 307-315.

[64] Swain M.V. 1979. Microfracture about scratches in brittle solids. Proceedings of the Royal Society. Series A, Mathematical and Physical Sciences. Vol 366, pp. 575-597.

[65] Li M., Zhou J., Lau A., Low S. 2002. Self-Similarity Simplification Approaches for the modeling and Analysis of Rockwell Hardness Indentation. Journal of Research of the National Institute of Standards and Technology. Vol. 107, No. 5, pp. 401-412.

[66] Briscoe, B. J. Evans P. D. Pelillo, E. Sinha, S.K. 1996. Scratching maps for polymers. Wear Vol. 200, pp. 137-147.

[67] Williams J.A. 1996. Analytical models of scratch hardness. Tribology International. Vol. 29, pp. 675-694.

[68] Torquato, S. 2002. Random heterogeneous materials: microstructure and macroscopic properties. Springer-Verlag New York, Inc. pp. 59-70.

[69] Paola, M. D. Pirrotta, A. Valenza, A. 2011. Visco-elastic behavior through fractional calculus: An easier method for best fitting experimental results. Mechanics of Materials. Vol. 43. pp.799–806.

[70] Barenblatt G.I, 1962. The Mathematical theory of equilibrium cracks in brittle fracture. advances in applied mechanics. Vol. VII, Academic Press. pp. 55-129.

[71] Wells A.A. 1958. The dynamic stress distribution surrounding a running crack-A photo-elastic analysis. Proceedings of the society for experimental stress analysis. Vol. 16. pp. 69-92.

[72] Atluri S.N., Nakagaki M., Chen W.H. 1977. Flaw Growth and Fracture. STP 631. American Society for Testing and Materials. Philadelphia. pp. 376-96.

[73] McMeeking, R.M. and Evans, A.G. 1982. Mechanics of transformation toughening in brittle materials. Journal of the American Ceramic Society. 242-246.

[74] Jajam K.C., Tippur H.V. 2011. An experimental investigation of dynamic crack growth past a stiff inclusion. Engineering fracture mechanics. Vol. 78. pp. 1289-1305.

[75] Al Wakeel S., Hubler M. 2016. Experimental and theoretical investigation of the fracture behavior of glass beads/epoxy composites using microscratching. 9th International Conference of Fracture Mechanics of Concrete and Concrete Structures. pp. 1-11.

[76] Akono T. A. Ulm, F. J. 2011. Scratch test model for the determination of fracture toughness. Engineering Fracture Mechanics. Vol. 78. pp. 334-342.

[77] Akono T. A. Ulm, F. J. 2011. Scratching as a fracture process from butter to steel. Physical Review Letters. Vol. 106(20). pp. 204302-1 204302-4.

[78] ASM Handbooks, volume 1 and 2, Engineered Materials Handbook: Nonferrous Alloys and Pure Metals, Vol. 146, no.4.

[79] Anon. 2012. ASTM D2734. Standard Test Methods for Void Content of Reinforced Plastics.

[80] Xu, X.F, Stefanou, G., 2011. Variational formulation on effective elastic moduli of randomly cracked solids. Multiscal Computational Engineering. Vol.9. pp. 347-363.

[81] V. A. Lubarda, V.A., Krajcinovic, D. 1993. Damage tensors and the crack density distribution. Journal of solids structures, vol. 30. Number 20. pp. 285-2877.

[82] Naebe, M., Abolhasani, M., Khayyam, H., Amini, A., Fox, B. 2016. Crack damage in polymers and Composites: A Review, Polymer reviews, vol.56. pp. 31-69.

[83] Peretz, D. 1972. Crack propagation in polymeric composites. Engineering fracture mechanics, vol. 4. pp. 979-990.

[84] Awaja, F., Nguyen, M., Zhang, S., Arhatari, B. 2011. The investigation of inner structural damage of UV and heat degraded polymer composites using X-ray micro CT. Composites: Part A. Vol.42. pp. 408-418.

[85] Muskhelishvili N.I. 1953. Some basic problems of mathematical theory of elasticity. P. Noordhoff, Groningen, The Netherlands.

[86] Paris P.C, Sih G.C. 1965. Stress analysis of cracks. ASTM STP. pp. 30-81.

[87] Goodier J.N. 1969. Mathematical theory of equilibrium of cracks. In fracture II, New York: Academic Press. pp. 2-67.

[88] Eftis J, Liebowitz H. 1972. On the modified Westergaard equations for certain plane crack problems. International Journal of Fracture Mechanics. Vol.8. pp. 383-392.

[89] Budiansky B, Hutchinson JW, Lambropoulos JC. 1983. Continuum theory of dilatant transformation toughening in ceramics. International Journal Solids Structure. Vol. 19, No. 4. pp.337–355.

[90] NSTC 2007. The National Nanotechnology Initiative – Strategic Plan, December 2007. Executive Office of the President of the United States.

[91] Sanchez, F., and Soboley, K. 2010. Nanotechnology in concrete – A review. Construction and Building Materials. Vol.24. pp.2060-2071.

[92] Singh, L.P., Karade, S.R., Bhattacharyya, S.K., Yousuf, M.M., Ahalawat, S. 2013. Beneficial role of nano-silica in cement based materials. Construction and Building Materials. Vol. 47. pp. 1069-1077.

[92] Nygaard, R. 2010. Well Design and Well Integrity. Energy and environmental systems group, ISEEE.

[93] Zhang, A., Weissinger, J., Emily Peethamparan, S., and Scherer, and George W. 2010. Early Hydration and setting of oil well cement. Cement and concrete research. Vol. 40. pp. 1023-1033.

[94] Celia, M.A., Bachu, S., Nordbotten, J.M., Gasda, S., and Dahle, H.K. 2004. Quantitative estimation of CO_2 leakage from geological storage: Analytical models, numerical models, and data needs. In Proceedings of 7th International Conference on Greenhouse Gas Control Technologies.

[95] Li, H., Zhang, M-h., and Ou, J-p. 2007. Flexural fatigue performance of concrete containing nano-particles for pavement. International journal fatigue. Vol. 29(7). pp.1292–301.

[96] Jo, B. W., Kim, C. H., Tae, G. H., & Park, J. B. 2007. Characteristics of cement mortar with nano-SiO_2 particles. Construction and building materials. Vol. 21. pp. 1351–1355.

[97] API 10A 2011. Specification for cements and materials for well cementing.

[98] Halliburton 2009. www.halliburton.com.

[99] Meyer 2008. Summary of carbon dioxide enhanced oil recovery (CO2 EOR) injection well technology. API special reports, 62.

[100] Schlumberger (2009). www.slb.com.

[101] Anon, ASTM C830. 2016. Apparent Porosity, Liquid Absorption, Apparent specific gravity and bulk density of refractory shapes by vacuum pressure.

[102] Anon, ASTM C1202 .2012. Standard test Method for electrical indication of concrete's ability to resist chloride ion penetration.

[103] Torquate, S. 2010. Jammed hard-particle packing: From Kepler to Bernal and beyond. FH Stillinger. pp. 1-12.

[104] Liu A. J. and Nagel, S. R. 1998. Jamming. Department of physics & astronomy university of Pennsylvania. Nature.

[105] Luis A.A. 2005. Computer simulation methods in chemistry and physics. pp. 59-70.

[106] Chen, W., Hung, Y. 1979. On the J-integral for cracked structure with inclusions. Journal of fracture. Vol.15. pp. R73-R76.

APPENDIX A

In this appendix, we show the related material mentioned in chapter 3. Including the raw data for the scratch test, the mathematical simulation used to interpret the experimental results and predict the behavior of the composite during the scratch test and the Matlab code used to generate random probability distributions for different population of particles (pixels) to calculate the radial distribution function.

A.1 RAW DATA FOR THE SCRATCH TEST

A.1.1 SUMMARY OF THE SCRATCH CURVES FOR SPECIMEN WITH 0% GLASS BEADS

Scratch test was used to measure the horizontal force with the penetration depth by dragging a probe on the polymer surface as explained in chapter 3. Figure A.1 illustrate all the scratches that have been made on specimen with 0% glass beads.

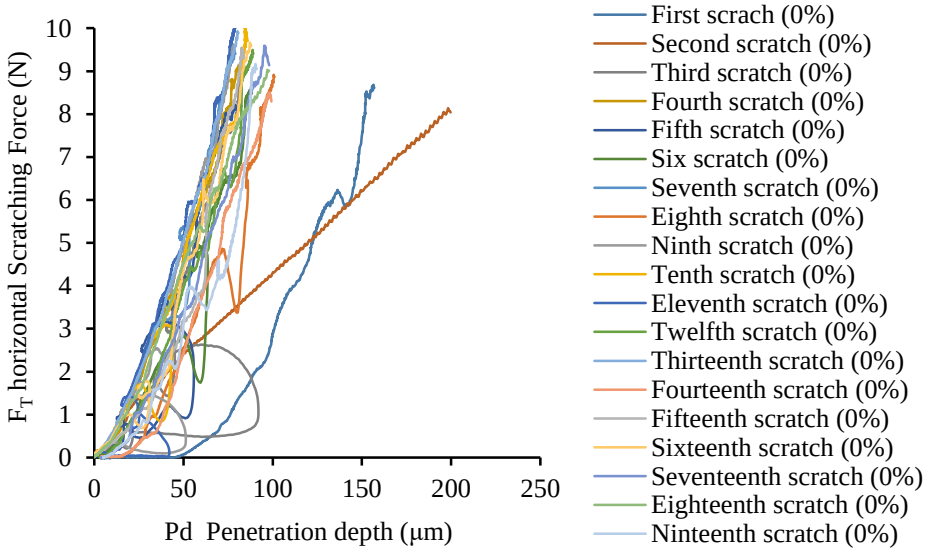

Figure A.1.1. Relation between Horizontal Scratching Force and the Penetration depth for specimen with 0% glass beads using the scratch test

A.1.2 SUMMARY OF THE SCRATCH CURVES FOR SPECIMEN WITH 5% GLASS BEADS

Figure A.2 illustrate all the scratches that have been made on specimen with 5% glass beads.

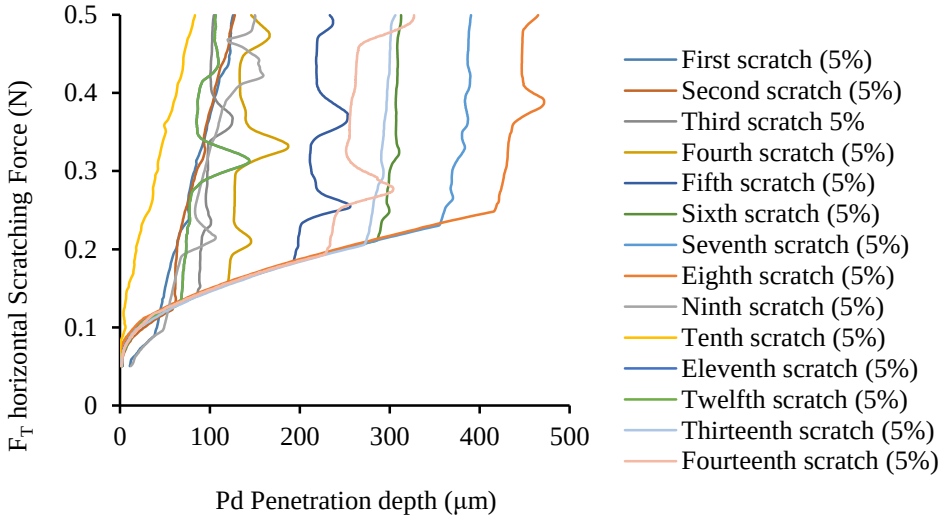

Figure A.1.2. Relation between Horizontal Scratching Force and the Penetration depth for specimen with 5% glass beads using the scratch test

A.1.3 SUMMARY OF THE SCRATCH CURVES FOR SPECIMEN WITH 25% GLASS BEADS

Figure A.3 illustrate all the scratches that have been made on specimen with 25% glass beads.

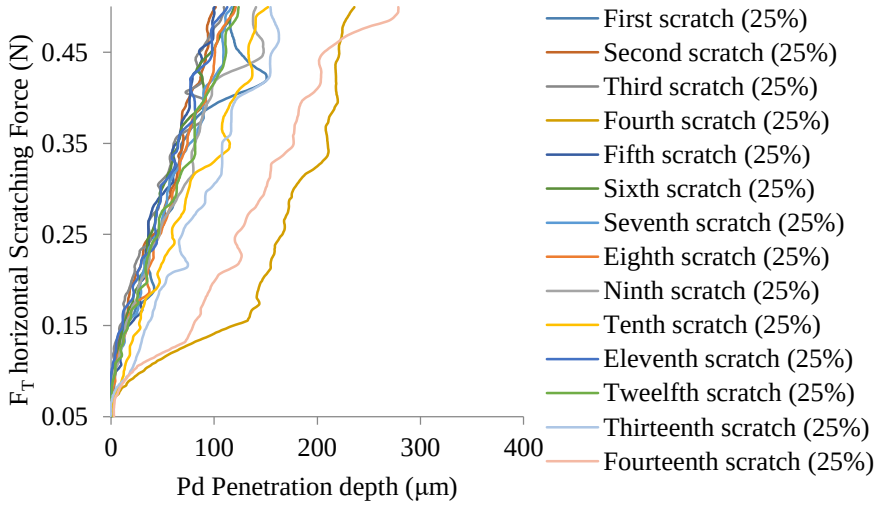

Figure A.1.3. Relation between Horizontal Scratching Force and the Penetration depth for specimen with 25% glass beads using the scratch test

A.1.4 SUMMARY OF THE SCRATCH CURVES FOR SPECIMEN WITH 50% GLASS BEADS

Figure A.4 illustrate all the scratches that have been made on specimen with 50% glass beads.

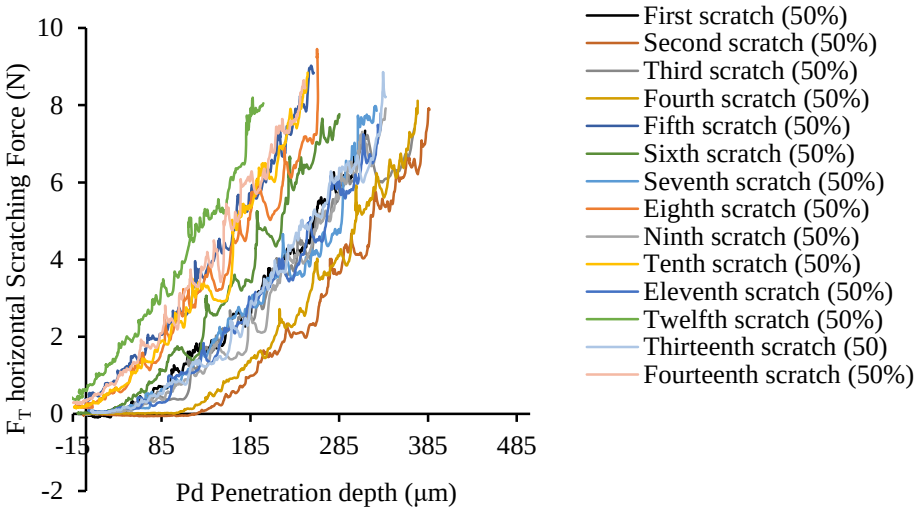

Figure A.1.4. Relation between Horizontal Scratching Force and the Penetration depth for specimen with 50% glass beads using the scratch test

A.2 PANORAMA IMAGES FOR THE SCRATCHES DURING THE SCRATCH TEST

A.2.1 PANORAMA IMAGES OF ALL THE SCRATCHES FOR 50% INCLUSION SPECIMEN

Scratch # 1 (50% glass beads)

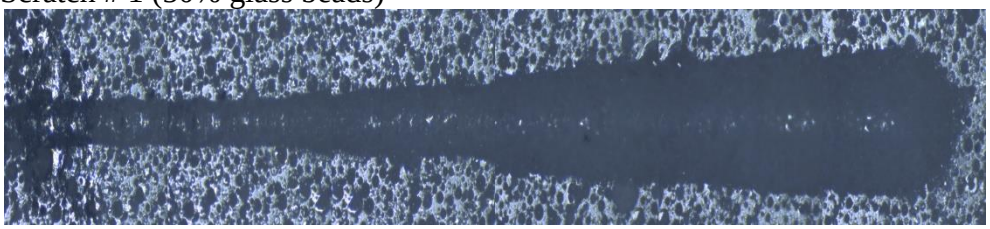

Scratch # 2 (50% glass beads)

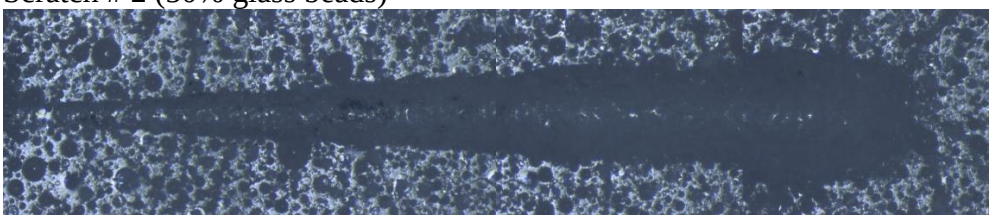

Scratch # 3 (50% glass beads)

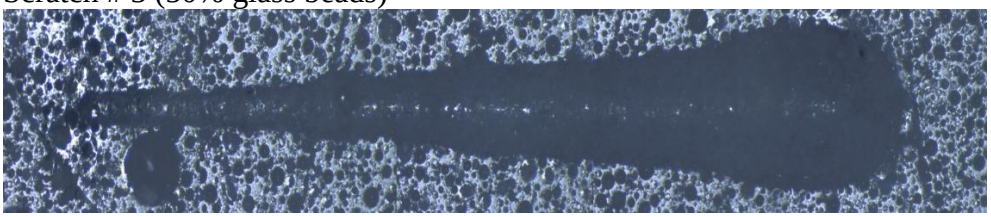

Scratch # 4 (50% glass beads)

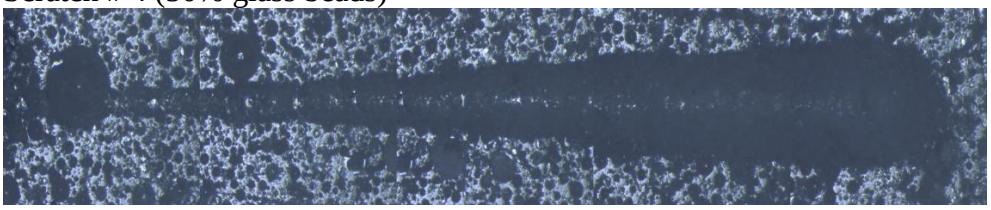

Scratch # 5 (50% glass beads)

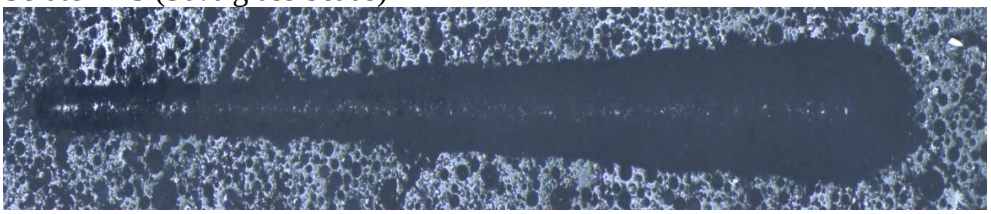

Scratch # 6 (50% glass beads)

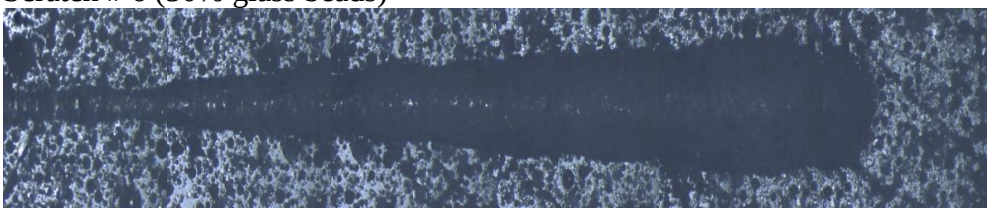

Scratch # 7 (50% glass beads)

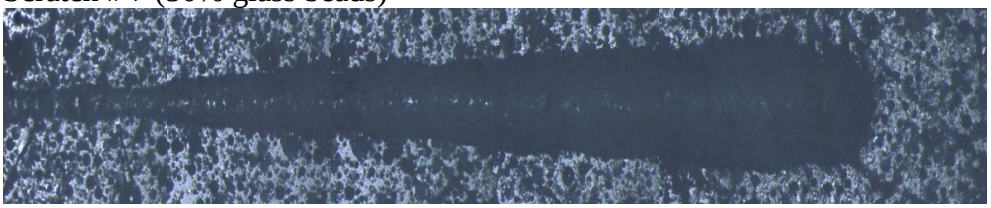

Scratch # 8 (50% glass beads)

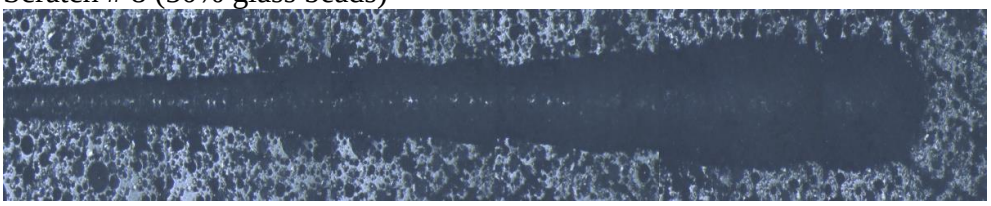

Scratch # 9 (50% glass beads)

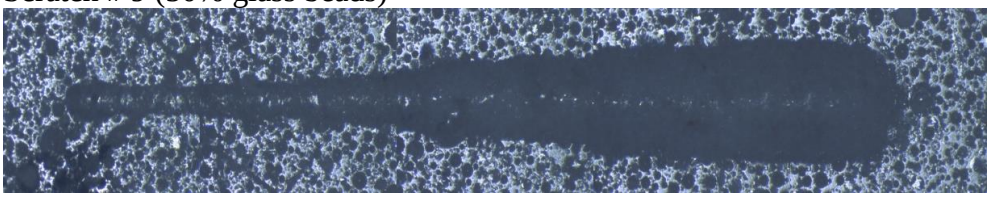

Scratch # 10 (50% glass beads)

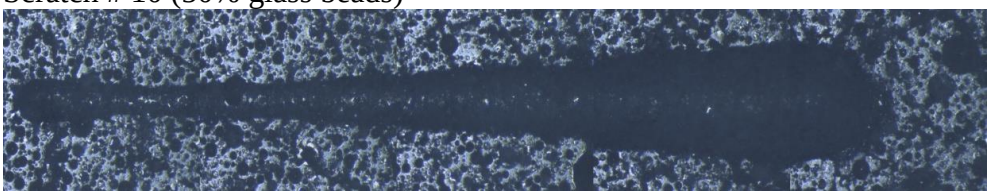

Scratch # 11 (50% glass beads)

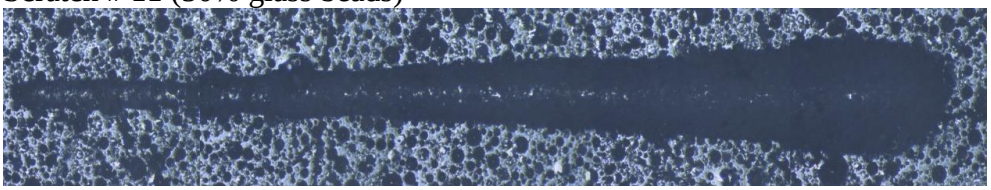

Scratch # 12 (50% glass beads)

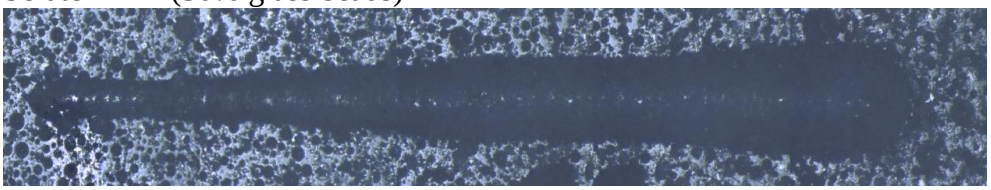

Scratch # 13 (50% glass beads)

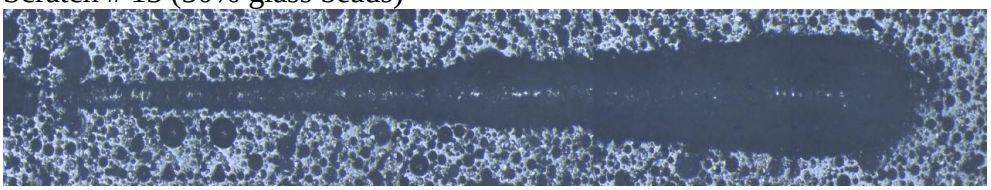

Scratch # 14 (50% glass beads)

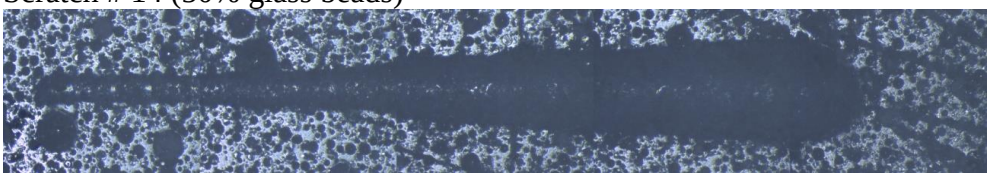

A.2.2 PANORAMA IMAGES OF ALL THE SCRATCHES FOR 25% INCLUSION SPECIMEN

Scratch # 1 (25% glass beads)

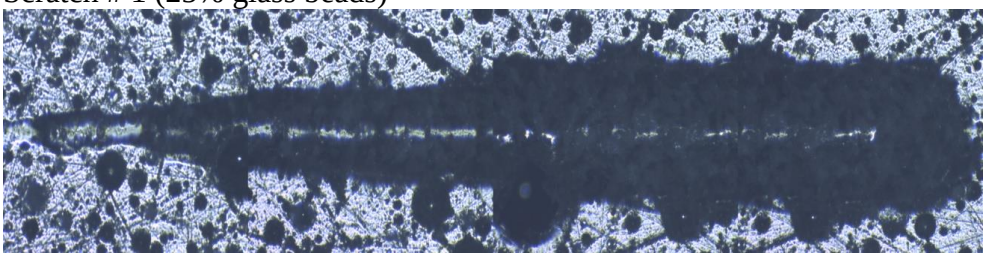

Scratch # 2 (25% glass beads)

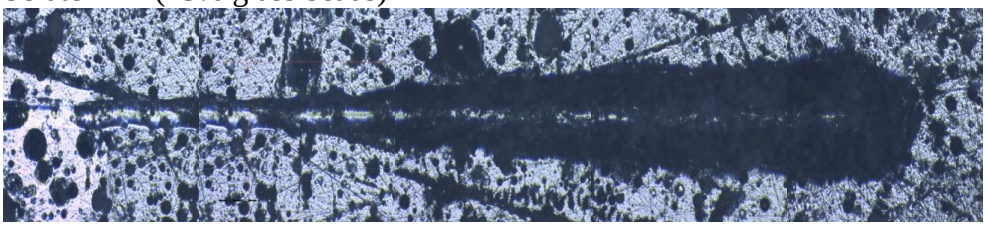

Scratch # 3 (25% glass beads)

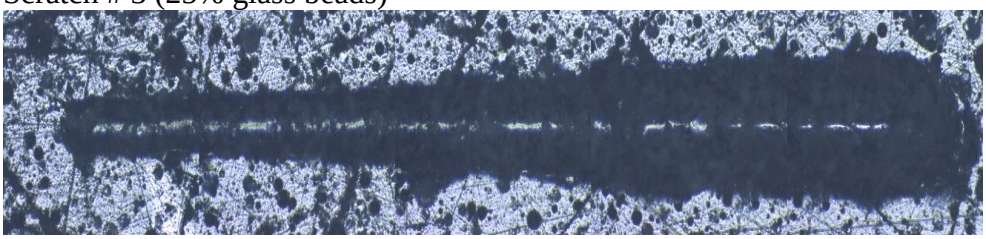

Scratch # 4 (25% glass beads)

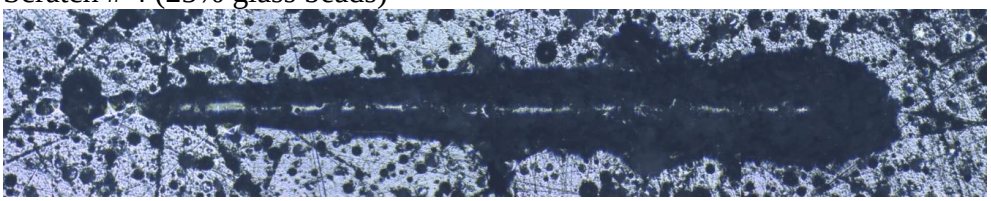

Scratch # 5 (25% glass beads)

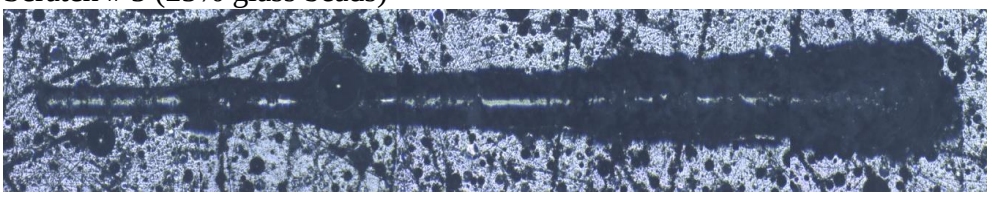

Scratch # 6 (25% glass beads)

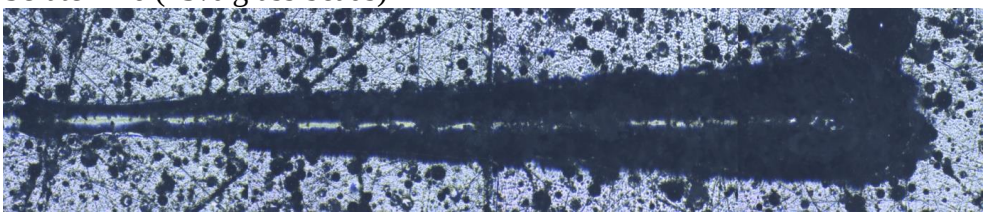

Scratch # 7 (25% glass beads)

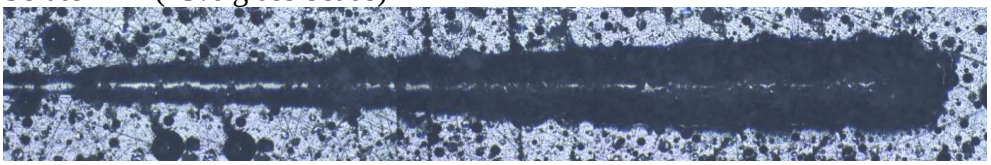

Scratch # 8 (25% glass beads)

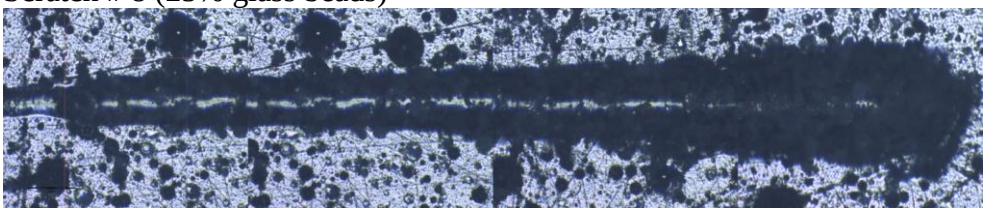

Scratch # 9 (25% glass beads)

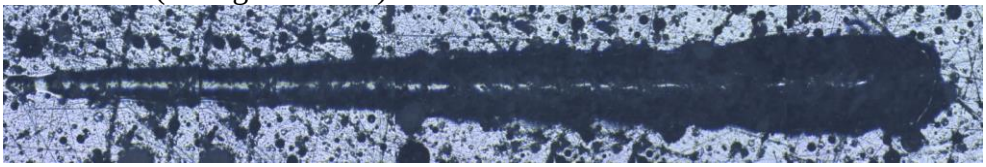

Scratch # 10 (25% glass beads)

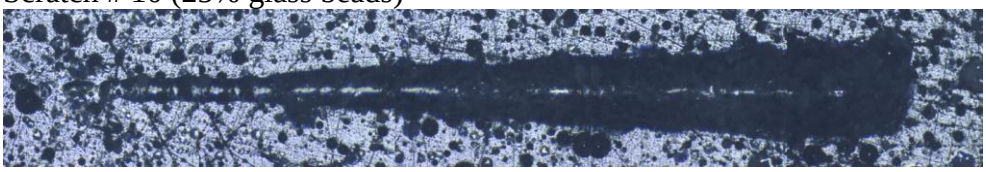

Scratch # 11 (25% glass beads)

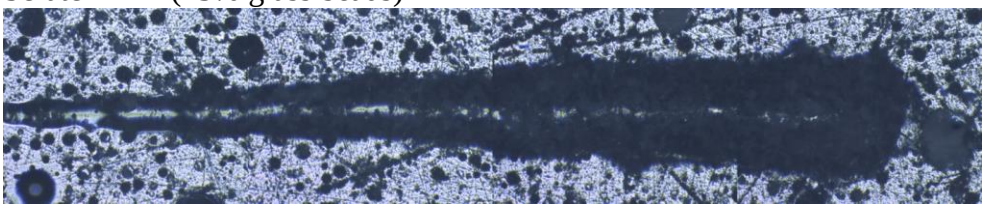

Scratch # 12 (25% glass beads)

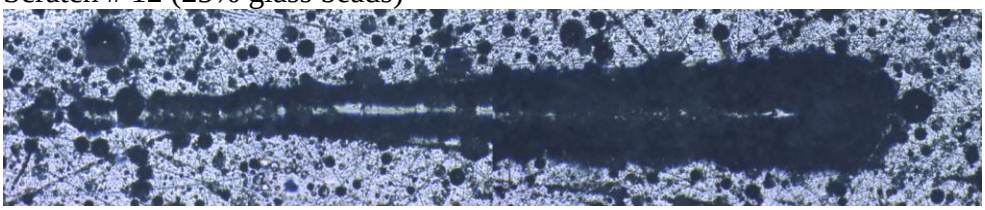

Scratch # 13 (25% glass beads)

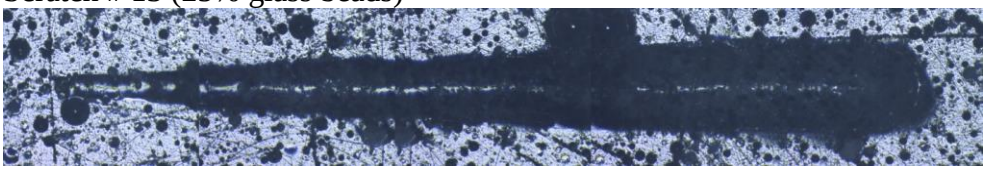

Scratch # 14 (25% glass beads)

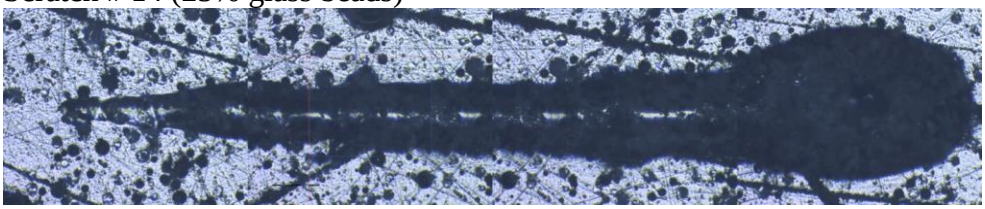

A.2.3 PANORAMA IMAGES OF ALL THE SCRATCHES FOR 5% INCLUSION SPECIMEN

Scratch #1 (5% glass beads)

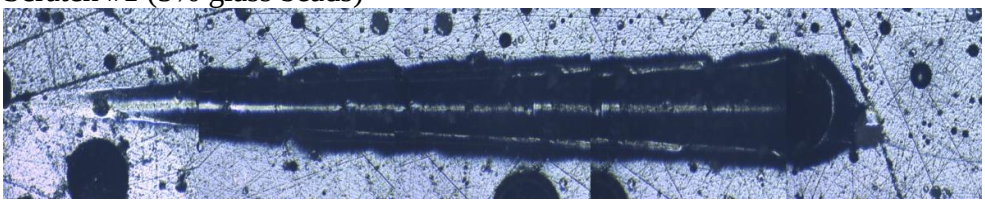

Scratch # 2 (5% glass beads)

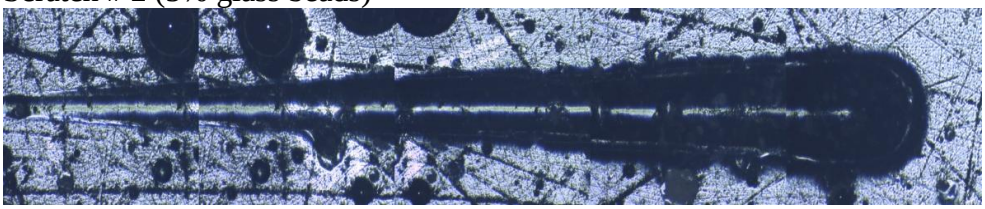

Scratch # 3 (5% glass beads)

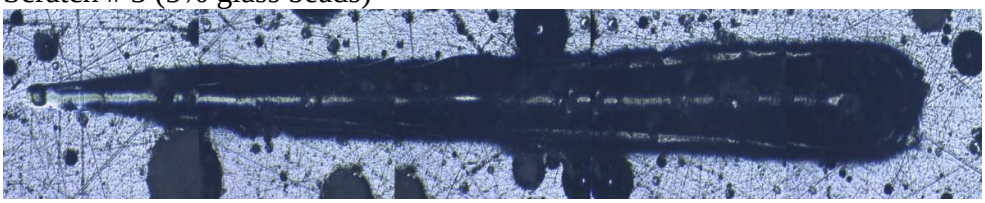

Scratch # 4 (5% glass beads)

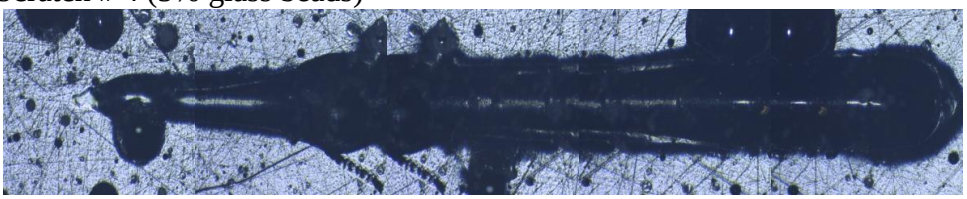

Scratch # 5 (5% glass beads)

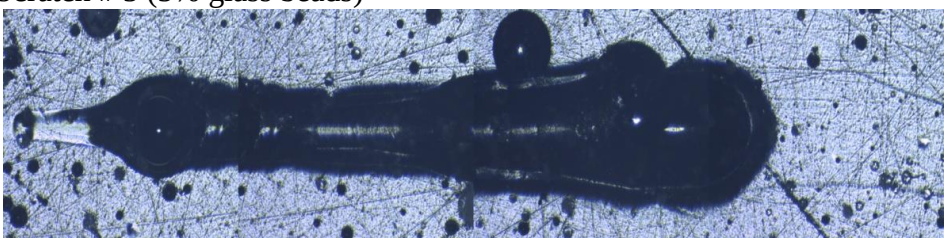

Scratch # 6 (5% glass beads)

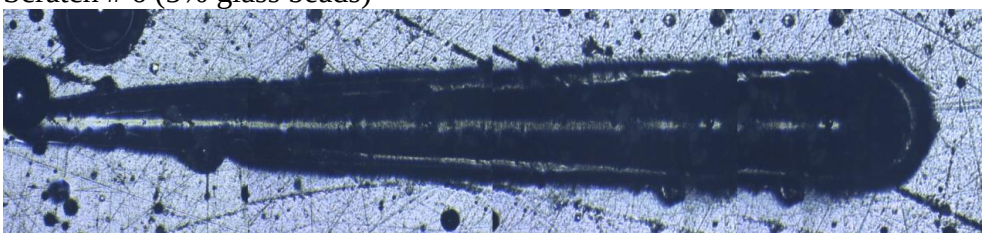

Scratch # 7 (5% glass beads)

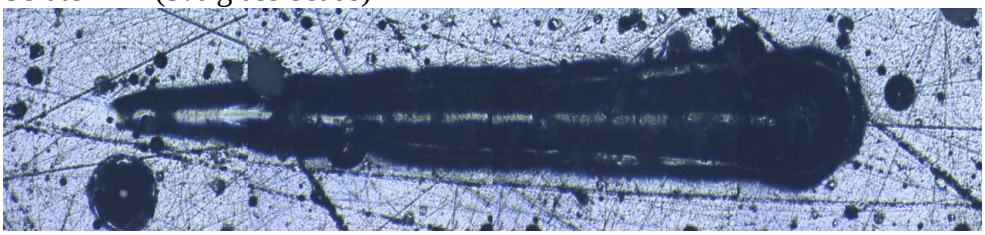

Scratch # 8 (5% glass beads)

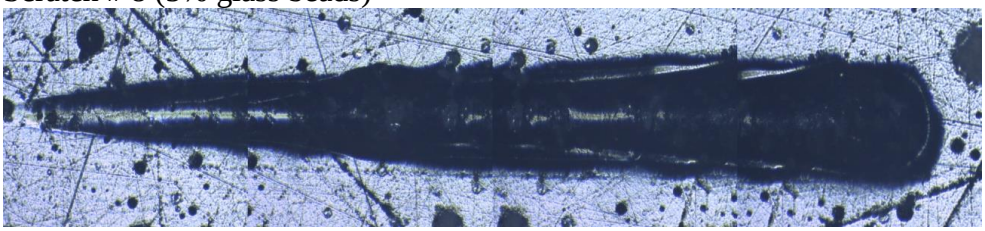

Scratch # 9 (5% glass beads)

Scratch # 10 (5% glass beads)

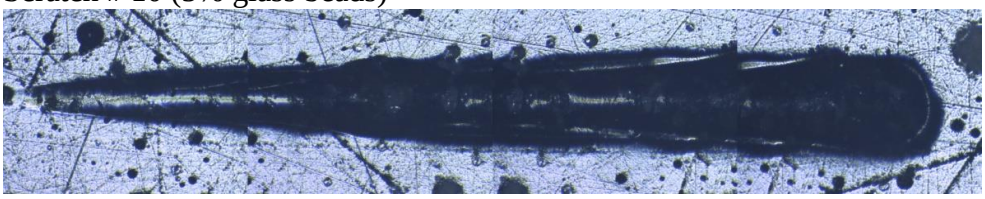

Scratch # 11 (5% glass beads)

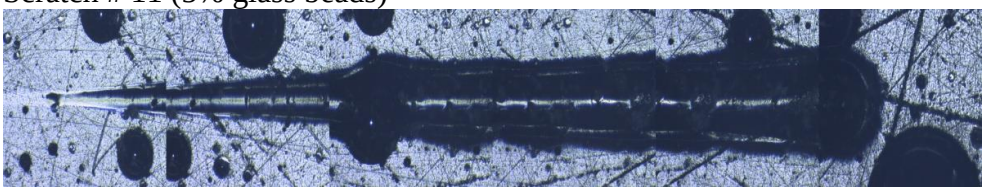

Scratch # 12 (5% glass beads)

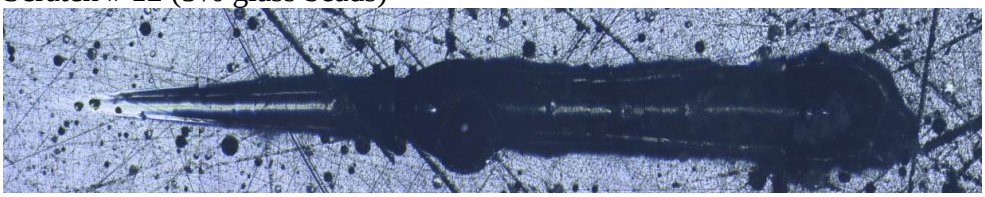

Scratch # 13 (5% glass beads)

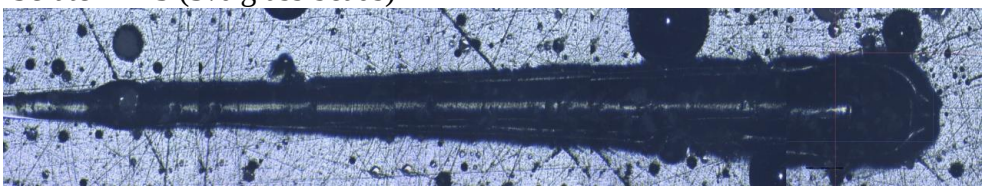

Scratch # 14 (5% glass beads)

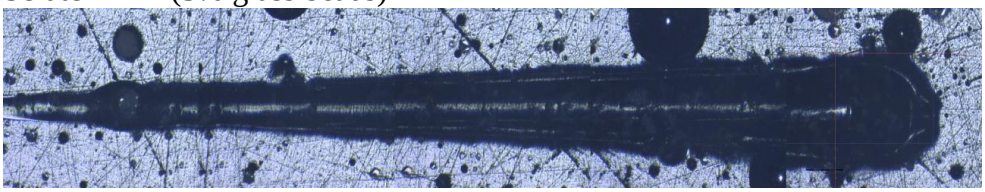

Scratch # 15 (5% glass beads)

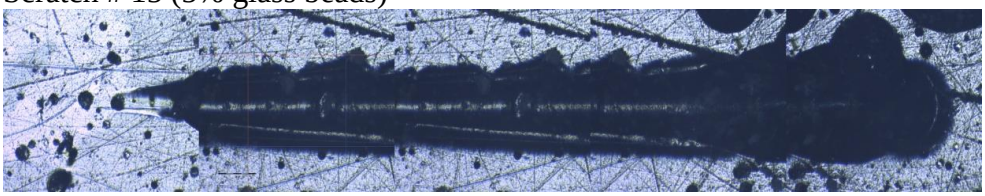

A.2.4 PANORAMA IMAGES OF ALL THE SCRATCHES FOR 0% INCLUSION SPECIMEN

Scratch #1 (0% glass beads)

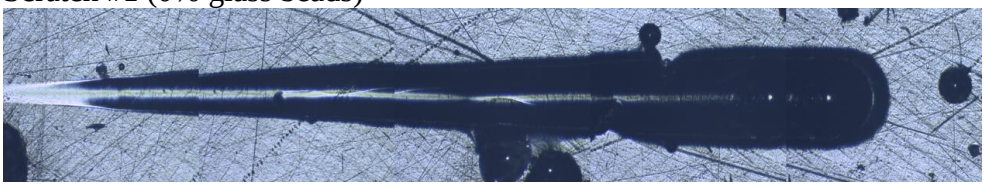

Scratch #2 (0% glass beads)

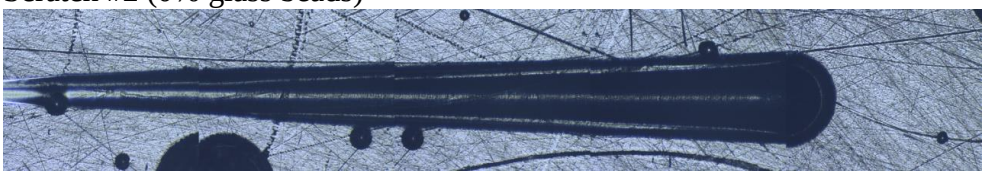

Scratch # 3 (0% glass beads)

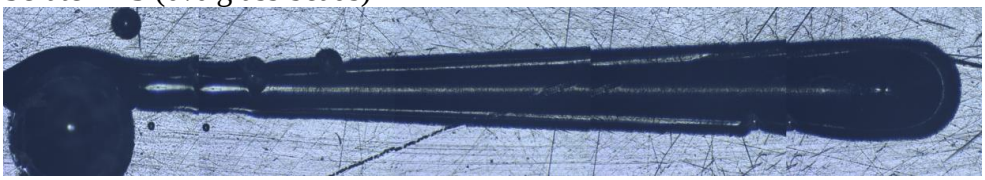

Scratch # 4 (0% glass beads)

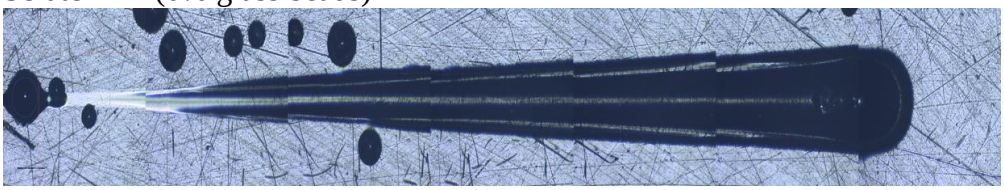

Scratch # 5 (0% glass beads)

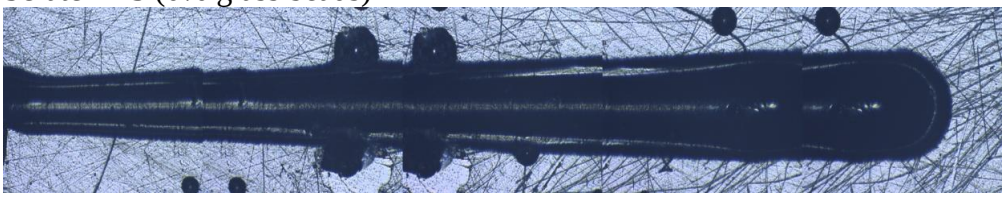

Scratch # 6 (0% glass beads)

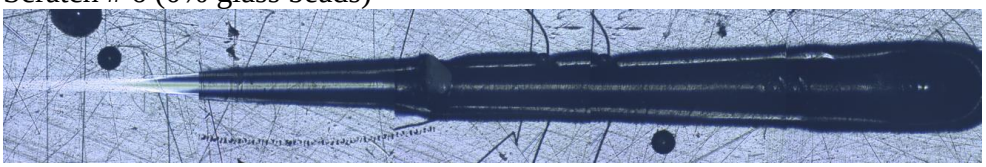

Scratch # 7 (0% glass beads)

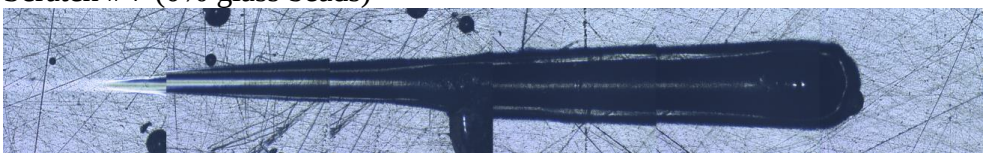

Scratch # 8 (0% glass beads)

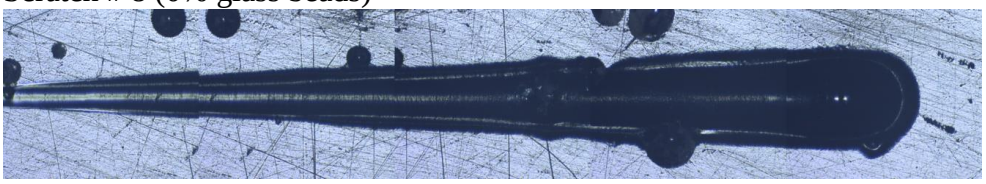

Scratch # 9 (0% glass beads)

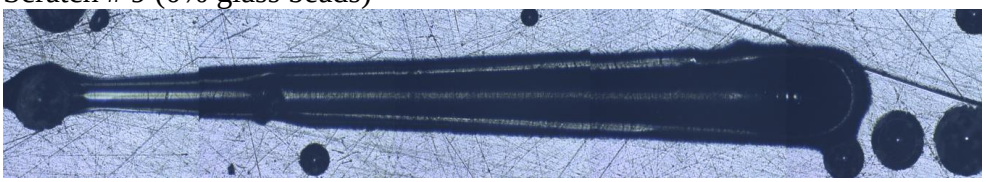

Scratch # 10 (0% glass beads)

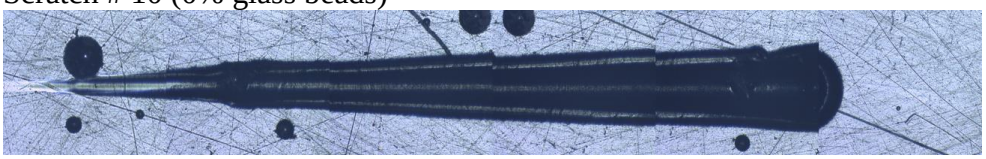

Scratch # 11 (0% glass beads)

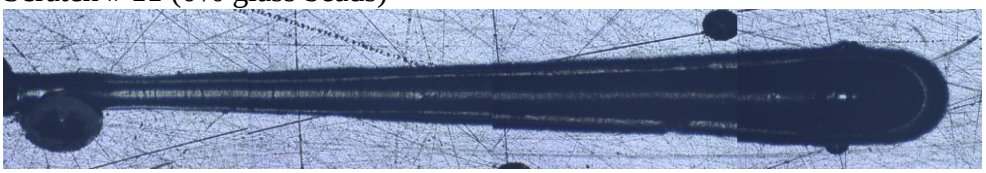

Scratch # 12 (0% glass beads)

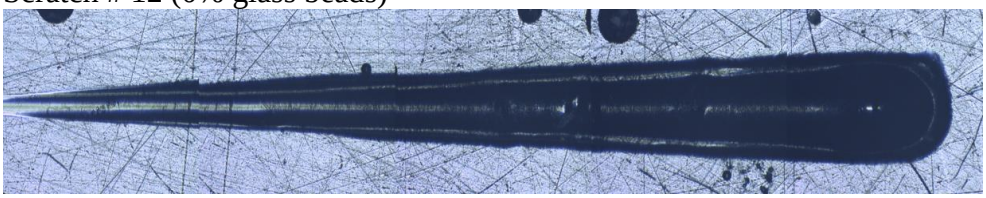

Scratch # 13 (0% glass beads)

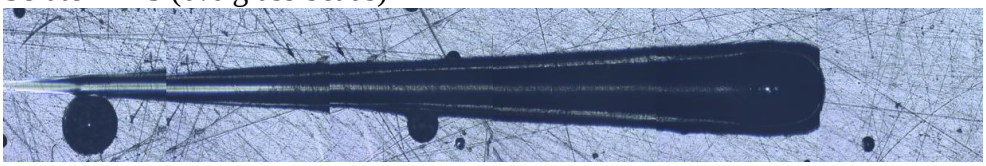

Scratch # 14 (0% glass beads)

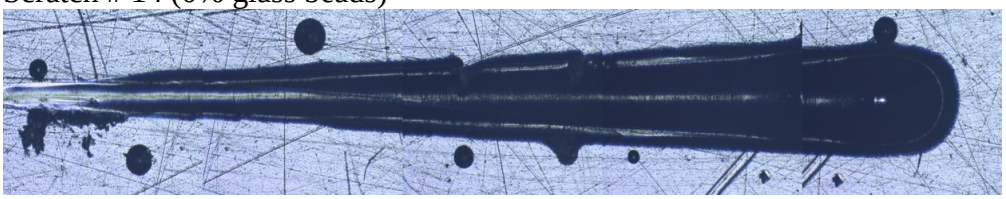

Scratch # 15 (0% glass beads)

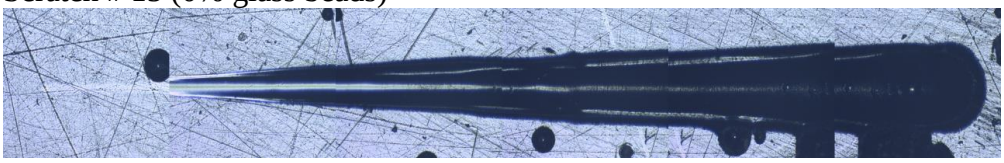

Scratch # 16 (0% glass beads)

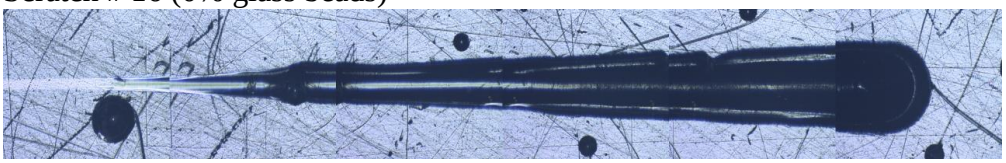

Scratch # 17 (0% glass beads)

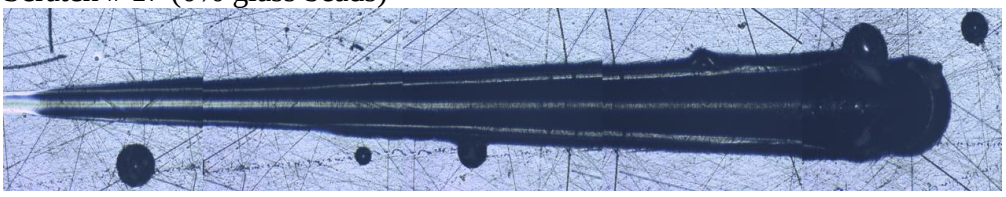

Scratch # 18 (0% glass beads)

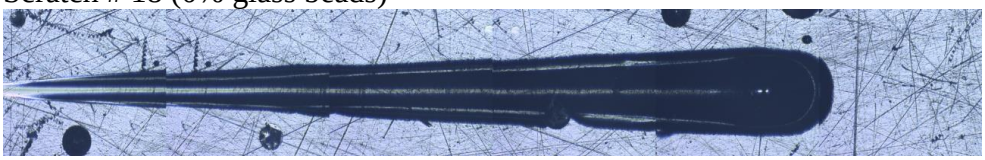

Scratch # 19 (0% glass beads)

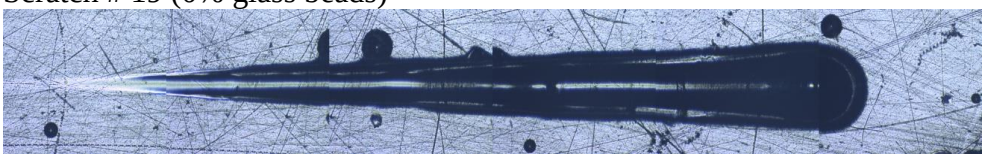

A.3 STATISTICAL ANALYSIS ANOVA FOR THE DATA FROM EXPERIMENTAL WORK

A.3.1 STATISTICAL ANALYSIS SUMMARY FOR THE THREE POINT-BENDING TEST

Table A.3.1 Average data with the deviation in 3PB-test data

Summary of 3PB test		
Vol.%	K_{IC}	STD-ERROR
0%	2.683851953	0.142007
5%	2.029405937	0.060606
25%	1.972677892	0.088226
50%	1.502989204	0.10207

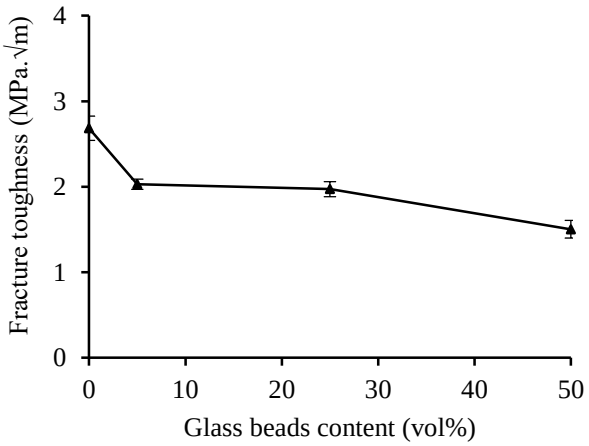

Figure A.3.1. Average data with the deviation in 3PB test data

A.3.2 STATISTICAL ANALYSIS SUMMARY FOR THE SCRATCH TEST

Table A.3.2 Average data with the deviation in scratch test data

Summary of scratch test		
Vol. %	K_{IC}	STD-ERROR
0	2.7	0.154445063
5	1.45	0.159898671
25	1.11	0.079668882
50	0.315	0.023614237

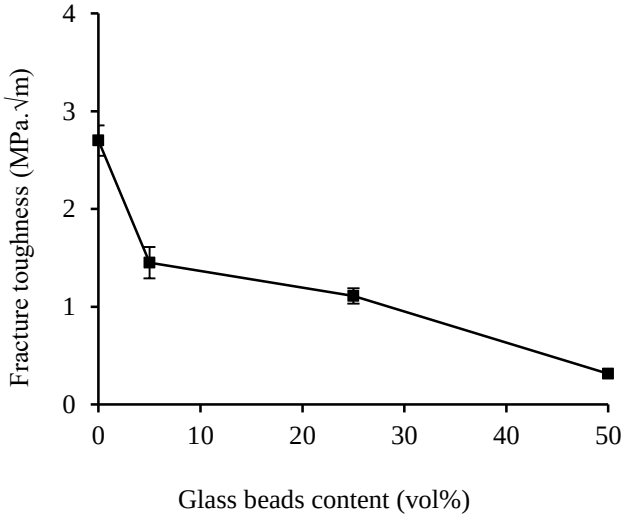

Figure A.3.2. Average data with the deviation in scratch test data

We separated the data affected by the kink in Figure A.3.2. to two figures one with kink point and one without kink point.

A.3.2.1 STATISTICAL ANALYSIS SUMMARY FOR THE SCRATCH TEST WITH KINK POINT

Table A.3.2.1 Average data with the deviation in the scratch test data with kink point

Summary of scratch test with kink point		
Vol. %	K_{IC}	STDERROR
0	0.94515	0.145735
5	0.842083	0.613452
25	0.5006	0.109177
50	0.26955	0.003182

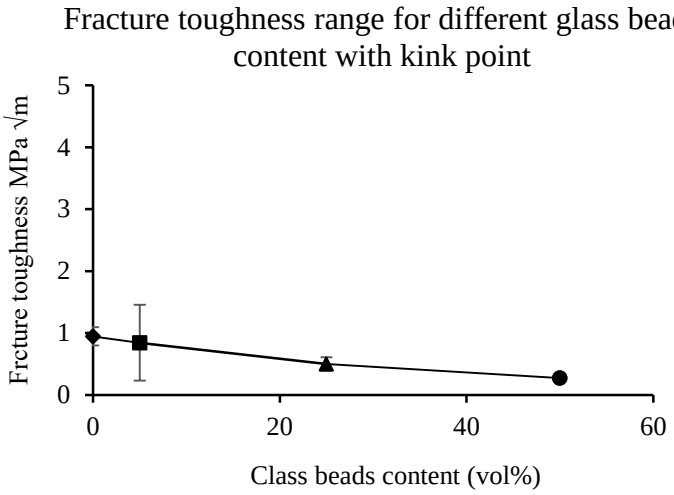

Figure A.3.2.1 Average data with the deviation in scratch test data with kink point

A.3.2.2 STATISTICAL ANALYSIS SUMMARY FOR THE SCRATCH TEST WITH WITHOUT KINK POINT

Table A.3.2.2 Average data with the deviation in the scratch test data with kink point

Summary of scratch test without kink point		
Vol. %	K_{IC}	STD-ERROR
0	2.601194	0.377558
5	3.0959	0.280863
25	1.46007	0.354601
50	0.46129	0.154464

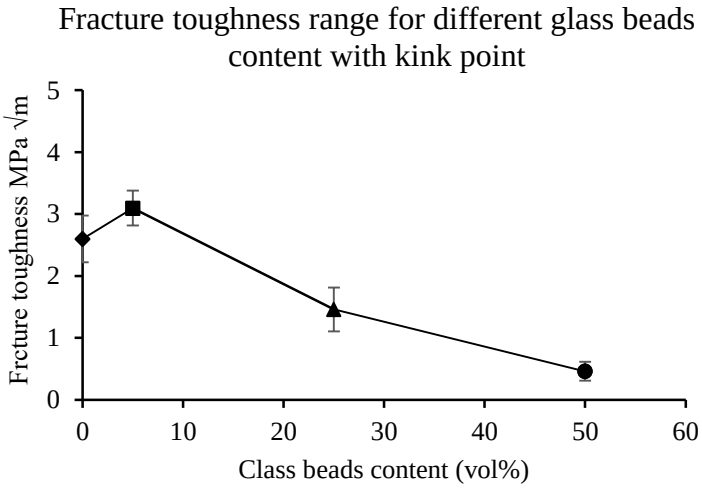

Figure A.3.2.2 Average data with the deviation in scratch test data without kink point

A.4 MATHEMATICAL SIMULATION FOR POLYMER MODELING

The aim of material modeling is to simulate mathematically the experimental behavior of a material. In this study, we demonstrate and formulate a linear viscous behavior of glass beads embedded in epoxy resin composites using scratching test. The proposed mathematical model allows us to interpret the experimental results data and predicate the behavior of the composite.

From literature

Author	Model representation
Shivakumar-2011	linear elastic or elastic-plastic static analysis
Shivakumar-2013	linear elastic or elastic-plastic static analysis
Thomas Wasik-2005	Linear elastic and isotropic

Two-Dimensional constitutive model

This model expected to contribute to the developments that have been made to predict the fracture behavior of polymers by considering the spatial location of inclusions to estimate the energy release rate using the J-integral [Rice].

The following assumptions are made in modeling the behavior of the polymer:

1.The crack is a straight line and propagates along the x-axis.

2.A two-dimensional representation of the model will be considered.

3.The Cartesian coordinates will be used throughout the derivation.

The visco-elastic material property is a mixture of simple two behaviors; elastic behavior which is a solid property and the viscous behavior is a fluid property. The total strain can be separated into elastic and viscous parts:

$$\underline{\underline{\varepsilon^{total}}} = \underline{\underline{\varepsilon^{elastic}}} + \underline{\underline{\varepsilon^{viscous}}} \qquad \text{(A.4.1)}$$

Because of the viscous effects, the viscous energy portion is not recovered when the external load removed, which can be considered as stationary energy is given by:

$$U_1 = u\ \underline{(\varepsilon^{viscous})} \tag{A.4.2}$$

The elastic portion can be represents the energy per unit volume $\varphi^{elastic}$, is given by:

$$U_2 = \varphi^{elastic}\ \underline{(\varepsilon^{elastic})} \tag{A.4.3}$$

The strain energy density is U_0 can be expressed in terms of elastic and viscous one.

$$U_0 = u\ \underline{(\varepsilon^{viscous})} + \varphi^{elastic}\ \underline{(\varepsilon^{elastic})} \tag{A.4.4}$$

Internal energy density

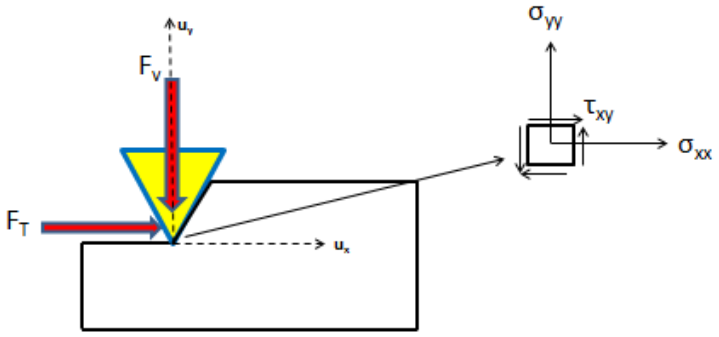

Figure A.4.1. Stress and displacement components in the Cartesian coordinate system

Figure A.4.1 shows the displacement in the x and y directions, respectively. The corresponding strain components are ε_x, ε_y, γ_{xy}. For small displacements in the planner problem the strain displacement can be written as follows:

$$\varepsilon_x = \frac{\partial u_x}{\partial x}\ ;\ \varepsilon_y = \frac{\partial u_y}{\partial y}\ ;\ \gamma_{xy} = \frac{\partial u_x}{\partial y} + \frac{\partial u_y}{\partial x} \tag{A.4.5}$$

The above strain components must satisfy the compatibility governing equation:

$$\frac{\partial^2 \varepsilon_x}{\partial y^2} + \frac{\partial^2 \varepsilon_y}{\partial x^2} = \frac{\partial^2 \gamma_{xy}}{\partial y \, \partial x} \quad \text{(A.4.6)}$$

Formulation of isothermal viscoelastic stress strain constitutive relation

The following series expansion is used to represent the strain energy density:

$$\varphi^e_{(\varepsilon)} = \frac{1}{0!}\varphi^e_{(\varepsilon_0)} + \frac{1}{1!}\frac{\partial \varphi^e_{(\varepsilon_0)}}{\partial \varepsilon}:(\varepsilon - \varepsilon_0) + \frac{1}{2!}(\varepsilon - \varepsilon_0): \frac{\partial^2 \varphi^e_{(\varepsilon_0)}}{\partial \varepsilon \otimes \partial \varepsilon}:(\varepsilon - \varepsilon_0) + \cdots\cdots\cdots\cdots$$

$$= \varphi^e_{(0)} + \sigma_0:(\varepsilon - \varepsilon_0) + \frac{1}{2}(\varepsilon - \varepsilon_0): \frac{\partial^2 \varphi^e_{(\varepsilon_0)}}{\partial \varepsilon \otimes \partial \varepsilon}:(\varepsilon - \varepsilon_0) + \cdots\cdots\cdots\cdots$$

$$= \frac{1}{2}\,\varepsilon: \frac{\partial^2 \varphi^e_{(\varepsilon_0)}}{\partial \varepsilon \otimes \partial \varepsilon}:\varepsilon$$

$$= \frac{1}{2}\,\varepsilon: C^e:\varepsilon \quad \text{(A.4.7)}$$

where: C^e = fourth order elasticity tensor, represent the material elastic properties. The general stress-strain relation is known as Hooke's law:

$$\sigma_{ij} = C_{ijkl}\,\varepsilon_{kl} \quad \text{(A.4.8)}$$

where, σ_{ij} : cauchy stresses (i,j = 1,2,3), ε_{kl} : linear strains (k,l = 1,2,3), C_{ijkl}: the standard elastic constants the six by six stiffness tensor. The stress component in the x-direction is:

$$\sigma_x = \frac{\partial^2 U}{\partial y^2} \quad \text{(A.4.9)}$$

As calculated equation A.4.7 can be written as:

$$\varphi^{elastic} = \frac{1}{2}\,\underline{\underline{\varepsilon^{elastic}}} : C_0 : \underline{\underline{\varepsilon^{elastic}}}$$

The stress and strain vectors are symmetric, $\sigma = \sigma^T$ and $\varepsilon = \varepsilon^T$, the elastic modulus tensor C_0 must also possess a similar symmetry with respect to the first and second pairs of its indices

$C_{ijkl} = C_{jikl} = C_{ijlk} = C_{jilk}$

Derivation of linear visco-elastic solid

The material behavior was modeled as linear viscous model to simulate the experimental behavior. The constitutive model developed in this study is for epoxy resin composites. It consists of a combination of springs and a dashpot. When the spring is connected to dashpot in series yields a Maxwell model. A combination of the Maxwell model in parallel with a spring as its illustrated in Figure A.4.2, yields the model that we proposed for in this study to predict the shape of the compressive stress-strain curve.

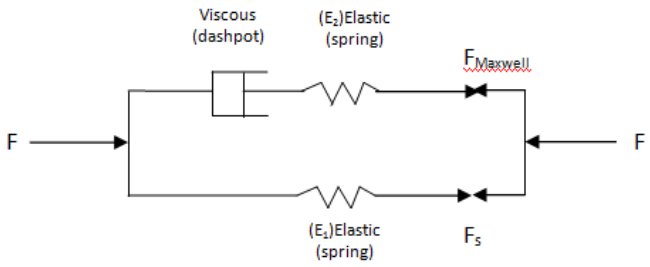

Figure A.4.2. Proposed model for the epoxy resin

The spring represents the elastic part of a visco-elastic material which is represent time dependent deformation process:

$$\sigma_{(t)} = E\ \varepsilon_{(t)} \qquad \text{(A.4.10)}$$

where, E: is Young's modulus of epoxy.

The representation of the viscous component of the visco-elastic material can be done by presenting the dashpot in the model, the stress is proportion to time derivative of strain:

$$\sigma_{(t)} = \eta\ \varepsilon'_{(t)} \quad \text{(A.4.11)}$$

where: $\varepsilon' = \frac{d\varepsilon}{dt}$, η: is fluid viscosity in the dashpot. When the spring and the dashpot are in series, the stress will be equal:

$$\sigma_{(t)} = \varepsilon\ E + \eta\varepsilon' \quad \text{(A.4.12)}$$

Model solving

In "Maxwell model" the spring and the dashpot are in series, therefore, the stresses in the spring and the dashpot are equal and the strains are additive:

$$\sigma_{Maxwell} = \sigma_{spring} = \sigma_{viscous} \quad \text{(A.4.13)}$$

$$\varepsilon_{Maxwell} = \varepsilon_{spring} + \varepsilon_{viscous} \quad \text{(A.4.14)}$$

But, if the spring and the Maxwell model in parallel, the strains are equal and the stresses are additive:

$$\varepsilon_{total} = \varepsilon_{Spring} = \varepsilon_{Maxwell} \quad \text{(A.4.15)}$$

$$\sigma_{total} = \sigma_{Spring} + \sigma_{Maxwell} \quad \text{(A.4.16)}$$

$$\sigma_{total} = E_1\varepsilon + (E_2\varepsilon + \eta\frac{d\varepsilon}{dt}) \quad \text{(A.4.17)}$$

The next step will be dividing the above equation by the viscosity η:

$$\frac{\sigma}{\eta} = \frac{E_1}{\eta}\varepsilon + \frac{E_2}{\eta}\varepsilon + \frac{d\varepsilon}{dt} \quad \text{(A.4.18)}$$

$$\frac{d\varepsilon}{dt} = \frac{\sigma}{\eta} - \frac{E_1}{\eta}\varepsilon - \frac{E_2}{\eta}\varepsilon \quad \text{(A.4.19)}$$

Integrating both sides of the equation:

$$\int dt = \int \frac{d\varepsilon}{\frac{\sigma_0}{\eta} - \frac{(E_1+E_2)}{\eta}\varepsilon} \tag{A.4.20}$$

$$\varepsilon_t = \frac{\sigma_0}{(E_1+E_2)}\left[1 - e^{-\frac{(E_1+E_2)t}{\eta}}\right] \tag{A.4.21}$$

Among many kinds of DGERBA epoxides, DER 661 was used in this research because of high viscosity (the viscosity=η=400 MPa.s from Material Safety Data Sheet) to avoid the settlement of the glass beads to the bottom mold. The epoxy modulus of elasticity (E_1 and E_2) is given in Material Safety Data Sheet, which is equal to 2.8 GPa.

A.1 MATLAB CODE USED IN GENERATING RANDOM PARTICLE DISTRIBUTION

In this section, we are presenting a commended MATLAB code used to generate sixty fields of three different populations of random pixels for each population. The populations were chosen to match the experimental test ranging from 5%, 25% and 50%. The size of the image was chosen to be 100x100 pixels.

```
clear all
clc
%*************************************************************************
% ****************** Radial Distribution Function (RDF) ********************
% ******************       By Shahlaa Al Wakeel       ***********************
%*************************************************************************
%*************************************************************************
% Scriptfile name: GofR.m (Plot DRF of N particles in volume V) **************
%*************************************************************************
% Purpose:
%                  This file is used to calculate the probability of finding particles
%                    in a shell of delta r at a distance r from a reference point
%
%*************************************************************************
%-------------------------------------------------------------------------------------------------
%----------------------------- READING AND DISPLAY OF IMAGE ----------------------------

 PixelSize = 100; % creates a 100x100 matrix basically the image size
 PartWeight = 0.25;    % weight of the black pixels
 numImage = 60;

 %create a matrix of zeros that will hold the histogram values for making the average on the final plot.

g_rValues = zeros (numImage, ceil (sqrt (PixelSize^2 + PixelSize^2)));
 for imagecount = 1: numImage
        display (['Image number: ', num2str(imagecount)])
        imageName = [num2str(imagecount),'_', num2str(PartWeight*100),'%.jpeg'];
        I = imread(imageName);
        level = graythresh(I); % computes a global threshold (level) that can be used to convert an
                                    intensity image to a binary image with im2bw.
        % level is a normalized intensity value that lies in the range [0, 1]
        BW = im2bw (I, level); % convert the gray image to black and white,
        d = size (BW); % sizes of each dimension of array BW in a vector
```

```
        k = 0; %index of the radial distance between the black pixels
        blackcount = 0; %initial value for the number of black pixels
      for followPixel = 1: (d (1) *d (2))-1 % followPixel is the particle of
                                  interest - the one being compared
         if BW(followPixel) == 0 %counting the number of black pixels
           blackcount = blackcount + 1;
           for leadPixel = (followPixel+1): d (1) *d (2)
             if BW(leadPixel) == 0 % two conditions: if i particle and j
                          particle have same color and (&&) i
                          particle color is black
        k = k + 1;
        [y_i, x_i] =ind2sub([size(BW(:,:),1),size(BW(:,:),2)],followPixel);
        [y_j, x_j] = ind2sub([size(BW(:,:),1),size(BW(:,:),2)],leadPixel);
        r(k)= abs(round(sqrt( ((x_i-x_j)^2) + ((y_i-y_j)^2))));

            end
          end
       end
    end
    if BW(end,end) == 0 %checks the last pixel to see if it is also black
       blackcount = blackcount + 1;
end

    %histogram for distribution:
    figure (1);
    edges = 1:(ceil(sqrt(length(BW)^2+length(BW)^2))); %this arranges the
                    histogram values so each bar is for the next r value
    h = histogram(r,edges); %to plot the histogram of the r values, separated
                        on the x axis in the "edges" increments

    if imagecount == 1
      xmax = max(r)*1.1;
      ymax = max(h.Values)*2;
    end
    figure (1);

    %subplot (6,10, imagecount);
    axis ([0, xmax,0, ymax])
    axis off %makes the axis numbers invisible in the subplot

    %change color of the histogram bars, because it will be blue by default
    h.FaceColor = [0,0,0]; %sets color to black (rgb values all 0)
    nelements = h.Values;
    centers = h.BinEdges(2:end);

    %calculating and plotting the g(r)
```

```
figure (2)
hold on
g_r = nelements/blackcount;
g_rValues(imagecount,(1:length(g_r))) = g_r; %saves the g(r) values in
                        the matrix for the final average plot
plot(centers,g_r);
xlabel('radial distance (in pixels)')
ylabel('g(r) probability')
```

APPENDIX B

In this appendix, we show the related material mentioned in chapter 4. Including the calculation of the polymer's modulus of elasticity E_0 the composites modulus.

B.1 POLYMER MODULUS OF ELASTICITY CALCULATION

Uniaxial tension test under a controlled rate of displacement rate of 5 mm/min was conducted at room temperature following the ASTM D638. The machine measures the load and the corresponding displacement through a computerized data acquisition system. From the collected data, the stress versus the strain responses was plotted, Figure B.1, and the elastic modulus was calculated using the slope of the linear portion of the stress versus the strain curve. The average modulus of epoxy/glass was found to be 1850 MPa.

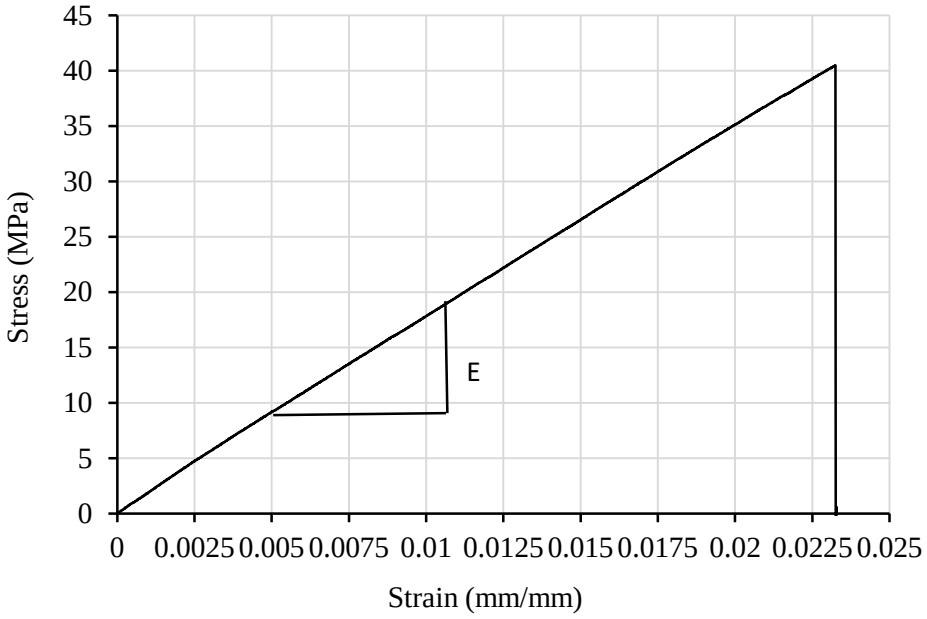

Figure B.1. Stress-strain curve showing the polymer behavior under uniaxial tension test

B.2 POLYMER DENSITY AND POROSITY CALCULATIONS

Measured density (M_d)

The density was found by dividing the weight of the specimen by its volume. Specimen volume was calculated as 4.0x 2.0x 1.059=8.472 cm^3.

B.2.1. Polymer measured density calculations

Vol. % glass beads	Measured weight (g)	Measured volume (cm^3)	Measured density (g/cm^3)
0%	10.2	8.472	1.2
5%	9.34	8.472	1.16
25%	8.35	8.472	0.99
50%	5.98	8.472	0.79

Theoretical density (T_d)

Per ASTM D2734, the theoretical density of a composite can be calculated using the following equation:

$$T_d = \frac{100}{\left(\frac{R}{D} + \frac{r}{d}\right)} \quad \text{(B.2.1)}$$

where, T is the theoretical density, R is the percent weight of the resin in the composite, weight %, D is the resign density (1.204 g/cm^3), r is the percent weight of the glass beads in the composite and d is the glass beads density (0.38 g/cm^3).

Table B.2.2. Polymer's theoretical density calculations

Vol. % glass beads	% weight of the resin	% weight of the hardener	Total % weight	% weight of glass beads	Theoretical density (g/ cm^3)
0%	0.891	0.109	1	0	1.15
5%	0.877	0.107	0.984	0.016	1.11
25%	0.807	0.098	0.905	0.095	0.96
50%	0.678	0.082	0.76	0.24	0.77

Void content

Per ASTM D2734, the void content was calculated using the following equation:

$$V = 100\ (T_d - M_d)/T_d \quad \text{(B.2.2)}$$

where, V is the void ratio, (T_d) is the theoretical density (g/cm^3) and (M_d) is the measured density (g/cm^3).

Then the porosity, O, will be calculated using the following equation:

$$O = \frac{V}{1+V} \quad \text{(B.2.3)}$$

The results are listed in Table B.2.3

Table B.2.3. Polymer's theoretical density calculations

Vol. % glass beads	Theoretical density (g/ cm^3)	Measured density (g/cm^3)	Void ratio %	Porosity %
0%	1.15	1.2	0.048	0.05
5%	1.11	1.16	0.47	0.05
25%	0.96	0.99	0.39	0.04
50%	0.77	0.79	0.029	0.03

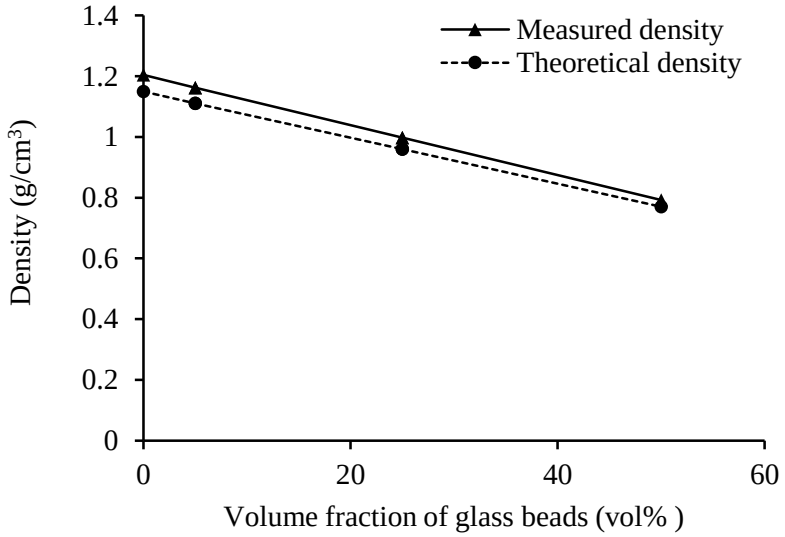

Figure B.2. Polymer's Theoretical and measured density for different glass beads content

APPENDIX C

In this appendix, we show the related material mentioned in chapter 5. Including the calculation of the porosity and composites modulus calculations. Detailed ANOVA analysis is shown in section C.2.

C.1 POROSITY CALCULATION FOR AGED INJECTED CEMENT WITH SiO_2 PARTICLES

Following up the ASTM C830, calculations were performed to obtain the porosity value of the aged cement paste injected with SiO_2 particles. The volume was calculated by subtracting the suspended weight from the saturated weight in grams divided by the water density (1gram/cm^3):

$$\text{V in cm}^3 = \frac{(\text{W} - \text{S}) \text{ in gram}}{\text{water density in gram/cm}^3} \quad \text{(C.1.1)}$$

The porosity is obtained by subtracting the saturated weight from the dry weight divided by volume, as follows:

$$\text{P, \%} = \frac{(\text{W}-\text{D}) \text{ in gram}}{\text{V in cm}^3} * 100 \quad \text{(C.1.2)}$$

Table C.1. Cement paste porosity calculation

Slice #	W Fully saturated weight (g)	S Suspended weight (g)	V Volume (cm^3)	D Dry weight (g)	P Porosity (%)
L1	19.7	9.5	10.2	15.6	40
L2	19	9.2	9.8	15	41
L3	20.2	9.8	10.4	15.9	41
L4	20.6	9.9	10.7	16.2	41
L5	18.3	8.8	9.5	14.4	41
L6	22.2	10.7	11.5	17.4	42
L7	20.2	9.7	10.5	15.8	42
L8	16.8	8	8.8	13.2	42
L9	15.5	7.5	8	12.2	42

C.2 ANOVA ANALYSIS FOR AGED CEMENT PASTE

	Slice #2	**x-mean**	**(x-man)^2**
	0.793676	0.057571	0.003314
	0.702409	-0.0337	0.001135
	0.802918	0.066814	0.004464
	0.82949	0.093385	0.008721
	0.561465	-0.17464	0.030499
	0.72667	-0.00943	8.9E-05
sum	4.416627		0.048223
mean	0.736105		

	Slice #3	x-mean	$(x\text{-man})^2$
	0.620384	0.036584	0.001338374
	0.625005	0.041205	0.001697845
	0.62385	0.04005	0.001603973
	0.569552	-0.01425	0.000203018
	0.591502	0.007702	5.93185E-05
	0.472509	-0.11129	0.012385858
sum	3.502803		
mean	0.5838		0.017288387

	Slice #4	x-mean	$(x\text{-man})^2$
	0.648111	0.037547	0.00141
	0.564931	-0.04563	0.002082
	0.584571	-0.02599	0.000676
	0.815626	0.205062	0.04205
	0.399726	-0.21084	0.044453
	0.650421	0.039857	0.001589
sum	3.663386		0.09226
mean	0.610564		

	Slice #5	x-mean	$(x\text{-man})^2$
	0.640024	0.058919	0.003471
	0.650421	0.069317	0.004805
	0.593813	0.012708	0.000161
	0.4159	-0.1652	0.027293
	0.605366	0.024261	0.000589
	0.581105	0	0
sum	3.486629		0.036319
mean	0.581105		

	Slice #6	x-mean	$(x\text{-man})^2$
	0.58226	-0.09377	0.008793
	0.622695	-0.05334	0.002845
	0.708185	0.032155	0.001034
	0.66313	-0.0129	0.000166
	0.72667	0.05064	0.002564
	0.753241	0.077211	0.005962
sum	4.056181		0.021364
mean	0.67603		

	Slice #7	**x-mean**	**(x-man)^2**
	0.62154	0.113987	0.012993
	0.640024	0.132472	0.017549
	0.60421	0.096658	0.009343
	0.545291	0.037739	0.001424
	0.293441	-0.21411	0.045844
	0.340807	-0.16675	0.027804
sum	3.045313		0.114957
mean	0.507552		

	Total observations	x-mean	(x-man)^2
	0.793676	0.177817	0.031618715
	0.702409	0.08655	0.007490828
	0.802918	0.187059	0.034990974
	0.82949	0.21363	0.045637835
	0.561465	-0.05439	0.002958744
	0.72667	0.11081	0.012278946
	0.620384	0.004525	2.04742E-05
	0.625005	0.009146	8.36484E-05
	0.62385	0.007991	6.38508E-05
	0.569552	-0.04631	0.002144374
	0.591502	-0.02436	0.000593269
	0.472509	-0.14335	0.020549432
	0.648111	0.032252	0.00104016
	0.564931	-0.05093	0.002593712
	0.584571	-0.03129	0.000978988
	0.815626	0.199767	0.039906775
	0.399726	-0.21613	0.046713577
	0.650421	0.034562	0.001194536
	0.640024	0.024165	0.000583926
	0.650421	0.034562	0.001194536

	0.593813	-0.02205	0.000486051
	0.4159	-0.19996	0.039983741
	0.605366	-0.01049	0.000110119
	0.581105	-0.03475	0.001207883
	0.58226	-0.0336	0.001128915
	0.622695	0.006835	4.67226E-05
	0.708185	0.092326	0.008524083
	0.66313	0.04727	0.002234464
	0.72667	0.11081	0.012278946
	0.753241	0.137382	0.018873758
	0.62154	0.00568	3.22637E-05
	0.640024	0.024165	0.000583926
	0.60421	-0.01165	0.0001357
	0.545291	-0.07057	0.004979874
	0.293441	-0.32242	0.103953885
	0.340807	-0.27505	0.075653829
mean	0.615859	SST	0.52285146

Total Sum of Squares (SST) 0.52285146

Sum of Squares within Groups (SSW) 0.33040994

Sum of squares between Groups (SST-SSW) 0.19244152

Degree of freedom (DOF)

Numerator (number of individual group -1) 5

Denominator (number of observation- Numerator) 30

Sum of squares between Groups/DOF 0.038488

Sum of Squares within Groups/DOF 0.011014

F-ratio 3.494596

F (5,30) 3.494596

Critical value from F- table 2.5336

2.5336 < 3.495

reject null hypothesis

APPENDIX D

In this appendix, we show the related material mentioned in chapter 6, including a MATLAB code used to generate sixty fields of different particle arrangement and orientation. SIF calculations based on finite element analysis.

D.1 MATLAB CODE USED IN GENERATING DIFFERENT PARTICLE ARRANGEMENTS AND ORIENTATIONS

In this section, we are presenting a commended MATLAB code used to generate sixty different populations of particle arrangements and orientations.

```
clear all
clc
%*************************************************************************
% ****************Fracture toughness of different particles arrangements **************
% ****************************and orientations ********************************
% *************************************************************************
% ********************      By Shahlaa Al Wakeel      ***************************
%*************************************************************************
%*************************************************************************
% Scriptfile name: Partarrang.m ***************************************************
%*************************************************************************
% Puropse:
%                 This file is used to calculate the fracture toughness of different particles
%                  arrangement and orientations in front of crack tip of single edge notch
%
%*************************************************************************


PartArea=2513.275;
PartRadius=20;
ZoneVolume=9650972.63;
FirstIntegral_1=(PartArea*2)/ZoneVolume;
E=70000;
v=0.25;
%parameters
a = 0.00006;
b = 0.00002;

n=60;

x1_angle = 90; %REFERENCE ANGLE FOR THE X AXIS OF THE PARTICAL (relative to
vertical);
%%%%%%%%%%%%%%%%%%%%%%%%%% Particle arrangements %%%%%%%%%%%%%%%%%%%%%%%%%%
```

```
x2_angle = 0; % 0 deg -> vertical particle
              % 90 deg -> horizontal particle
              % -45 deg -> diagonal right (positive slope)
              % +45 deg -> diagonal left (negative slope)


for i=1:n
%%%%%%%%%%%%%%%%%%%%%%%%% Particle (1)
PosArrang11(i) = randi(161)-1;%% O to 160
PosArrang21(i) = randi(81)-1;
%%%%%%%%%%%%%%%%%%%%%%%%% Particle (2)
PosArrang12(i) = randi(161)-1;
PosArrang22(i) = randi(81)-1;

 D = (((PosArrang12(i)-PosArrang11(i))^2  )+((PosArrang22(i)-
PosArrang21(i))^2))^0.5; %check


while D < 2*PartRadius

    PosArrang11(i) = randi(161)-1;
    PosArrang21(i) = randi(81)-1;
    %%%%%%%%%%%%%%%%%%%%%%%%% Particle (2)
    PosArrang12(i) = randi(161)-1;
    PosArrang22(i) = randi(81)-1;

    D = (( (PosArrang12(i)-PosArrang11(i) )^2)+((PosArrang22(i)-
PosArrang21(i))^2))^0.5; %check
%     Dist(i) = D;

end

while ( (PosArrang11(i) == 80 && PosArrang21(i) == 0) ||  (PosArrang12(i) ==
80 && PosArrang22(i) == 0))
      PosArrang11(i) = randi(161)-1;%% O to 160
    PosArrang21(i) = randi(81)-1;
    %%%%%%%%%%%%%%%%%%%%%%%%% Particle (2)
    PosArrang12(i) = randi(161)-1;
    PosArrang22(i) = randi(81)-1;
end
rArrang1(i)=sqrt((PosArrang11(i)-80)^2 + (PosArrang21(i))^2);
theta1(i)=atan2(PosArrang21(i),PosArrang11(i)-80);

rArrang2(i)=sqrt((PosArrang12(i)-80)^2 + (PosArrang22(i))^2);
theta2(i)=atan2(PosArrang22(i),PosArrang12(i)-80);


   SecondIntegral1 = 1/((rArrang1(i))^(3/2))*cos(3*theta1(i)/2);
   SecondIntegral2 = 1/((rArrang2(i))^(3/2))*cos(3*theta2(i)/2);

    S1=abs( SecondIntegral1 * 1.28e-8);
    S2=abs( SecondIntegral2 * 1.28e-8);
```

```
   alpha1 = abs(x1_angle - theta1(i));
   alpha2 = abs(x2_angle - theta2(i));

   eps1 = 180/(70000*pi*a*b) * (pi*a *( a - (a+b)*cos(2*alpha1)));
   eps2 = 180/(70000*pi*a*b) * (pi*a *( a - (a+b)*cos(2*alpha1)));

   deltaK1(i)=((E*eps1)/(6*(sqrt(2*pi))*(1-
v)))*(FirstIntegral_1*0.000001)*S1;
   deltaK2(i)=((E*eps2)/(6*(sqrt(2*pi))*(1-
v)))*(FirstIntegral_1*0.000001)*S2;

end
```

D.2 SIF BASED ON FINITE ELEMENT ANALYSIS RESULTS CONSIDERING PARTICLE ARRANGEMENTS AND ORIENTATIONS

D.2.1 Ordered arrangements

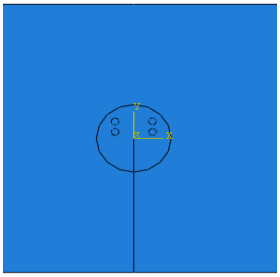

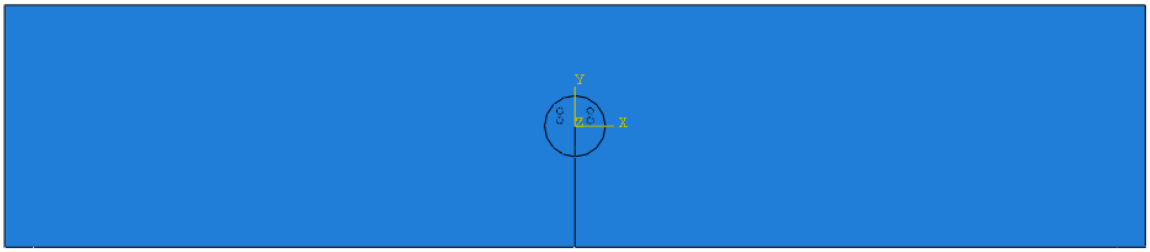

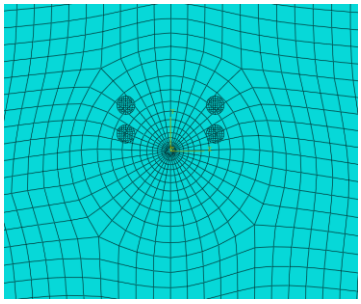

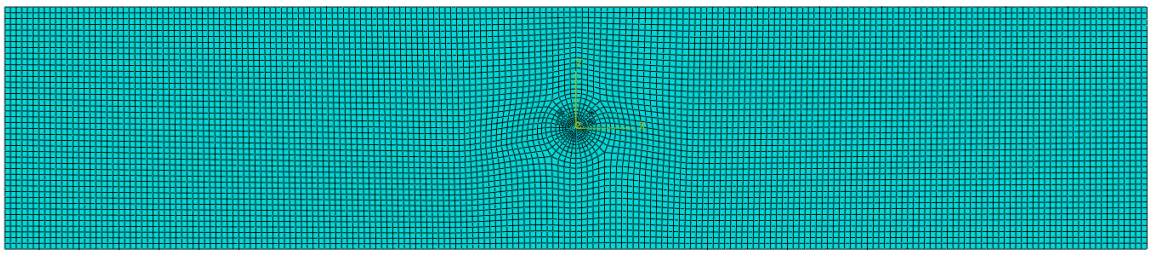

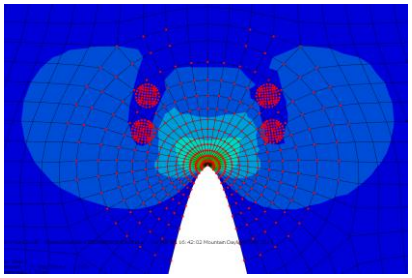

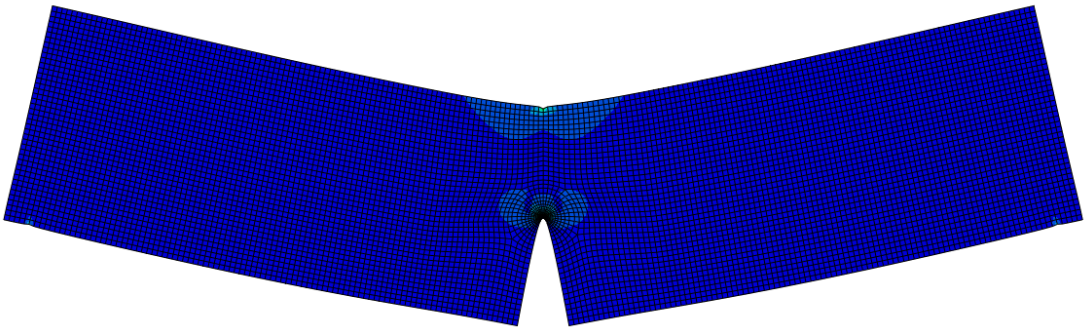

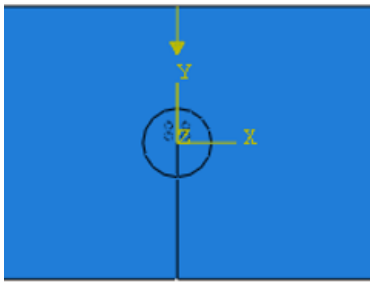
Y
Z
X

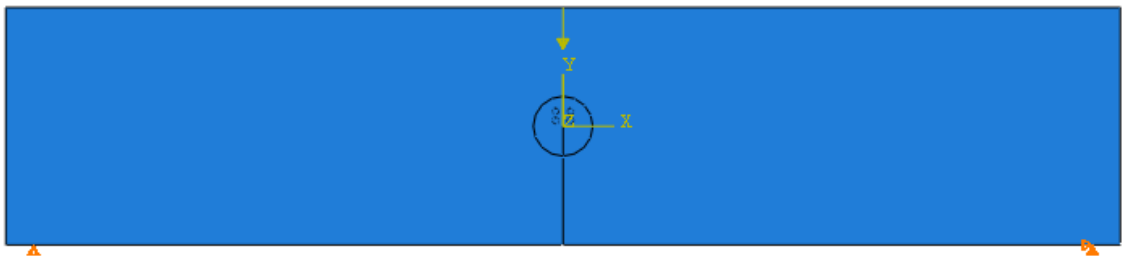
Y
Z
X

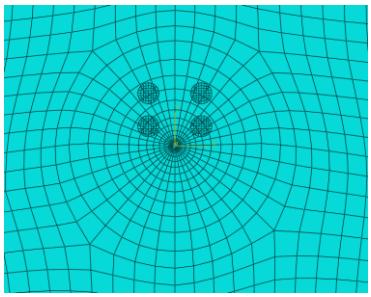

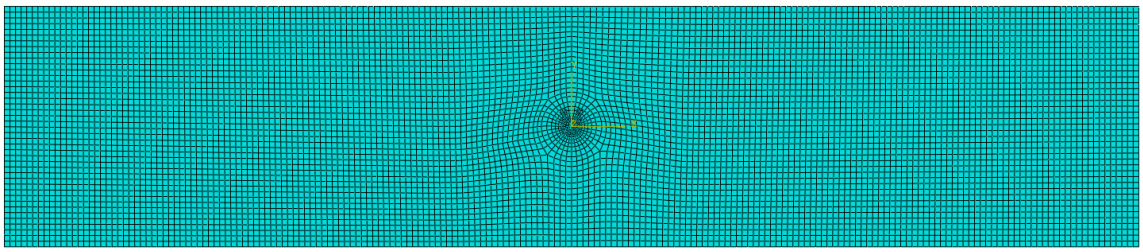

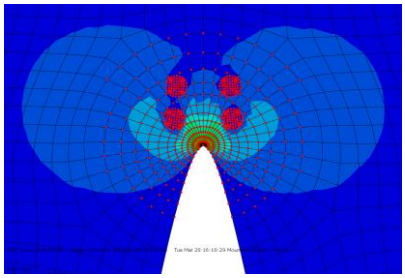

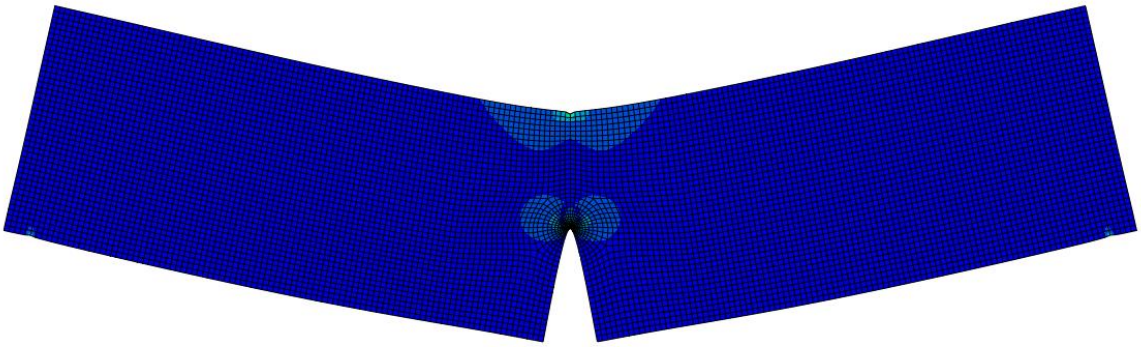

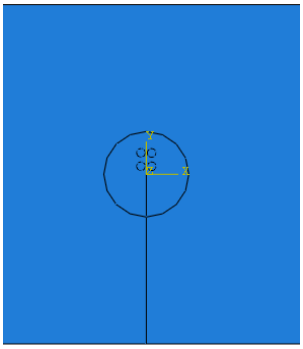

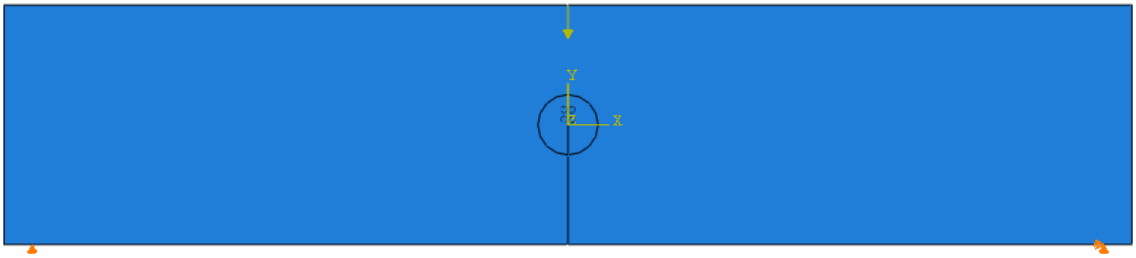

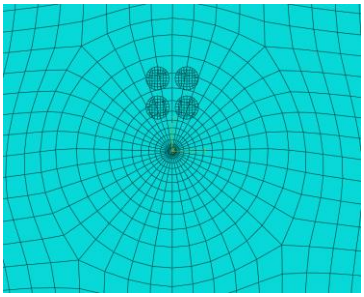

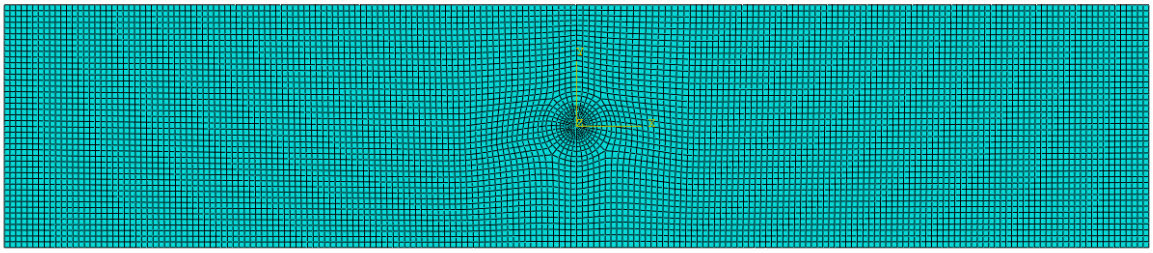

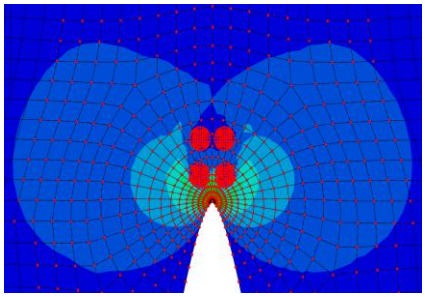

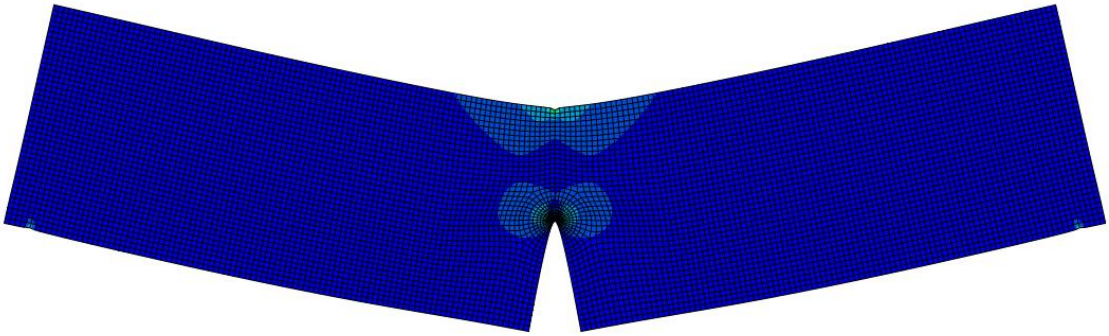

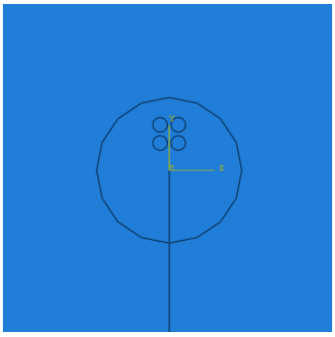

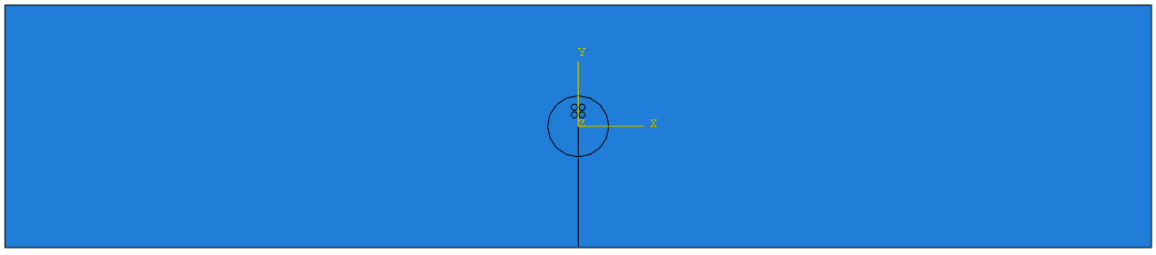

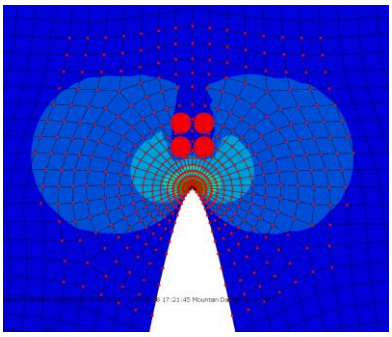

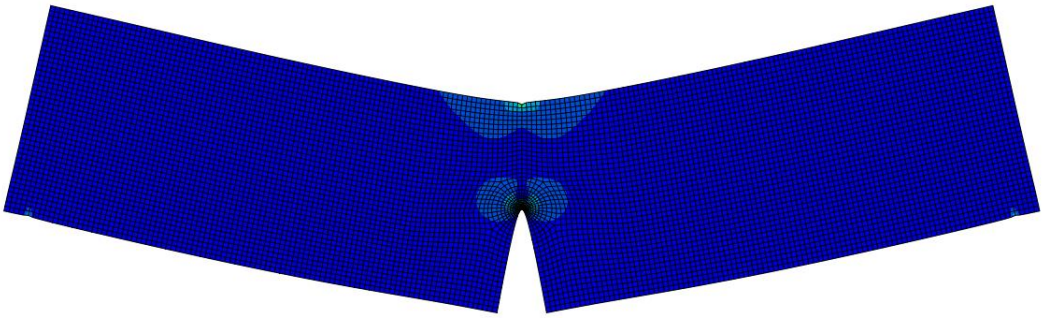

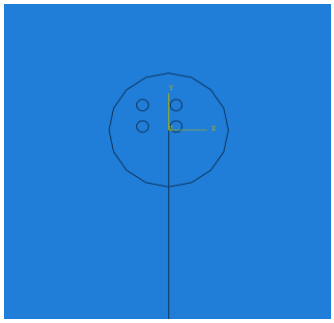

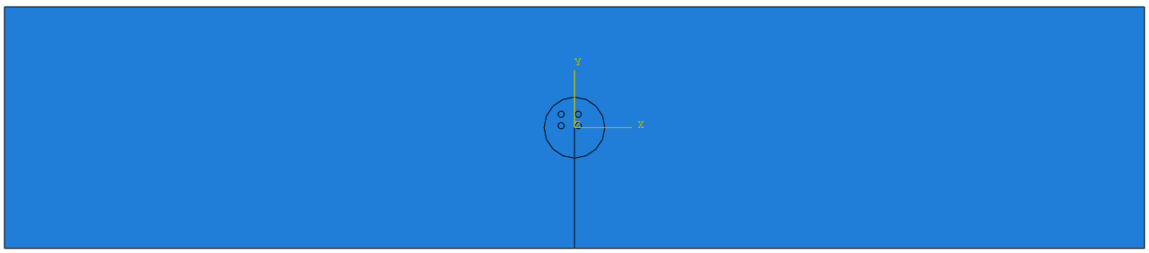

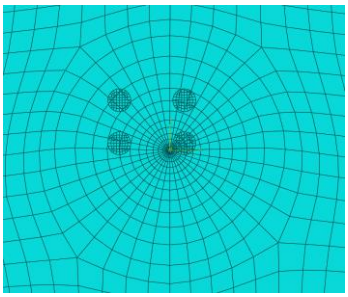

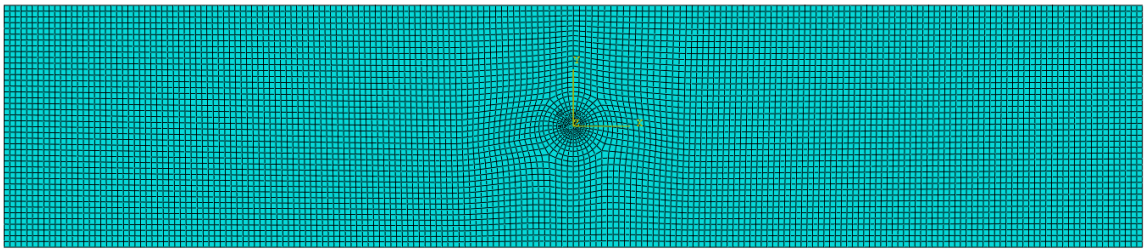

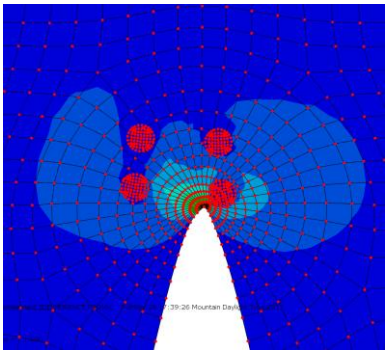

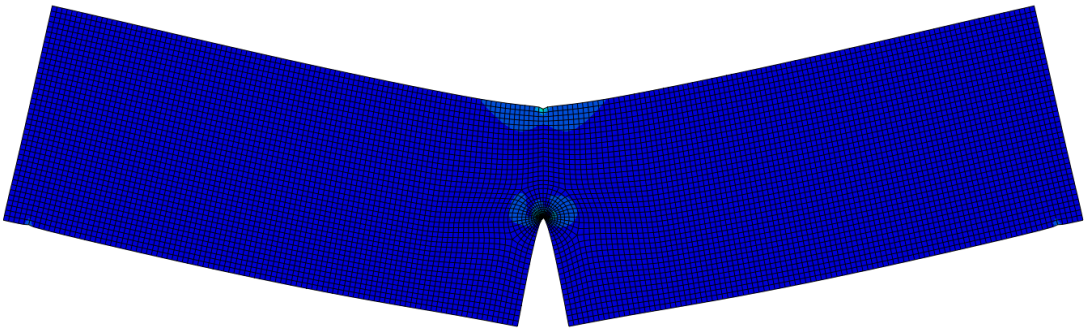

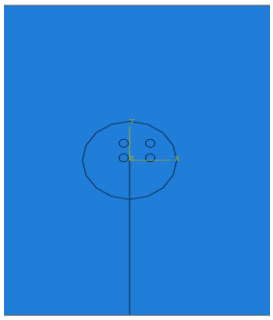

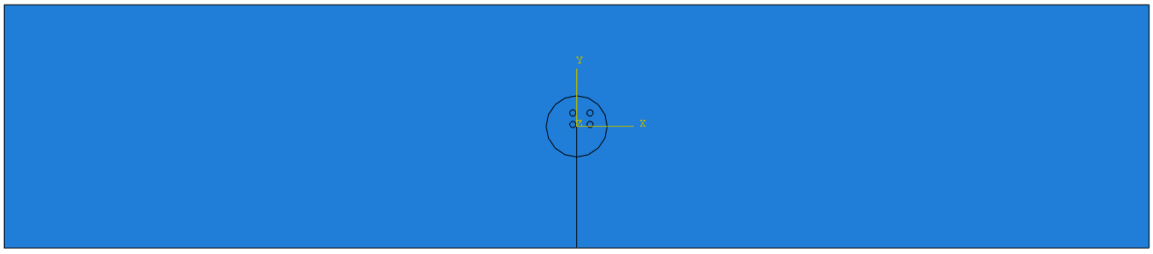

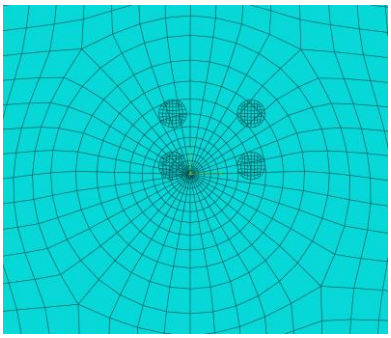

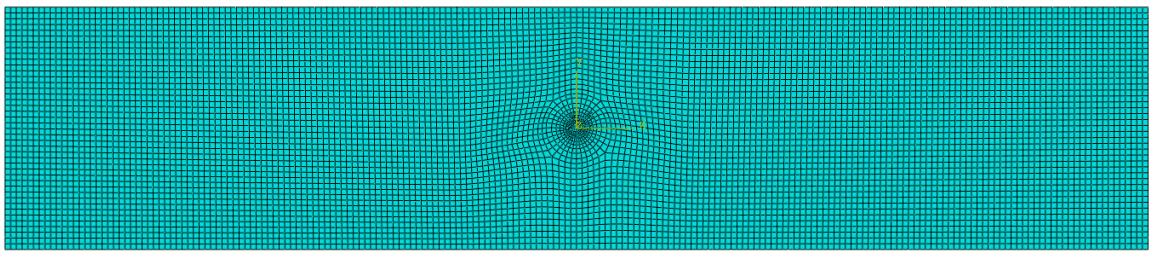

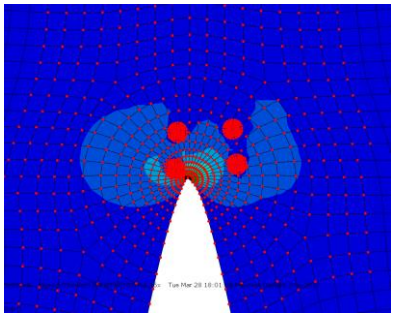

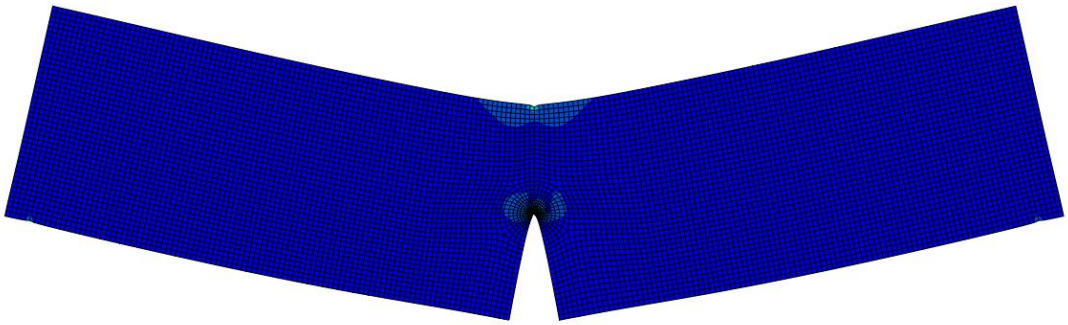

D.2.2 Random arrangements

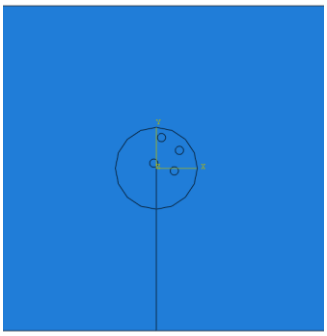

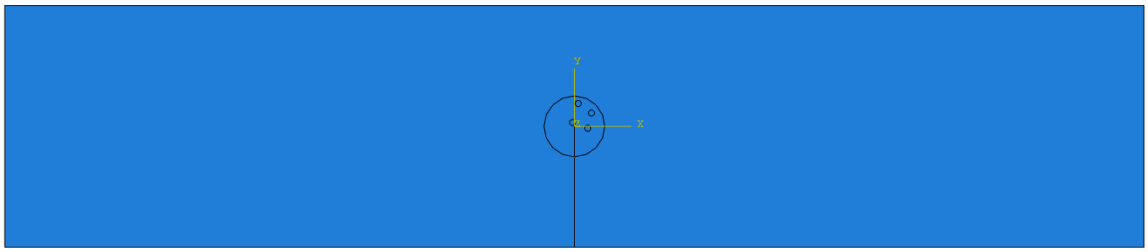

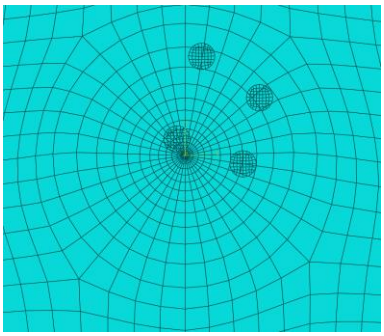

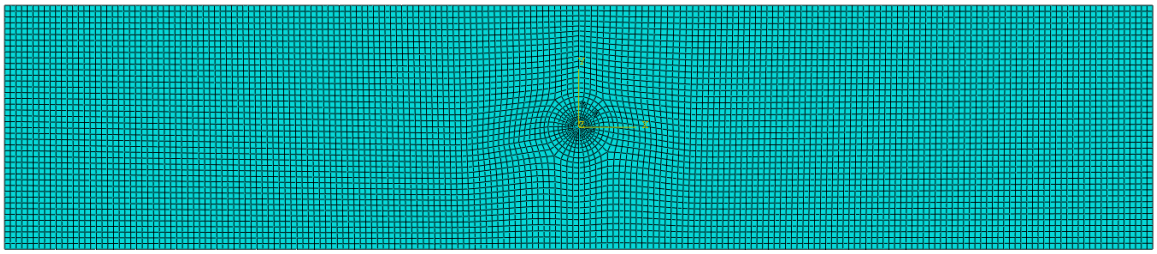

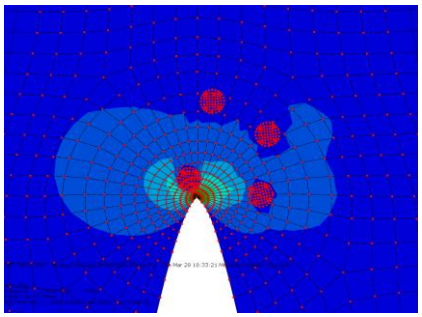

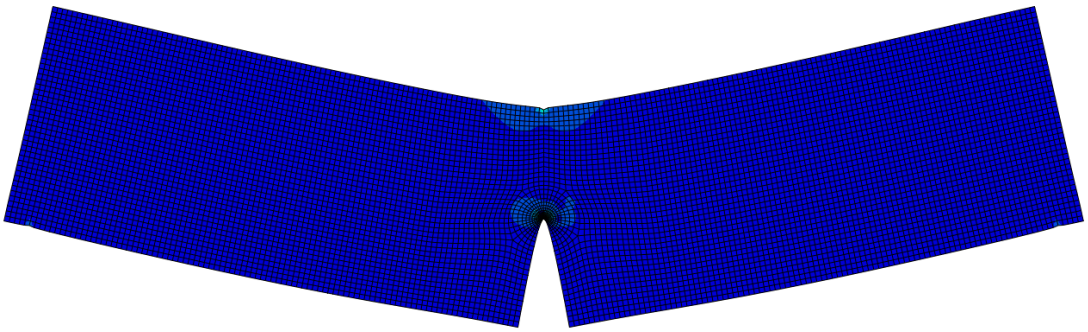

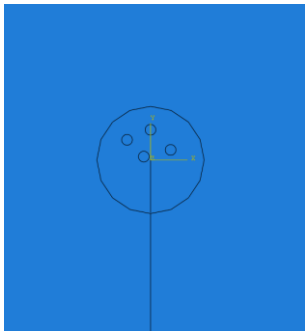

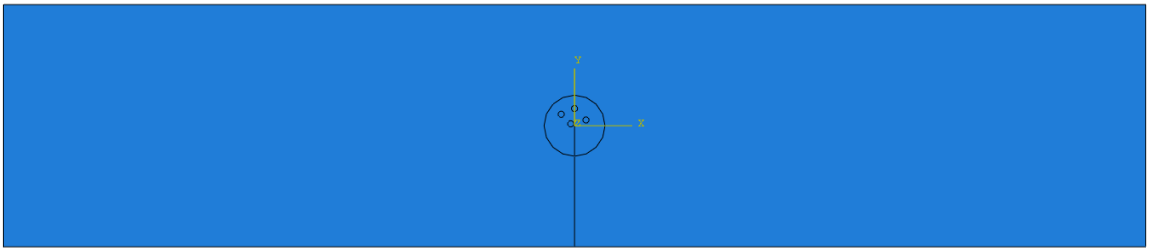

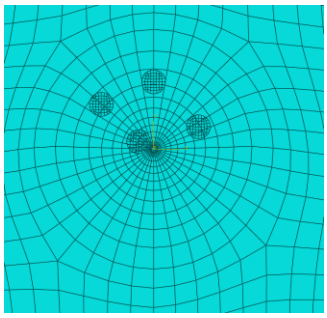

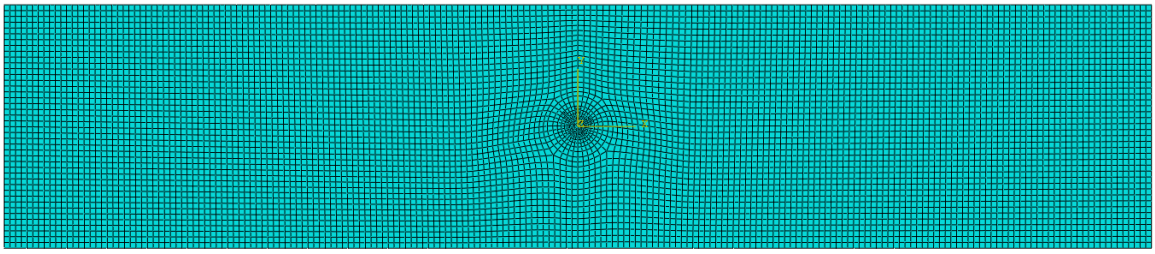

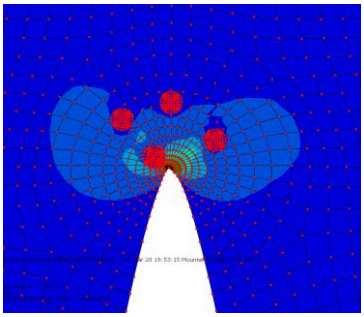

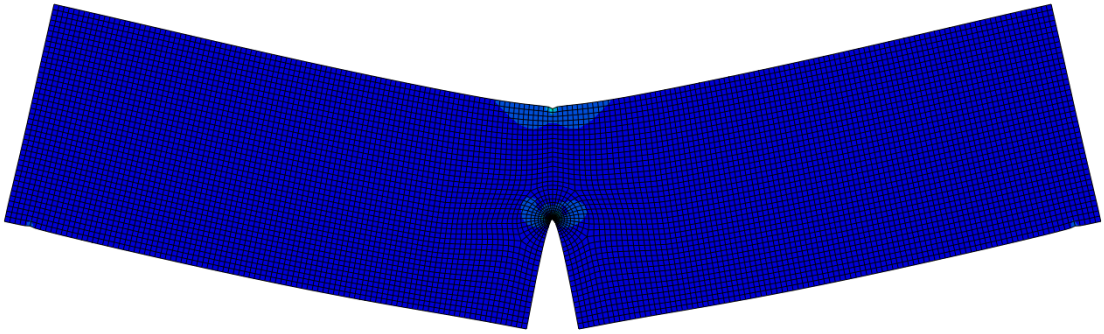

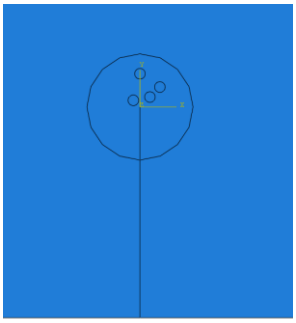

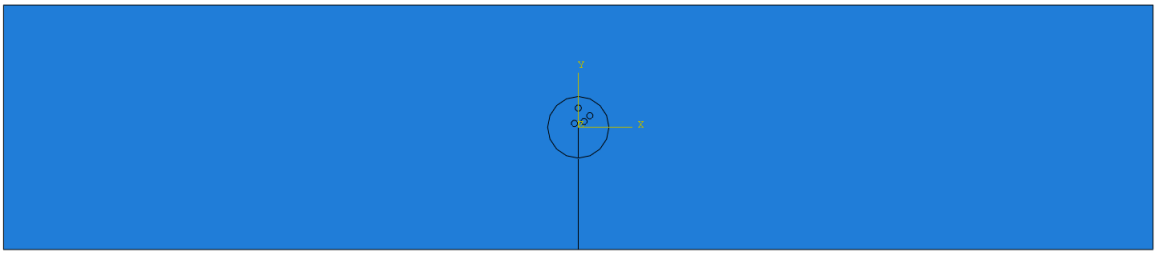

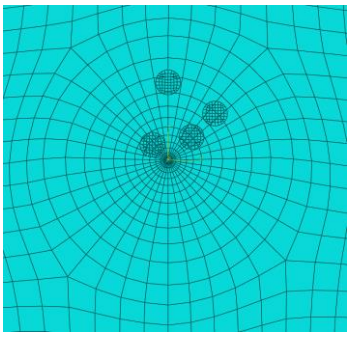

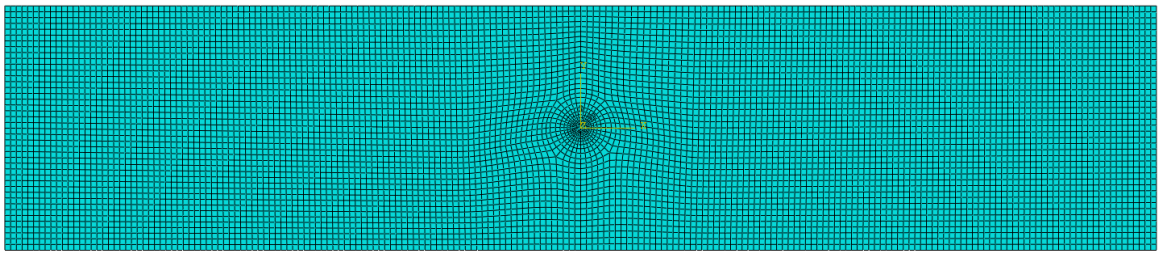

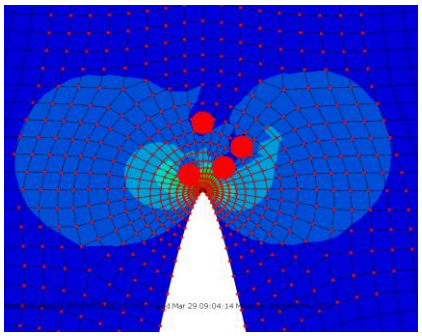

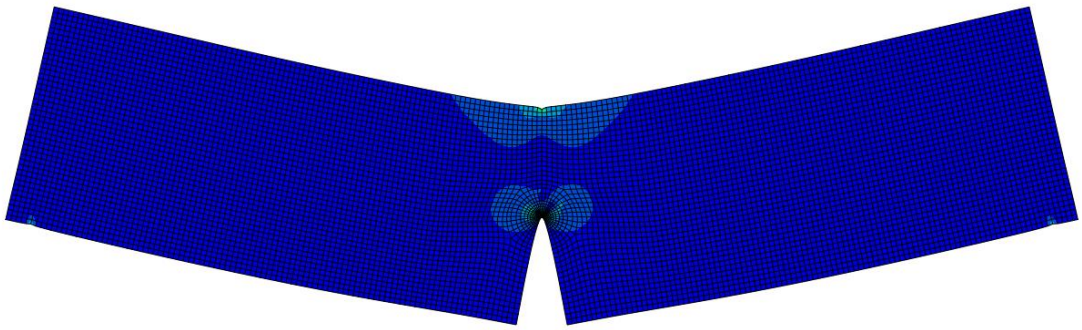

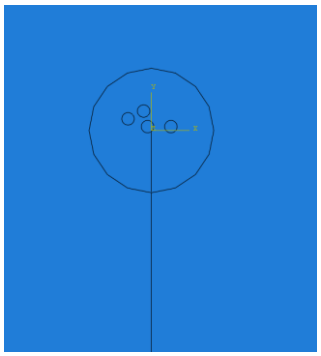

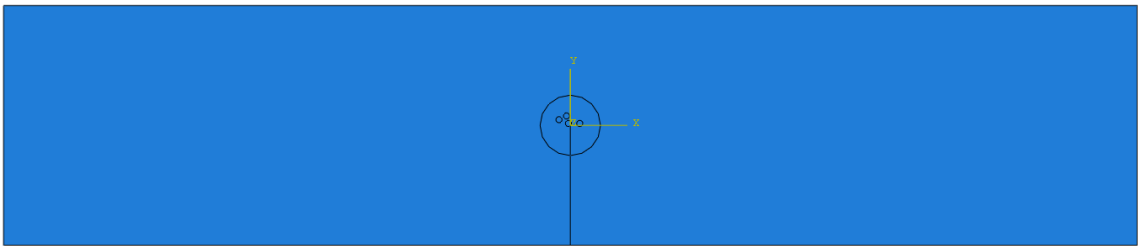

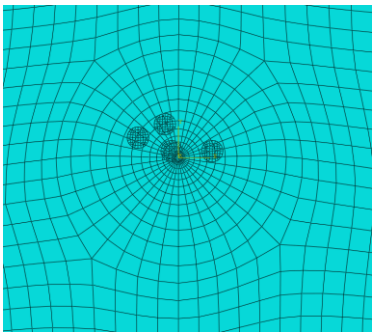

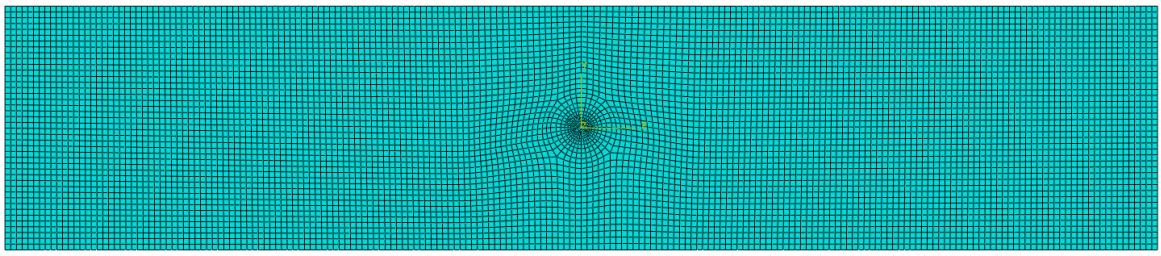

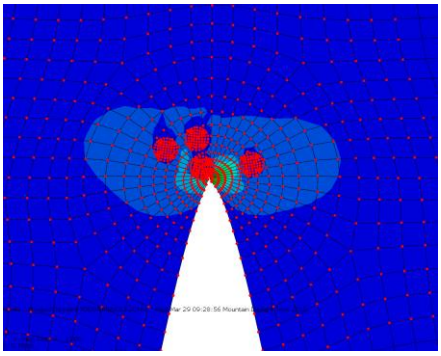

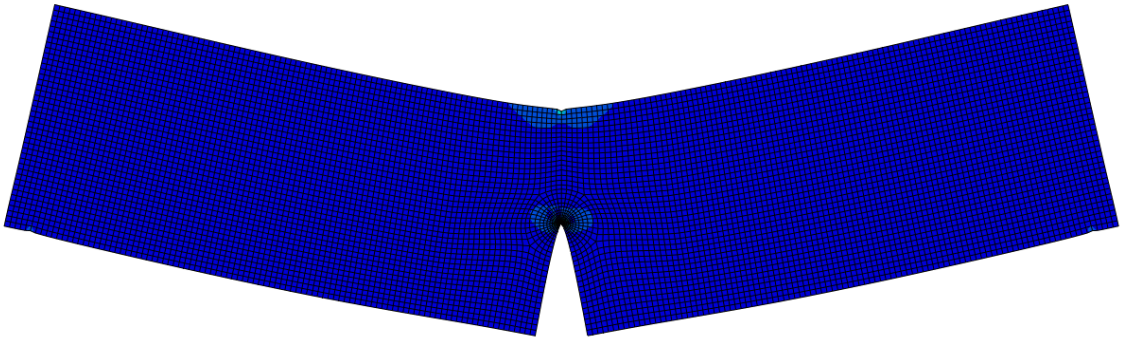

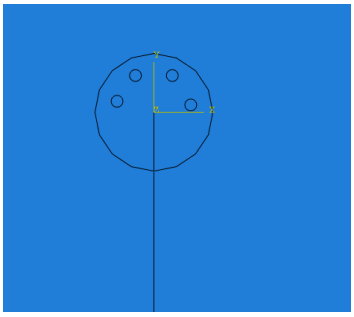

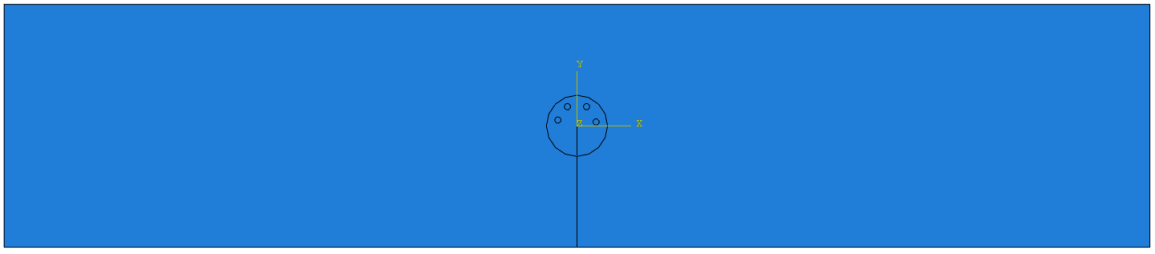

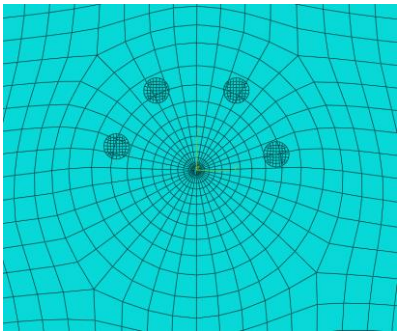

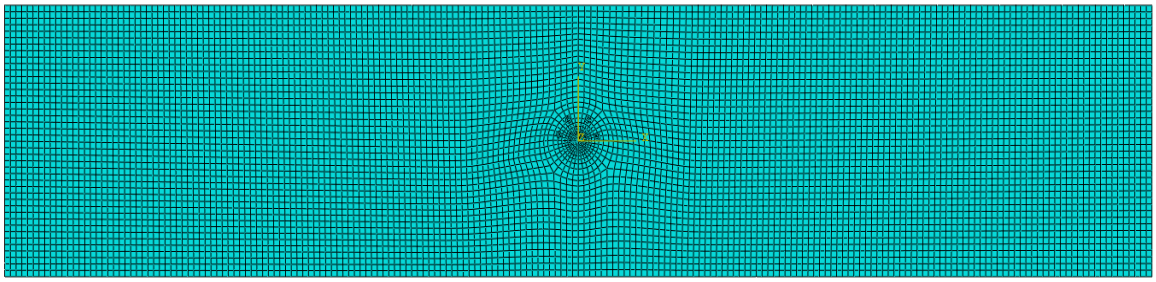

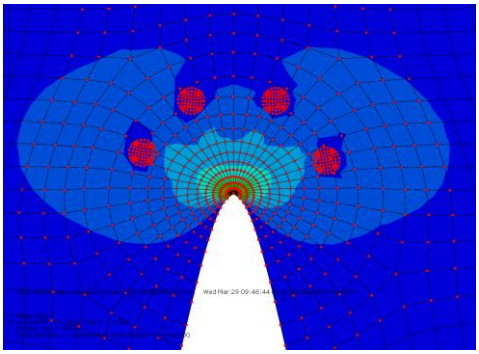

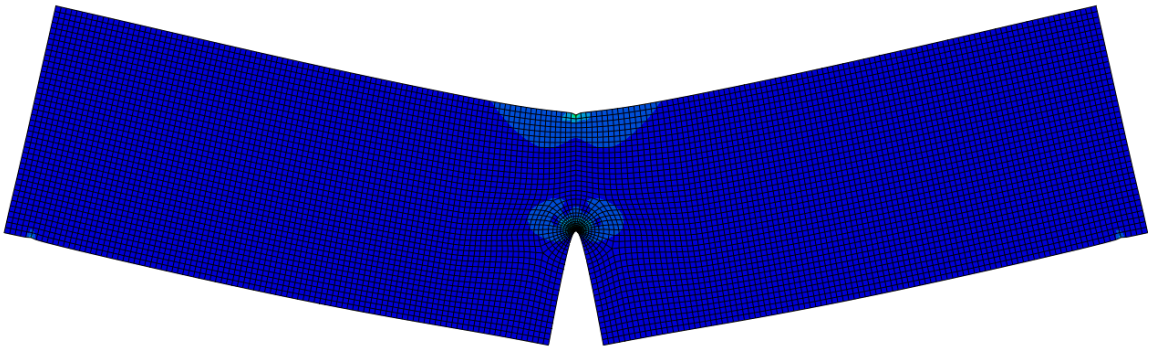

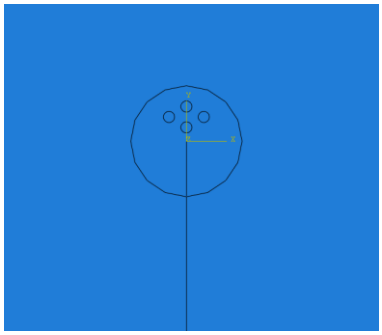

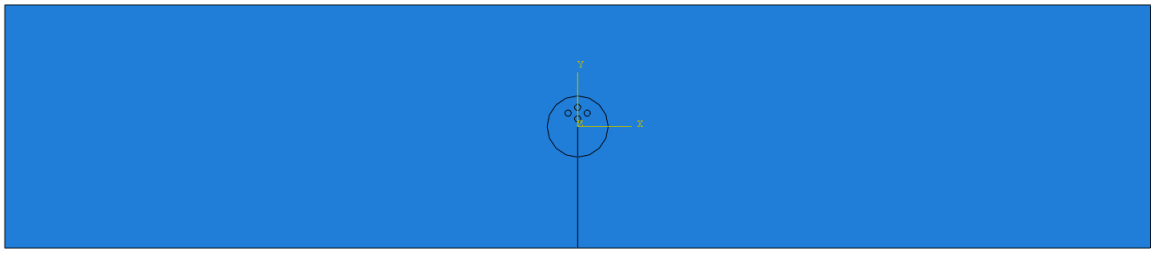

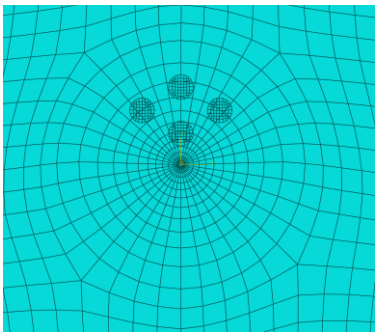

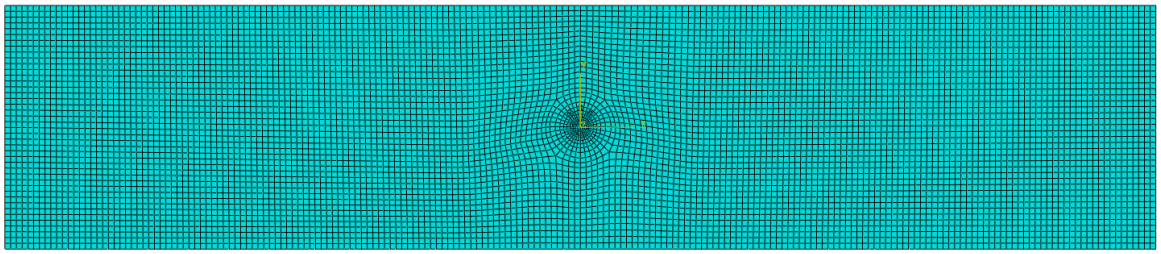

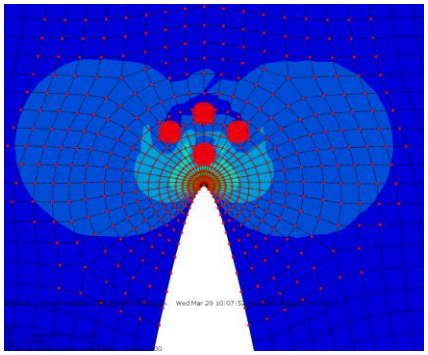

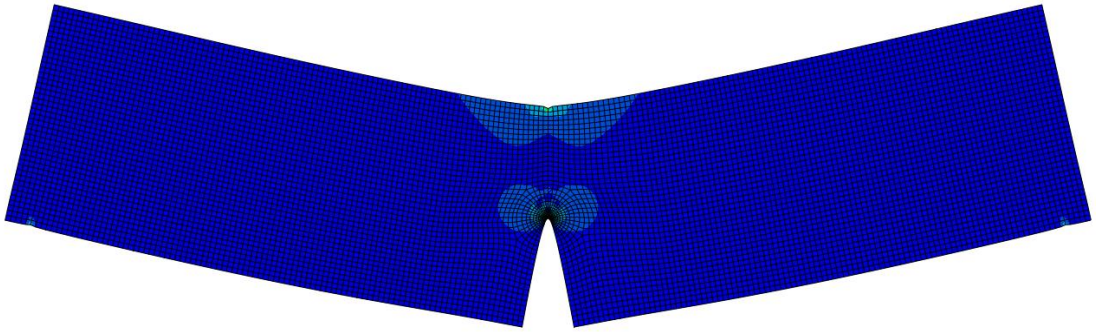

D.2.3 Jammed arrangements

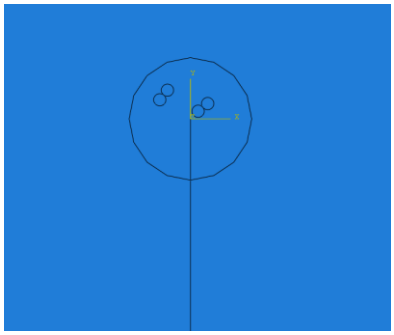

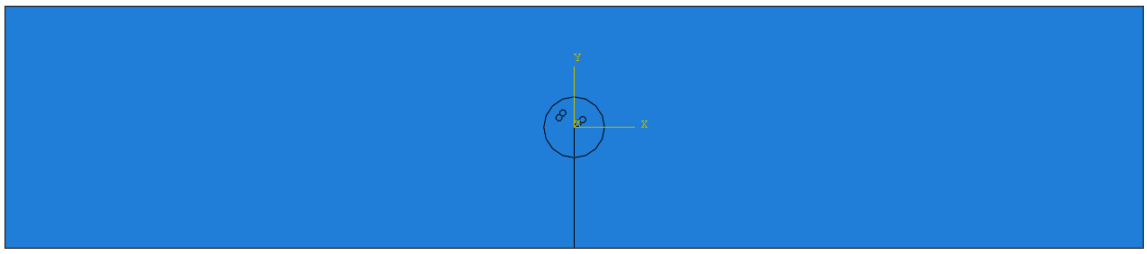

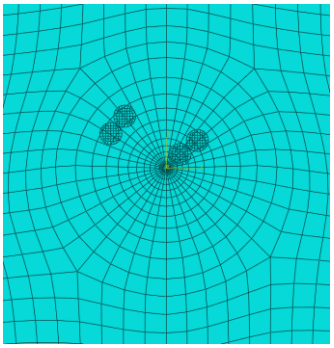

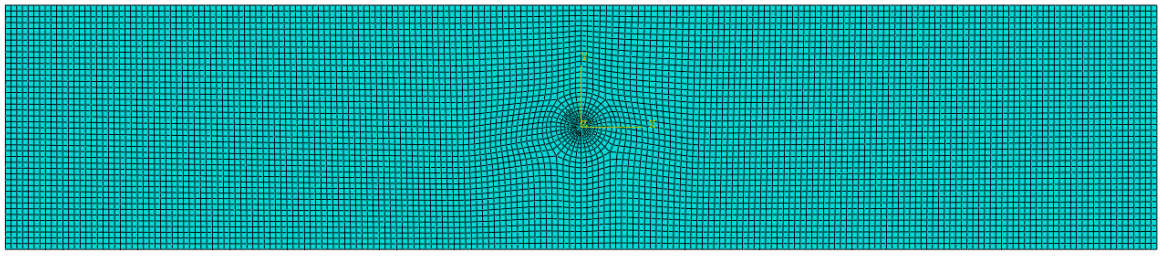

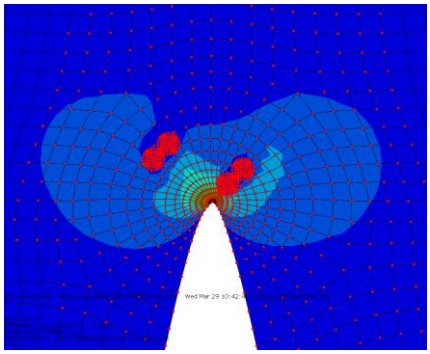

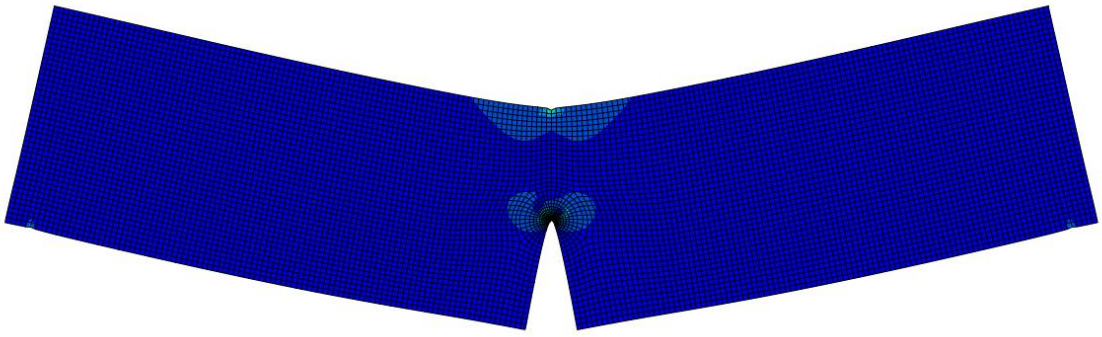

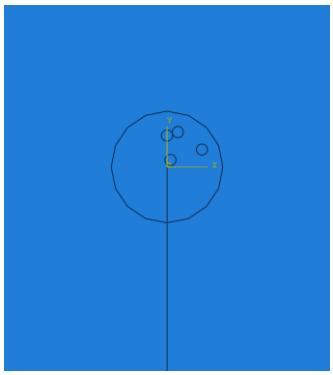

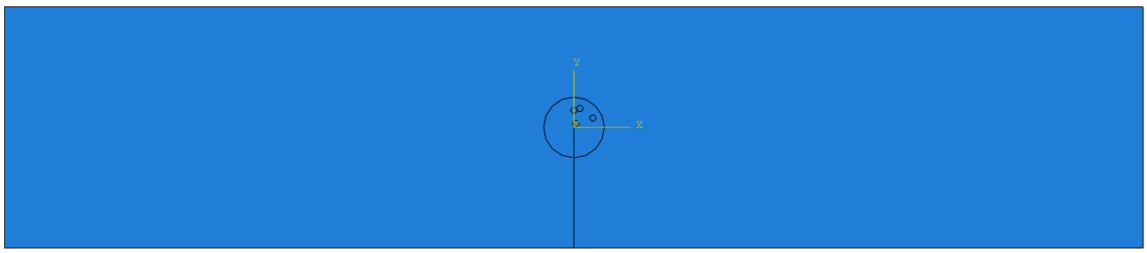

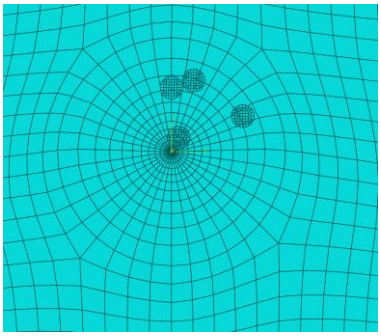

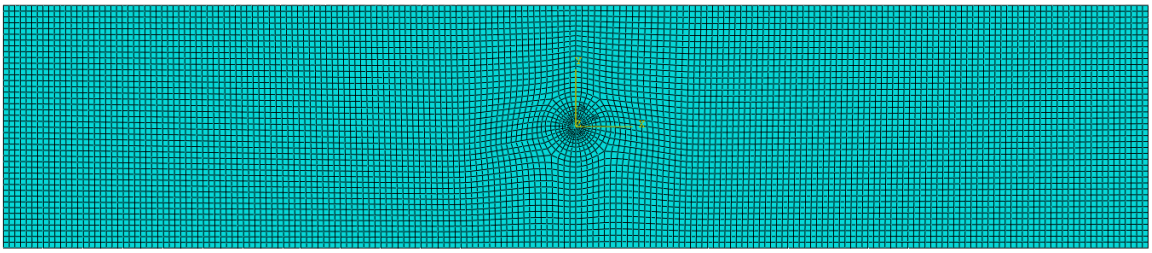

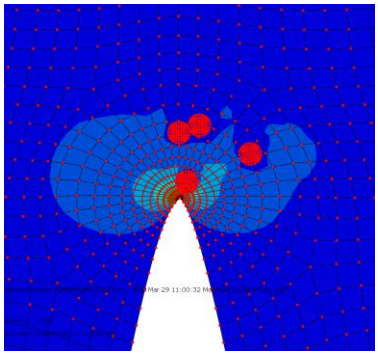

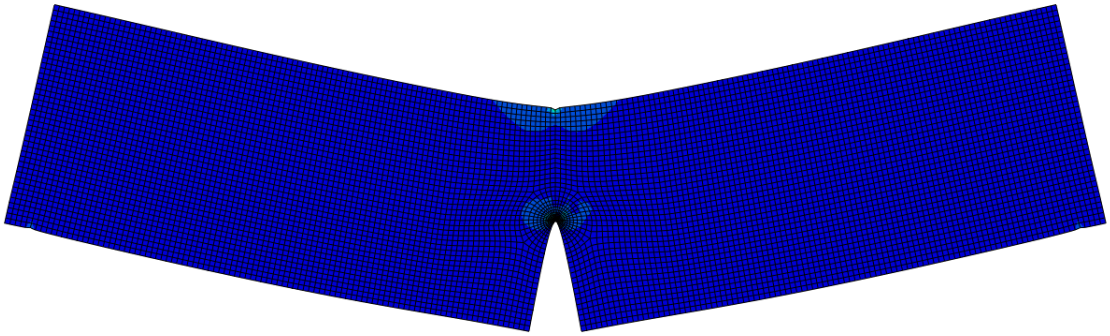

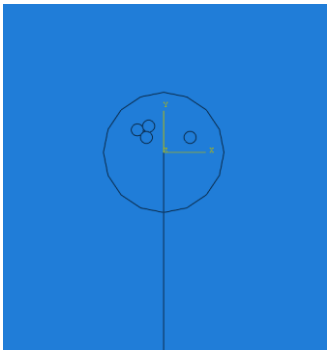

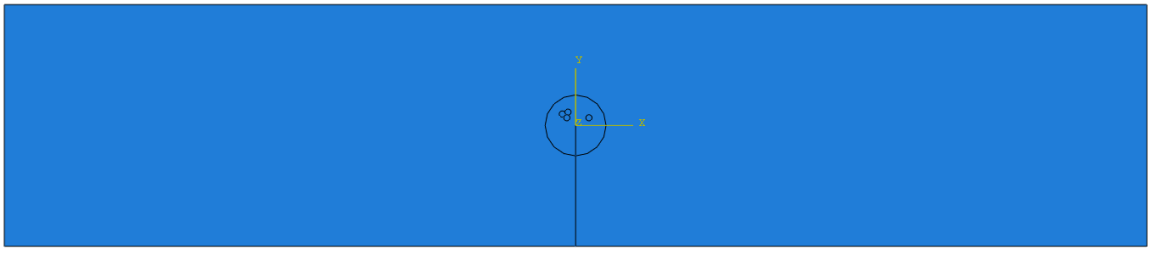

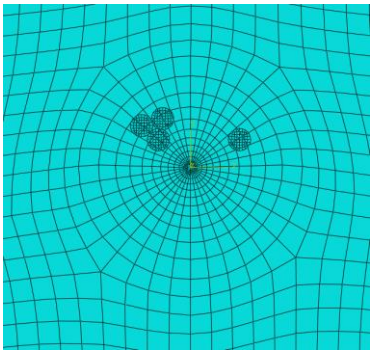

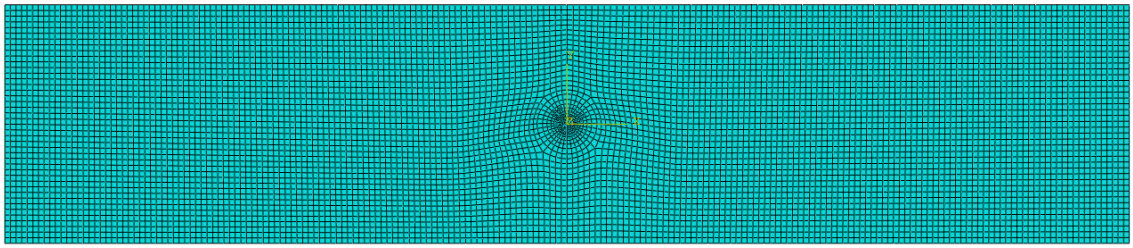

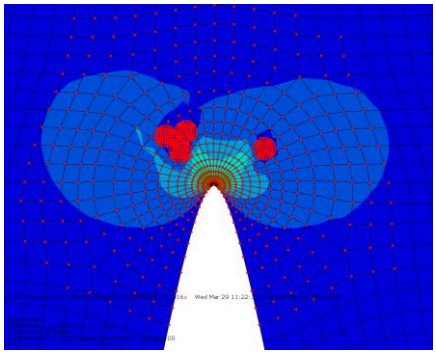

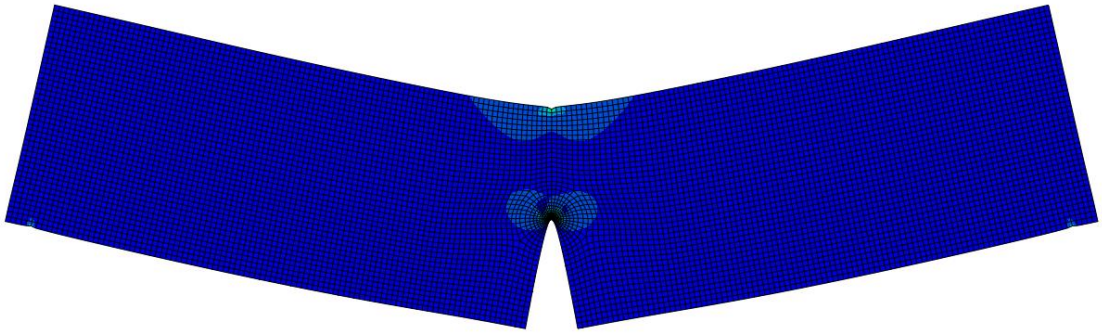

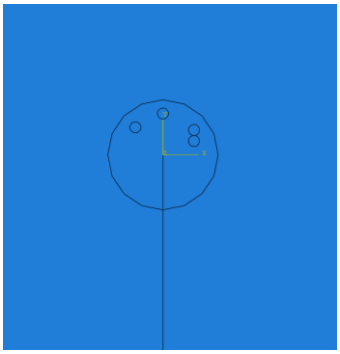

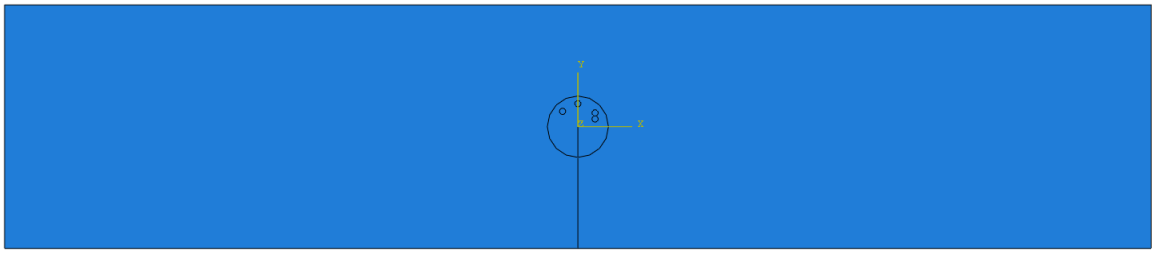

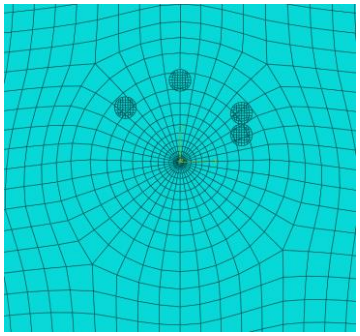

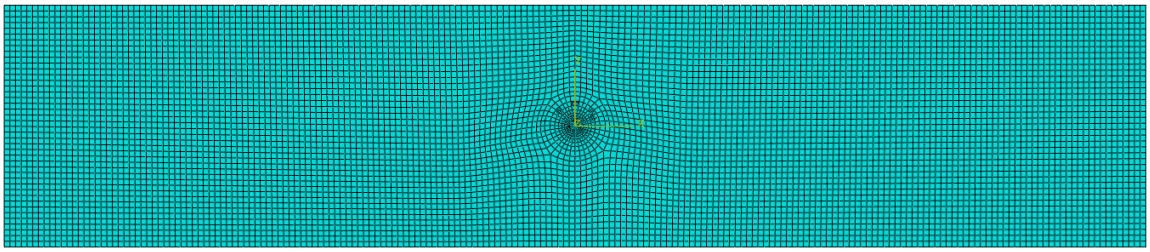

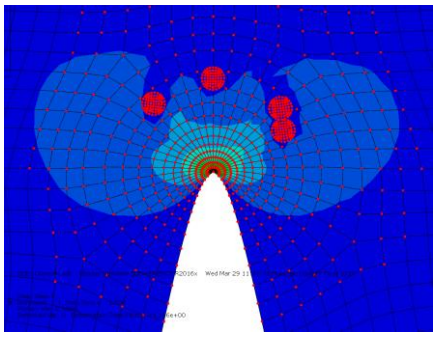

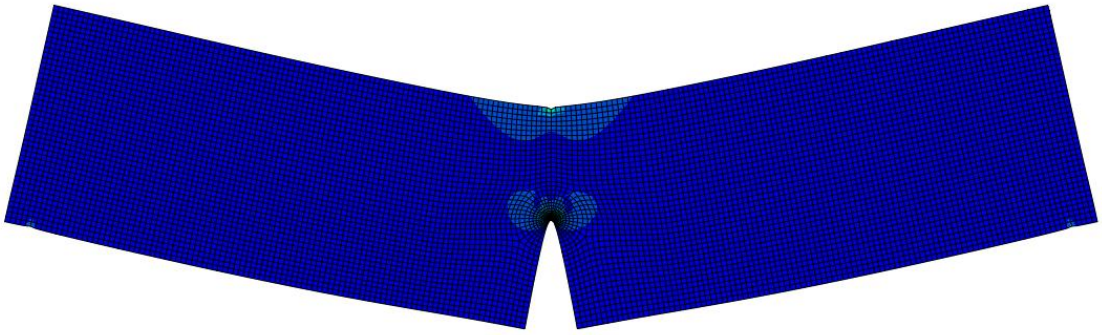

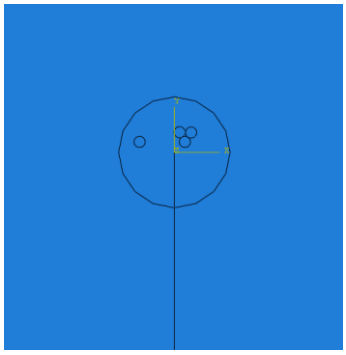

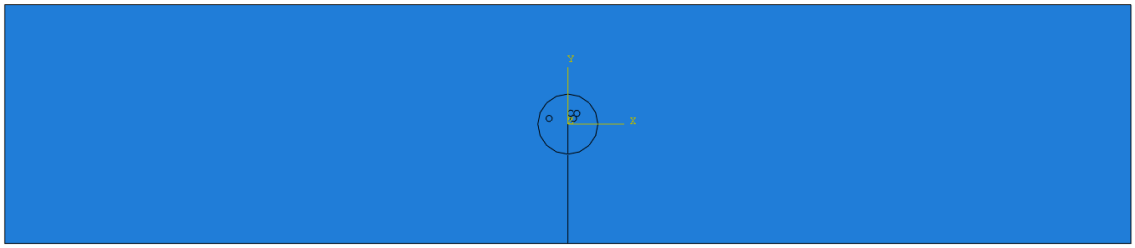
Y
X